

## **Abstract**

Huafeng Ding SCATTERING OF LIGHT WAVES BY BIOLOGICAL CELLS AND IN TISSUES. (Under the direction of Dr. Xin-Hua Hu) Department of Physics, November 2006.

Studies of optical properties of biological cells and tissues have attracted intensive research efforts due to its fundamental importance in a wide range of biomedical optics problems. The aims of this dissertation research are to construct various experimental systems to determine the distribution of refractive index on the cellular scale and the refractive index for turbid and skin samples as well as the theoretical modeling.

A goniometer system with a photoelastic modulation scheme was employed to determine Mueller matrix elements of B-cell and HL-60 cell suspension samples. The angular dependence of the sixteen elements has been determined from the scattered light signals at three wavelengths of 442, 633 and 850 (or 862) nm. A finite-difference-time-domain method and coated sphere model have been used to investigate the effect of intracellular refractive index on the angle-resolved Mueller elements at different wavelengths using the 3D structures of selected B-cells reconstructed from confocal images. With these results, we demonstrated the usefulness of light scattering method in obtaining the cell morphology information.

An automated reflectometry system was constructed and calibrated for accurate measurement of coherent reflectance curves of turbid samples and the presence of coherent and diffuse reflection near the specular reflection angle has been analyzed. The complex refractive indices of turbid samples have been determined based on the

nonlinear regression of the coherent reflectance curves by the Fresnel's equations. The complex refractive indices of fresh porcine skin epidermis and dermis tissues, human skin epidermis and dermis tissues and other turbid samples were determined at 8 wavelengths between 325 and 1550nm. Dispersion relations of the real refractive index have been obtained and compared in the same spectral region.



SCATTERING OF LIGHT WAVES BY BIOLOGICAL CELLS AND IN TISSUES

A Dissertation

Presented to

the Faculty of the Department of Physics

East Carolina University

In Partial Fulfillment

of the Requirements for the Degree

Doctor of Philosophy in Biomedical Physics

by

Huafeng Ding

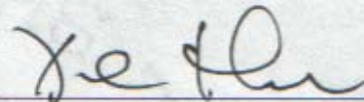
November 2006

SCATTERING OF LIGHT WAVES BY BIOLOGICAL CELLS AND  
IN TISSUES

by

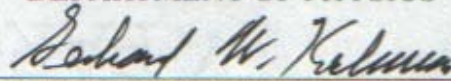
Huafeng Ding

APPROVED BY:  
ADVISOR OF DISSERTATION



XIN-HUA HU, Ph. D.  
DEPARTMENT OF PHYSICS

COMMITTEE MEMBER



GERHARD W. KALMUS, Ph. D.  
DEPARTMENT OF BIOLOGY

COMMITTEE MEMBER



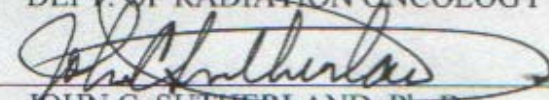
JUN QING LU, Ph. D.  
DEPARTMENT OF PHYSICS

COMMITTEE MEMBER



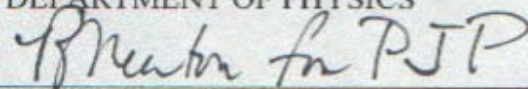
CLAUDIO H. SIBATA, Ph. D.  
DEPT. OF RADIATION ONCOLOGY

COMMITTEE MEMBER



JOHN C. SUTHERLAND, Ph. D.  
DEPARTMENT OF PHYSICS

DEAN OF THE GRADUATE SCHOOL



PATRICK J. PELLICANE, Ph. D.

## **Acknowledgements**

I would like to express my most sincere appreciations to my advisor, Dr. Xin-Hua Hu for his direction on my Ph.D. dissertation research. Dr. Hu is the person I can always ask for help since the first day I arrived here and his thorough knowledge and original insight made my projects possible. Especially, I am greatly indebted to him for his time and patience in reviewing and correcting this manuscript.

My thanks also go to Dr. Jun Qing Lu for allowing me to use her FDTD results and the Monte Carlo codes. Her professional advice on my code development is greatly appreciated.

I would like to express my appreciations to Dr. Gerhard Kalmus, Dr. Claudio Sibata and Dr. John Sutherland for serving on my dissertation committee and reviewing this manuscript.

Thanks and appreciations are also due to Dr. You Su Sun, Dr. William Wooden, Dr. Douglas Weidner and Dr. Thomas McConnell for providing us skin and cell samples.

My thanks also go to Mr. Ken Jacobs for his helps in designing and the mechanical systems.

I would like to thank the Department of Physics for their supports to my study and research here. And my thanks also go to the faculty, staff and graduate student in the department of physics for their friendship.

Finally, I would like to thank my parents and my wife for their trust, support, and encouragement throughout these years.

To My Family

## Table of Contents

List of Tables.....	viii
List of Figures.....	ix
List of Symbols.....	xv
Chapter 1 Introduction.....	1
Chapter 2 Theoretical Frameworks.....	6
2.1 Introduction.....	6
2.2 Stokes Vectors and Mueller Matrix.....	9
2.2.1 General Framework.....	9
2.2.2 Conversion from J-matrix to Mueller matrix.....	12
2.3 The Mie Theory.....	15
2.4 The Rayleigh Scattering Model.....	18
2.5 The Rayleigh-Gans Scattering Model.....	20
2.6 The Finite-Difference Time-Domain (FDTD) Method.....	23
2.7 The Effective Medium Theory.....	25
2.8 Refractive Index Determination.....	28
Chapter 3 Experimental Methods.....	31
3.1 PEM Based Goniometer System .....	31
3.1.1 The Measurement of Mueller Matrix Elements.....	31
3.1.2 Signal Processing.....	36
3.1.3 Experimental Determinations of 16 Matrix Elements.....	38

3.2 Design and control of Goniometer System.....	41
3.2.1 The Sample Holder.....	42
3.2.2 Scattering Volume.....	43
3.2.3 The Scattering Angle Range.....	45
3.2.4 Goniometer System Control and Alignment.....	47
3.3 Reflectometry System.....	48
3.3.1 Experimental System.....	49
3.3.2 The Prism Motion Control.....	50
3.4 Sample Acquisition and Preparation.....	51
3.4.1 Polystyrene Microsphere Suspensions Preparation.....	52
3.4.2 Cell Sample Preparation.....	52
3.4.3 Skin Sample Preparation.....	53
3.5 Figures.....	56
Chapter 4 Cell Scattering Measurement Results.....	58
4.1 Goniometer System Calibration .....	58
4.2 Matrix Elements of B-cells .....	61
4.3 Matrix Elements of HL-60 Cells.....	63
4.4 Figures.....	64
Chapter 5 Study of Turbid and Skin Samples.....	85
5.1 System Calibration with Water .....	85
5.2 The Complex Refractive Index of Liquid Solution .....	87
5.3 Refractive Index Determination for Skin Tissues .....	90

5.3.1 Results for Porcine Skin Tissues.....	90
5.3.2 Human Skin Results.....	92
5.4 Figures and Tables.....	95
Chapter 6 Discussions and Summary.....	114
6.1 Light Scattering by Cells .....	114
6.2 Light Scattering in Turbid and Skin Samples .....	117
6.3 Summary.....	120
6.4 Figures.....	121
Bibliography.....	123
Appendix.....	128
A. Derivations of the Mueller Matrix for Different Optical Devices.....	128
B. Mie Theory For Nonabsorptive Host Medium.....	133
C. Data Acquisition and Programs.....	142
D. VB code for goniometer system control and data collection.....	144

## **List of Tables**

Figure 3-1	Signal attenuation and phase shift in the signal conditioner.....	37
Figure 3-2	Eight combinations of the optical elements with different orientation angles.....	38
Figure 5-1	The human skin sample data .....	95
Figure 5-2	The coefficients of different dispersion equations.....	95

## List of Figures

Figure 2-1	One set of vectors for the derivation of U .....	10
Figure 2-2	Spherical polar coordinate system.....	16
Figure 2-3	Light scattering by an arbitrary particle.....	20
Figure 3-1	Schematic of the experimental setup: P: polarizer, BE: Beam expander, PE: PE modulator; B: beam expander, L: focusing lens, SH: sample holder, IT: immersion tank, Q: quarter-wave plate, A: analyzer, T: apertured tube, PM: photomultiplier, A/D: analog-to-digital converter, PC: Personal Computer. ....	32
Figure 3-2	One polarizer and modulator.....	33
Figure 3-3	Two polarizers and one modulator.....	35
Figure 3-4	Schematic diagram of the signal conditioner .....	36
Figure 3-5	Design for the sample holder .....	42
Figure 3-6	Determination of the correction factor for the scattering volume .....	43
Figure 3-7	Correction factor as a function of scattering angle by which the measure signal has to be multiplied to correct for the change scattering volume as seen by the PMT.....	45
Figure 3-8	The Scattering angle range .....	46
Figure 3-9	Goniometer system alignment. PH: Pin Hole .....	47
Figure 3-10	The schematic of the reflectometry system.....	48
Figure 3-11	Experimental Setup for refractive index measurement .....	49
Figure 3-12	Varied positions of the prism .....	51
Figure 3-13	Schematic diagram for the Si photodiode .....	56
Figure 3-14	Schematic diagram for the GaAs photodiode .....	57
Figure 4-1	The calculated sample volume “seen” by the detector versus the scattering	

	angle $\theta_s$ .....	64
Figure 4-2	Comparison between the signal (triangle) and the background noise (circle) for sphere suspension at 633nm.....	65
Figure 4-3	The measured and calculated Mueller matrix elements $S_{11}$ , $s_{12}=S_{12}/S_{11}$ and $s_{34}=S_{34}/S_{11}$ versus the scattering angle $\theta_s$ for water suspension of polystyrene microsphere with diameter of $1.00\mu\text{m}$ at 633nm. The solid lines were obtained from the Mie theory with $n_h=1.332$ and $n_{sp}=1.582$ for a single sphere and the measured $S_{11}$ was fitted to the calculated results with one adjustable constant. The normalized elements are plotted with no fitting.....	66
Figure 4-4	The measured and calculated Mueller matrix elements $S_{11}$ , $s_{12}=S_{12}/S_{11}$ and $s_{34}=S_{34}/S_{11}$ versus the scattering angle $\theta_s$ for water suspension of polystyrene microsphere with diameter of $1.00\mu\text{m}$ at 442nm. The solid lines were obtained from the Mie theory with $n_h=1.3380$ and $n_{sp}=1.601$ ...	67
Figure 4-5	The measured and calculated Mueller matrix elements $S_{11}$ , $s_{12}=S_{12}/S_{11}$ and $s_{34}=S_{34}/S_{11}$ versus the scattering angle $\theta_s$ for water suspension of polystyrene microsphere with diameter of $1.00\mu\text{m}$ at 850nm. The solid lines were obtained from the Mie theory with $n_h=1.3290$ and $n_{sp}=1.575$ .....	68
Figure 4-6	The angle-resolved Mueller matrix elements $S_{11}$ and $-s_{12}(\theta_s)$ of B-cell suspension samples at the wavelengths of 442, 633 and 862nm. The data points and error bars represent the mean and standard deviation of four measurements with different cell samples at different days.....	69
Figure 4-7	Same as Fig. 4-6 for the angle-resolved Mueller matrix elements $s_{13}(\theta_s)$ and $s_{14}(\theta_s)$ of B-cell suspension samples at the wavelengths of 442, 633 and 862nm. ....	70
Figure 4-8	Same as Fig. 4-6 for the angle-resolved Mueller matrix elements $s_{21}(\theta_s)$ and $-s_{22}(\theta_s)$ of B-cell suspension samples at the wavelengths of 442, 633 and 862nm. ....	71
Figure 4-9	Same as Fig. 4-6 for the angle-resolved Mueller matrix elements $s_{23}(\theta_s)$ and $-s_{24}(\theta_s)$ of B-cell suspension samples at the wavelengths of 442, 633 and 862nm. ....	72
Figure 4-10	Same as Fig. 4-6 for the angle-resolved Mueller matrix elements $s_{31}(\theta_s)$ and $-s_{32}(\theta_s)$ of B-cell suspension samples at the wavelengths of 442, 633 and	

	862nm. ....	73
Figure 4-11	Same as Fig. 4-6 for the angle-resolved Mueller matrix elements $s_{33}(\theta_s)$ and $-s_{34}(\theta_s)$ of B-cell suspension samples at the wavelengths of 442, 633 and 862nm. ....	74
Figure 4-12	Same as Fig. 4-6 for the angle-resolved Mueller matrix elements $s_{41}(\theta_s)$ and $-s_{42}(\theta_s)$ of B-cell suspension samples at the wavelengths of 442, 633 and 862nm. ....	75
Figure 4-13	Same as Fig. 4-6 for the angle-resolved Mueller matrix elements $s_{43}(\theta_s)$ and $s_{44}(\theta_s)$ of B-cell suspension samples at the wavelengths of 442, 633 and 862nm ....	76
Figure 4-14	The angle-resolved Mueller matrix elements $S_{11}$ and $-s_{12}(\theta_s)$ of HL-60 cell suspension samples at the wavelengths of 442, 633 and 850nm. The data points and error bars represent the mean and standard deviation of three measurements with different cell samples at different days.,.....	77
Figure 4-15	Same as Fig. 4-14 for the angle-resolved Mueller matrix elements $s_{13}(\theta_s)$ and $s_{14}(\theta_s)$ of HL-60 cell suspension samples at the wavelengths of 442, 633 and 850nm. ....	78
Figure 4-16	Same as Fig. 4-14 for the angle-resolved Mueller matrix elements $s_{21}(\theta_s)$ and $s_{22}(\theta_s)$ of HL-60 cell suspension samples at the wavelengths of 442, 633 and 850nm ....	79
Figure 4-17	Same as Fig. 4-14 for the angle-resolved Mueller matrix elements $-s_{23}(\theta_s)$ and $s_{24}(\theta_s)$ of HL-60 cell suspension samples at the wavelengths of 442, 633 and 850nm ....	80
Figure 4-18	Same as Fig. 4-14 for the angle-resolved Mueller matrix elements $s_{31}(\theta_s)$ and $s_{32}(\theta_s)$ of HL-60 cell suspension samples at the wavelengths of 442, 633 and 850nm ....	81
Figure 4-19	Same as Fig. 4-14 for the angle-resolved Mueller matrix elements $s_{33}(\theta_s)$ and $-s_{34}(\theta_s)$ of HL-60 cell suspension samples at the wavelengths of 442, 633 and 850nm ....	82
Figure 4-20	Same as Fig. 4-14 for the angle-resolved Mueller matrix elements $s_{41}(\theta_s)$ and $s_{42}(\theta_s)$ of HL-60 cell suspension samples at the wavelengths of 442, 633 and 850nm ....	83

Figure 4-21	Same as Fig. 4-14 for the angle-resolved Mueller matrix elements $s_{43}(\theta_s)$ and $s_{44}(\theta_s)$ of HL-60 cell suspension samples at the wavelengths of 442, 633 and 50nm.....84
Figure 5-1	The measured and calculated coherent reflectance versus incident angle of deionized water with s- and p-polarized incident beam at $\lambda = 633\text{nm}$ . Insert: full angular range. ....96
Figure 5-2	The reflection signal versus rotation angle of the detector at the incident angle of (a) $\theta=45^\circ$ ; (b) $\theta=70^\circ$ with a s-polarized beam at $\lambda=633\text{nm}$ for deionized water, 20% intralipid solution, porcine skin epidermis and dermis with an angular stepsize of $0.125^\circ$ . The error bars of about $\pm 5\%$ were removed for clear view and the two dashed lines indicate the angular acceptance range of the aperture in front of the photodiode.....97
Figure 5-3	Measured (symbols) and calculated (lines) coherent reflectance versus incident angle for 10% sphere suspension at 633nm for both s and p polarization. ....98
Figure 5-4	Wavelength dependence of the refractive index for 10% sphere suspension. Each data point and associated error bar are the mean and standard deviation obtained from 3 measurements. The lines are for guide of the eyes.....99
Figure 5-5	Refractive index measurement of 20% intralipid at 633nm for both s and p polarization.....100
Figure 5-6	The refractive indices of intralipid samples versus concentration. (a) real part; (b) imaginary part .....101
Figure 5-7	The (a) real and (b) imaginary refractive indices of 20% intralipid versus wavelength. Each data point and associated error bar are the mean and standard deviation obtained from 3 measurements. The lines are for guide of the eyes.....102
Figure 5-8	Effect of laser beam diameter on angle determination accuracy.....103
Figure 5-9	The microscope images of the histology slides of the skin samples from two patients: (a). ID no. 9 (skin type: III); (b). ID no. 11 (skin type: V). Bar = $100\mu\text{m}$ .....104
Figure 5-10	Schematic of skin tissue mounted for measurement. PH: Pin hole.....105

- Figure 5-11 The real (circle) and imaginary (triangle) refractive index of porcine skin dermis versus pressure. Each data point and associated error bar are the mean and standard deviation obtained from 3 measurements. The lines are for guide of the eyes.....106
- Figure 5-12 The coherent reflectance for porcine skin versus the incident angle at  $\lambda=1064\text{nm}$ : (a) dermis; (b) epidermis.....107
- Figure 5-13 The (a) real and (b) imaginary refractive indices of porcine skin epidermis versus wavelength. Each data point and associated error bar are the mean and standard deviation obtained from 9 measurements. The lines are for guide of the eyes.....108
- Figure 5-14 The (a) real and (b) imaginary refractive index of porcine skin dermis versus wavelength. Each data point and associated error bar are the mean and standard deviation obtained from 9 measurements. The lines are for guide of the eyes.....109
- Figure 5-15 The typical measured coherent reflectance curves of two skin samples from two patients at  $\lambda=442\text{nm}$  with a s-polarized incident beam: (a) epidermis; (b) dermis. The solid lines are calculated curves based on the Fresnel's equations with the following values of the complex refractive index: (a)  $n = 1.445 + i1.00 \times 10^{-2}$  for ID #3 (skin type: V) and  $n = 1.458 + i8.34 \times 10^{-3}$  for ID #9 (skin type: III); (b)  $n = 1.394 + i9.30 \times 10^{-3}$  for ID #3 and  $n = 1.404 + i9.20 \times 10^{-3}$  for ID #9.....110
- Figure 5-16 The dependence of the coefficient of determination  $R^2$  on different choices of  $n_r$  or  $n_i$  for a coherent reflectance curve measured from the epidermis or dermis side of a skin sample at  $\lambda=442\text{nm}$ . .....111
- Figure 5-17 The (a) real and (b) imaginary refractive indices of human skin epidermis versus wavelength. Each data point and associated error bar are the mean and standard deviation obtained from 6 or 9 measurements of 2 or 3 skin samples. The lines in (a) are based on the dispersion equations.....112
- Figure 5-18 The (a) real and (b) imaginary refractive indices of human skin dermis versus wavelength. Each data point and associated error bar are the mean and standard deviation obtained from 6 or 9 measurements of 2 or 3 skin samples. The lines in (a) are based on the dispersion equations.....113
- Figure 6-1 The angle-resolved Mueller matrix elements of  $S_{11}$ ,  $-s_{12}$  and  $-s_{34}$  calculated by the FDTD method for B-cell of 3D structures reconstructed from its confocal images with refractive indices set at  $n_h=1.336$  for the host medium,  $n_c=1.380$  for the cytoplasm and  $n_n=1.430$  for the nucleus at

$\lambda=633\text{nm}$  and  $n_h=1.330$ ,  $n_c=1.368$  and  $n_n=1.400$  or  $1.433$  at  $\lambda=850\text{nm}$ . The calculated elements are the averaged values over 12 orientations .....121

Figure 6-2	The angle-resolved Mueller matrix elements of $S_{11}$ , $-s_{12}$ and $-s_{34}$ calculated by a coated sphere model with the mean inner radius $r_n=4.143\mu\text{m}$ and outer radius $r_c=5.133\mu\text{m}$ . The mean values of the refractive indices were assigned as: $n_h=1.342$ , $n_c=1.400$ and $n_n=1.460$ at $\lambda=442\text{nm}$ ; $n_h=1.336$ , $n_c=1.380$ and $n_n=1.430$ at $\lambda=633\text{nm}$ ; $n_h=1.330$ , $n_c=1.368$ and $n_n=1.400$ at $\lambda=850\text{nm}$ . The elements are the values averaged over the coated spheres of Gaussian distributions with $\pm 20\%$ on $r_n$ and $r_c$ and $\pm 3.6\%$ on $n_n$ and $\pm 0.8\%$ on $n_c$ .....122
Figure A-1	Specification of the field components( $\hat{e}_i$ specifies the axes of the modulator) .....128
Figure A-2	Light through modulator.....130
Figure B-1	Spherical polar coordinate system.....134
Figure D-1	Goniometer system control.....144

## List of Symbols

Symbol	Name	Unit
$a_n$	Scattering coefficient	
$b_n$	Scattering coefficient	
$c_i$	Normalization constants for matrix elements	
$\vec{E}$	Electric field of a plane wave	N/C
$\vec{E}_i$	Incident electric field	N/C
$\vec{E}_s$	Scattered electric field	N/C
$E_{\parallel}$	Parallel component of the electric field	N/C
$E_{\perp}$	Perpendicular component of the electric field	N/C
$\epsilon$	permittivity	F/m
$\epsilon_{\text{eff}}$	Effective dielectric constant	F/m
$\psi$	Scalar function	
$g$	Anisotropy factor	
$\vec{H}$	Magnetic field of a plane wave	
$I_i$	Radiance or intensity of incident wave	W/m <sup>2</sup>
$I_s$	Irradiance of the scattered field	W/m <sup>2</sup>
$I_{si}$	Scattering signal from ith combination	v
(I,Q,U,V)	Stokes vectors	

$J$	Amplitude matrix	
$k$	Wave number	$m^{-1}$
$\lambda$	Wavelength	$m$
$m$	Relative refractive index	
$\mu$	permeability	$N/A^2$
$\mu_a$	Absorption coefficient	$mm^{-1}$
$\mu_s$	Scattering coefficient	$mm^{-1}$
$n_0$	Refractive index for prism	
$n_i$	Imaginary part of a complex refractive index	
$n_r$	Real part of a complex refractive index	
$p(\hat{s}, \hat{s}')$	Phase function	
$\pi_n$	Angular dependent function	
$\theta$	Incident angle	degree
$\theta_s$	Scattering angle	degree
$R(\theta)$	Reflectance	
$R^2$	Coefficient of determination of fitting error	
$S_{ij}$	Mueller matrix for scatterers	
$\tau_n$	Angular dependent function	
$V_{corr}$	Volume correction factor	
$\omega$	Modulation frequency	Hz

## Chapter 1 Introduction

Investigation of optical properties of biological cells and tissues has attracted intensive research efforts for its fundamental importance in a wide range of biomedical optics problems. Among various properties, the parameters of these biological systems related to elastic light scattering are of particular interests since the elastically scattered light signals are often the strongest signals yielded by a turbid system. Elastically scattered or simply the scattered light has been measured in many laboratories as the primary means to analyze biological systems ranging from tissues to cells. Light scattering is caused by inhomogeneity or fluctuation in the dielectric functions or refractive indices of a medium and therefore provides a sensitive tool to determine the structure and composition of the medium. The objective of this dissertation research is to conduct a systematic investigation of light scattering by biological cells and in tissues by combining experimental measurement of scattered light distribution with theoretical modeling. The dissertation research consists of two related topics on distributions of refractive index on the microscopic scales by biological cells and the refractive index of turbid samples and biological tissues with macroscopic dimensions. The specific aims of the dissertation research are

- (1) Construct a goniometer system to measure the angular dependence of light scattered by biological cells and determine the Mueller matrix elements of the cell samples at three different wavelengths: 442nm, 633nm and 850 (or 862) nm.

- (2) Compare the calculated angular dependence of the Mueller matrix elements with modeling tools of the finite-difference-time-domain method (performed by other researchers) to solve the Maxwell's equations to understand the correlation between the Mueller matrix elements and the intracellular distribution of refractive index.
- (3) Construct a prism-based reflectance system to measure the angular dependence of the coherent reflectance and transmission of turbid samples and skin tissues *in vitro* to determine the refractive index on the macroscopic scales between 325 and 1550nm in wavelength.
- (4) Obtain the dispersion relations of refractive index of the skin tissues using the Fresnel's equations and an effective medium theory.

For the first part of the dissertation research, we investigate the process of light scattering by biological cells with sizes close to the light wavelength on the scale of micrometers. The classical electrodynamic theory is required to accurately model this complex phenomenon (Jackson 1975). Analytical modeling of experimental data is only possible for scatterers of simple geometric shapes such as spheres and is extremely difficult, if not impossible, for biological cells because of their arbitrary shapes and complicated structures. The fundamental problem of deriving structural features of scatterer (i.e. cells) from light scattering information has not been solved because of the lack of accurate and efficient modeling tools. One approach of numerical modeling is to use the finite-difference time-domain (FDTD) method (Dunn and Richard-Kortum 1996; Dunn, Smithpeter et al. 1997), which was originally proposed as the method of solution

to the boundary problems of Maxwell's equations (Yee 1966). Recently, a parallel FDTD code with improved accuracy has been developed in our lab that has the capability to accurately model the light scattering by cells (Brock, Hu et al. 2005; Lu, Yang et al. 2005). This development has enabled us to compare the measured data to the results of FDTD simulations for investigating the cell morphology information through light scattering studies.

The second part of this dissertation research is mainly based on the angular measurement of coherent reflectance and transmission. On the scales much larger than wavelengths of visible and near-infrared light, the optical properties of turbid biological tissues are described by the optical parameters of scattering coefficient  $\mu_s$ , absorption coefficient  $\mu_a$  and scattering phase function  $p(\mathbf{s}, \mathbf{s}')$  based on the radiative transfer theory (Chandrasekhar 1960). Radiative transfer theory is preferred because it provides a practical theoretical framework in the problems of multiple light scattering dominating the light-tissue interaction over spatial scales of millimeters or larger. The radiative transfer theory, however, has to be complemented with proper boundary conditions. Consequently, as light propagates through an interface between two media of different optical properties, such as the air-tissue interface, an effective medium theory based on the wave model of light has often been invoked to define the boundary conditions. Since the tissue interfaces play an important role in determining the light distribution (Barrera and Garcia-Valenzuela 2003), we need to clearly understand the effective medium theory for turbid media. With these models one may define a refractive index for a turbid

medium and obtain detailed knowledge of refractive index to quantitatively describe the light-tissue interaction near an interface.

The organization of the dissertation is as the following. In Chapter 2, we first introduce the Stokes vectors and Mueller matrix as a platform for discussion of elastic light scattering by biological cells. The Stokes vectors are used for complete description of the polarized incident and scattered light beams, and a 4x4 Mueller matrix for characterization of scatterers. Therefore, the scattered light can be obtained through matrix multiplication. Various analytical microscopic scattering models are introduced, from the simple Rayleigh scattering model to the Mie theory, to help understand the light scattering process before the final discussion of the FDTD method. The effective medium theory is then introduced for understanding the refractive index of a turbid system. At the end of this chapter, the coherent reflection of an incident light beam according to the Fresnel's equations is discussed to define the refractive indices of the turbid samples and skin tissues and their inverse determination through nonlinear regression of the coherent reflection data is also described.

Chapter 3 presents the experimental designs for the measurement of Mueller matrix elements of cellular scatterers with a photoelastic modulator based goniometer system and the measurement of refractive indices for turbid and skin samples with a reflectometry system. The method for measuring the Mueller matrix is first introduced in this chapter, and the goniometer system design, control and alignment are then discussed. Following that, we present the prism based reflectometry system for measurement of

coherence reflectance curves. Sample preparations for polystyrene microsphere suspensions, cell solutions and skin tissues are described in detail.

The results of the experimental determinations of the 16 Mueller matrix elements for two different cell samples with our goniometer system are presented in Chapter 4. The system calibration with microsphere suspension is carried out at the three experimental wavelengths 442, 633 and 850 (or 862) nm and the comparison with Mie theory calculations for three matrix elements is provided. Following that, the experimentally determined matrix elements for human B-cells are demonstrated in a series of figures. The same procedures are followed for HL-60 cells and the results are shown at the end of this chapter.

Chapter 5 presents the results for the measurement of refractive indices for turbid samples and biological tissues. The complex refractive indices for turbid samples, both microsphere suspension and intralipid solution, are first determined with our calibrated reflectometry system at multiple wavelengths. And the refractive indices of tissue samples at eight different wavelengths are investigated. Various dispersion schemes are applied to model the real refractive index of human skin tissues at wavelengths between 300 and 1600nm.

In Chapter 6, we discuss and summarize the experimental results of this dissertation research as well as the possible research that should be pursued in the future.

## Chapter 2 Theoretical Frameworks

In this chapter, we first introduce the Stokes vectors and Mueller matrix to lay a foundation for understanding the light scattering by biological cells. Various light scattering models are discussed, ranging from the analytical Rayleigh scattering model to the numerical FDTD method. The effective medium theory is then reviewed to understand the refractive index of turbid samples that is determined with nonlinear regression of the reflection data.

### 2.1 Introduction

The strong correlation between the light scattering signals in the visible and near-infrared regions and cell morphology has been demonstrated by numerous studies (Wyatt and Phillips 1972; Brunsting and Mullaney 1974; Salzman, Crowell et al. 1975). The experimental determinations of the Mueller matrix for biological cells have been performed with a goniometer system on two strains of bacillus subtilis with the wavelength from 200 to 300nm (Bickel, Davidson et al. 1976). The measurements of the wavelength and scatterer size dependence of scattering have also been carried out (Mourant, Freyer et al. 1998). Cell suspensions were used in these measurements, which reveal the mechanisms underlying the optical properties of biological tissues in vivo. The complete description of the light scattering by biological cells can be expressed in terms of Stokes vectors for the incident and scattered light fields and a Mueller matrix for the scatterers.

We first consider a single particle as the example to understand the physics of scattering modeling. In general, the phase and amplitude of scattered waves change as the functions of the direction or the scattering angle. If the particle size is much smaller than the wavelength, we expect little change in the incident field as it propagates inside the particle. That is generally called the Rayleigh scattering model (Bohren and Huffman 1983). As particle size is increased to be close to or larger than the wavelength of the incident light, the phase change has to be considered and the scattered field becomes more oscillatory as a function of the scattering angle. For particles with sizes close to the wavelength but with small relative refractive indices, the Rayleigh-Gans model (Turner 1973) can be applied. The angular distributions of the scattered fields or related light intensities depend on the morphology and dielectric constant or refractive index distributions. If the particles are spherical, one can use the Mie model (Mie 1908) for the calculation of the scattered field.

For other complicated shapes of particles such as human cells, numerical models are required. One example is provided by the Finite-Difference Time-Domain (FDTD) method (Brock, Hu et al. 2005; Lu, Yang et al. 2005). The FDTD method has several advantages in comparison with other numerical techniques that include the ability to treat scatterers with inhomogeneous body, relatively simple algorithm and code parallelization. To account for the changes in intensity and polarization in the light scattering process, we provide a brief discussion of the Mueller matrix notations. In this dissertation, we develop a goniometer based system to measure the scattered light by cell suspension samples to determine their Mueller matrix elements and compare the measured data to

the calculated results by a FDTD method or the coated sphere model to study the correlation between the light scattering signals and the refractive index distribution of the cells.

In turbid media of macroscopic scales, such as biological tissues, light distribution is dominated by multiple light scattering since the scattering arises from the local micro-scale fluctuations of refractive index (van Gemert, Jacques et al. 1989; Wang, Zhang et al. 2002). The concept of an average or effective index may be introduced which is an important optical parameter for tissues (van Gemert, Jacques et al. 1989). Sparse studies were carried out to measure the indices of biological tissues because of the difficulty in optical measurements for turbid samples. The real part of refractive index of human tissues has been determined by using optical fiber immersion and optical coherence tomography (OCT) (Tearney, Brezinski et al. 1995; Knuttel and Boehlau-Godau 2000). The complex refractive index of cornea at 193 and 213 nm was determined by fitting the measured reflectance versus incident angle curves to the theoretical calculations based on the Fresnel's equations (Pettit and Ediger 1996). We should point out, however, that the above work assumed only the absorption of incident light in the corneal tissues as the cause of imaginary part of the refractive index. In our study, the imaginary part of the refractive index is due to mostly the loss of coherent component of the incident light waves in a turbid sample due to scattering.

Based on the effective medium theory, the coherent component of light reflected from or transmitted through a turbid sample can be measured to determine the refractive

index of the medium (Michael I. Mishchenko 2000). The Fresnel's equations are introduced to extract the complex refractive index of a turbid sample by nonlinear regression of the coherent reflection curve.

## 2.2 Stokes Vectors and Mueller Matrix

### 2.2.1 General Framework

The Stokes parameters (I, Q, U, V) provide a complete description of polarized light, which is particularly useful in scattering problems. The definitions of the Stokes parameters are given by

$$\begin{aligned}
 I &= E_{\parallel}E_{\parallel}^* + E_{\perp}E_{\perp}^* \\
 Q &= E_{\parallel}E_{\parallel}^* - E_{\perp}E_{\perp}^* \\
 U &= E_{\parallel}E_{\perp}^* + E_{\perp}E_{\parallel}^* \\
 V &= i(E_{\parallel}E_{\perp}^* - E_{\perp}E_{\parallel}^*)
 \end{aligned} \tag{2.1}$$

where an incident electric field is decomposed along two perpendicular axes and the constants relating irradiance to  $|\vec{E}|^2$  are ignored. Each vector has its own physical meaning. I is the total light irradiance; Q is the irradiance difference between linear polarization at  $0^\circ$  (parallel) and  $90^\circ$  (perpendicular) to the scattering plane; U is the irradiance difference between linear polarization at  $45^\circ$  and  $-45^\circ$ ; and V is the irradiance difference between right- and left-handed circular polarization.

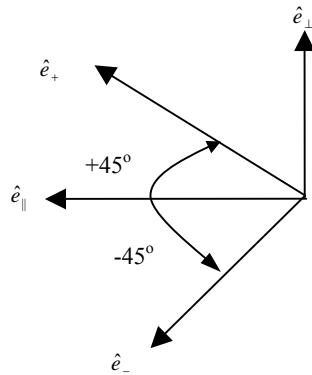


Figure 2-1 One set of vectors for the derivation of U

The derivations for I and Q are straightforward (Bohren and Huffman 1983) and will not be discussed here. To derive the element U, we need introduce another orthonormal set of vectors  $\hat{e}_+$  and  $\hat{e}_-$ , which are obtained by rotating  $\hat{e}_\parallel$  for  $+45^\circ$  and  $-45^\circ$  (Fig. 2-1),

$$\hat{e}_+ = \frac{1}{\sqrt{2}}(\hat{e}_\parallel + \hat{e}_\perp), \hat{e}_- = \frac{1}{\sqrt{2}}(\hat{e}_\parallel - \hat{e}_\perp). \quad (2.2)$$

Therefore, the electric field  $\vec{E}$  of a light beam can be written as  $\vec{E} = E_+\hat{e}_+ + E_-\hat{e}_-$ , where

$$E_+ = \frac{1}{\sqrt{2}}(E_\parallel + E_\perp), \quad E_- = \frac{1}{\sqrt{2}}(E_\parallel - E_\perp). \quad (2.3)$$

With these notations, the irradiance of a light beam transmitting through a  $+45^\circ$  polarizer is  $I_+ = (E_\parallel E_\parallel^* + E_\parallel E_\perp^* + E_\perp E_\parallel^* + E_\perp E_\perp^*)/2$  while that through a  $-45^\circ$  polarizer is  $I_- = (E_\parallel E_\parallel^* - E_\parallel E_\perp^* - E_\perp E_\parallel^* + E_\perp E_\perp^*)/2$ . The element U is then given by:

$$I_+ - I_- = E_\parallel E_\perp^* + E_\perp E_\parallel^*. \quad (2.4)$$

The element  $V$  can be derived by following the same procedures, but one more set of vectors ( $\hat{e}_R$  and  $\hat{e}_L$ ) need be introduced:

$$\hat{e}_R = \frac{1}{\sqrt{2}}(\hat{e}_{\parallel} + i\hat{e}_{\perp}), \hat{e}_L = \frac{1}{\sqrt{2}}(\hat{e}_{\parallel} - i\hat{e}_{\perp}). \quad (2.5)$$

The electric field thus can be written as  $\vec{E} = E_R\hat{e}_R + E_L\hat{e}_L$ , where

$$E_R = \frac{1}{\sqrt{2}}(E_{\parallel} - iE_{\perp}), \quad E_L = \frac{1}{\sqrt{2}}(E_{\parallel} + iE_{\perp}). \quad (2.6)$$

Similarly, the irradiance of light transmitting through a right-handed polarizer is  $I_R = (E_{\parallel}E_{\parallel}^* - iE_{\parallel}E_{\perp}^* + iE_{\perp}E_{\parallel}^* + E_{\perp}E_{\perp}^*)/2$  while that through a left-handed polarizer is  $I_L = (E_{\parallel}E_{\parallel}^* + iE_{\parallel}E_{\perp}^* - iE_{\perp}E_{\parallel}^* + E_{\perp}E_{\perp}^*)/2$ . The difference between these two irradiances provides  $V$

$$V = I_R - I_L = i(E_{\parallel}E_{\perp}^* - E_{\perp}E_{\parallel}^*). \quad (2.7)$$

The effect of an optical system on an incident electromagnetic field can be represented by a  $4 \times 4$  Mueller matrix, which relates the Stokes parameters between incident and transmitted fields:

$$\begin{pmatrix} I_t \\ Q_t \\ U_t \\ V_t \end{pmatrix} = \begin{pmatrix} S_{11} & S_{12} & S_{13} & S_{14} \\ S_{21} & S_{22} & S_{23} & S_{24} \\ S_{31} & S_{32} & S_{33} & S_{34} \\ S_{41} & S_{42} & S_{43} & S_{44} \end{pmatrix} \begin{pmatrix} I_i \\ Q_i \\ U_i \\ V_i \end{pmatrix} = \mathbf{S} \begin{pmatrix} I_i \\ Q_i \\ U_i \\ V_i \end{pmatrix}. \quad (2.8)$$

The sixteen elements of the matrix above are not always independent. For a randomly oriented collection of particles, if the particle(s) has (have) no optical activity, the Mueller matrix becomes (Hunt and Huffman 1973):

$$\begin{pmatrix} S_{11} & S_{12} & 0 & 0 \\ S_{12} & S_{22} & 0 & 0 \\ 0 & 0 & S_{33} & S_{34} \\ 0 & 0 & -S_{34} & S_{44} \end{pmatrix}, \quad (2.9)$$

with only six independent elements. Spherical scatterers have a simpler form of Mueller matrix (Perry 1978)

$$\begin{pmatrix} S_{11} & S_{12} & 0 & 0 \\ S_{12} & S_{11} & 0 & 0 \\ 0 & 0 & S_{33} & S_{34} \\ 0 & 0 & -S_{34} & S_{33} \end{pmatrix}, \quad (2.10)$$

with only four independent elements.

### 2.2.2 Conversion from J-matrix to Mueller Matrix

In general, when light interacts through an optical element (e.g., polarizer, retarder, scatter), its response can be described by a  $2 \times 2$  amplitude matrix (J-matrix) (Bickel, Davidson et al. 1976) between incident field  $(E_{\parallel i}, E_{\perp i})$  and scattered field  $(E_{\parallel t}, E_{\perp t})$ :

$$\begin{pmatrix} E_{\parallel t} \\ E_{\perp t} \end{pmatrix} = \begin{pmatrix} J_1 & J_4 \\ J_3 & J_2 \end{pmatrix} \begin{pmatrix} E_{\parallel i} \\ E_{\perp i} \end{pmatrix}. \quad (2.11)$$

The amplitude matrix can be used to derive the Mueller matrix as shown below (Bohren and Huffman 1983). By expanding Eq. (2.11), we have

$$\begin{aligned} E_{\parallel t} &= J_1 E_{\parallel i} + J_4 E_{\perp i} \\ E_{\perp t} &= J_3 E_{\parallel i} + J_2 E_{\perp i} \end{aligned} \quad (2.12)$$

According to its definition, the Stokes parameter I for scattered light is

$$I_t = (J_1 E_{\parallel i} + J_4 E_{\perp i})(J_1^* E_{\parallel i}^* + J_4^* E_{\perp i}^*) + (J_3 E_{\parallel i} + J_2 E_{\perp i})(J_3^* E_{\parallel i}^* + J_2^* E_{\perp i}^*). \quad (2.13)$$

Expansion of the equation above gives

$$I_t = J_1 J_1^* E_{\parallel i} E_{\parallel i}^* + J_1 J_4^* E_{\parallel i} E_{\perp i}^* + J_4 J_1^* E_{\perp i} E_{\parallel i}^* + J_4 J_4^* E_{\perp i} E_{\perp i}^* + J_3 J_3^* E_{\parallel i} E_{\parallel i}^* + J_3 J_2^* E_{\parallel i} E_{\perp i}^* + J_2 J_3^* E_{\perp i} E_{\parallel i}^* + J_2 J_2^* E_{\perp i} E_{\perp i}^*. \quad (2.14)$$

Then we express the Stokes parameters of the incident beam in the following form:

$$\begin{aligned} E_{\parallel i} E_{\parallel i}^* &= \frac{1}{2}(I_i + Q_i); & E_{\perp i} E_{\perp i}^* &= \frac{1}{2}(I_i - Q_i) \\ E_{\parallel i} E_{\perp i}^* &= \frac{1}{2}(U_i - iV_i); & E_{\perp i} E_{\parallel i}^* &= \frac{1}{2}(U_i + iV_i) \end{aligned} \quad (2.15)$$

Therefore, Eq. (2.14) can be rewritten as

$$I_t = \frac{1}{2}[(J_1 J_1^* + J_3 J_3^*)(I_i + Q_i) + (J_4 J_4^* + J_2 J_2^*)(I_i - Q_i) + (J_1 J_4^* + J_3 J_2^*)(U_i - iV_i) + (J_1 J_4^* + J_3 J_2^*)(U_i + iV_i)] \quad (2.16)$$

With the same procedures, the other three Stokes parameters can be obtained:

$$\begin{aligned} Q_t &= \frac{1}{2}[(J_1 J_1^* - J_3 J_3^*)(I_i + Q_i) + (J_4 J_4^* - J_2 J_2^*)(I_i - Q_i) + (J_1 J_4^* - J_3 J_2^*)(U_i - iV_i) + (J_1 J_4^* - J_3 J_2^*)(U_i + iV_i)] \\ U_t &= \frac{1}{2}[(J_1 J_3^* + J_3 J_1^*)(I_i + Q_i) + (J_4 J_2^* + J_2 J_4^*)(I_i - Q_i) + (J_1 J_2^* + J_3 J_4^*)(U_i - iV_i) + (J_4 J_3^* + J_2 J_1^*)(U_i + iV_i)] \\ V_t &= \frac{1}{2}[(J_1 J_3^* - J_3 J_1^*)(I_i + Q_i) + (J_4 J_2^* - J_2 J_4^*)(I_i - Q_i) + (J_1 J_2^* - J_3 J_4^*)(U_i - iV_i) + (J_4 J_3^* - J_2 J_1^*)(U_i + iV_i)] \end{aligned} \quad (2.17)$$

Combine Eq. (2.16) and (2.17)

$$\begin{pmatrix} I_t \\ Q_t \\ U_t \\ V_t \end{pmatrix} = \mathbf{S} \begin{pmatrix} I_i \\ Q_i \\ U_i \\ V_i \end{pmatrix}, \quad (2.18)$$

where (Hovenier 1994)

$$\mathbf{S} = \begin{pmatrix} S_{11} & S_{12} & S_{13} & S_{14} \\ S_{21} & S_{22} & S_{23} & S_{24} \\ S_{31} & S_{32} & S_{33} & S_{34} \\ S_{41} & S_{42} & S_{43} & S_{44} \end{pmatrix} = \mathbf{T} \begin{pmatrix} J_1 J_1^* & J_1 J_4^* & J_4 J_1^* & J_4 J_4^* \\ J_1 J_3^* & J_1 J_2^* & J_4 J_3^* & J_4 J_2^* \\ J_3 J_1^* & J_3 J_4^* & J_2 J_1^* & J_2 J_4^* \\ J_3 J_3^* & J_3 J_2^* & J_2 J_3^* & J_2 J_2^* \end{pmatrix} \mathbf{T}^{-1}, \quad (2.19)$$

and

$$\mathbf{T} = \begin{pmatrix} 1 & 0 & 0 & 1 \\ 1 & 0 & 0 & -1 \\ 0 & 1 & 1 & 0 \\ 0 & i & -i & 0 \end{pmatrix} \text{ and } \mathbf{T}^{-1} = \frac{1}{2} \begin{pmatrix} 1 & 1 & 0 & 0 \\ 0 & 0 & 1 & -i \\ 0 & 0 & 1 & i \\ 1 & -1 & 0 & 0 \end{pmatrix}. \quad (2.20)$$

Since the 16 elements of the Mueller matrix are completely defined if the 4 elements of the amplitude matrix are known, it can be shown that the maximum number of independent elements of a Mueller matrix is 7 since (Abhyanka.Kd and Fymat 1969)

$$J_i = a_i e^{i\theta_i}. \quad (2.21)$$

The independent constants will be  $a_1, a_2, a_3, a_4, (\theta_2 - \theta_1), (\theta_3 - \theta_1)$  and  $(\theta_4 - \theta_1)$ . Theoretically, we only need to measure at most 7 of the 16 elements of Mueller matrix to determine the optical properties of a single scatterer with rigid body although the real cases (i.e., cell scattering measurement) are often more complicated. The derivations of the Mueller matrix for different optical elements (polarizer, retarder and photo elastic modulator) can be found in Appendix A.

### 2.3 The Mie Theory

In this section, we briefly review the Mie theory to derive the Mueller matrix elements for a simple sphere (Bohren and Huffman 1983). These results will be used later in our system calibration. The Mie theory provides one of the analytical solutions of the light scattering problems for a spherical particle embedded in a host medium. An accurate model of light distribution in microsphere suspensions, which are often used as tissue phantoms for calibrating optical instruments and investigating cell and tissue optics, can be established by combining the Mie theory and Monte Carlo simulations (Ma, Lu et al. 2003).

An electromagnetic wave  $(\vec{E}, \vec{H})$  propagating in a homogeneous medium need satisfy the following two wave equations

$$\begin{aligned}\nabla^2 \vec{E} + k^2 \vec{E} &= 0 \\ \nabla^2 \vec{H} + k^2 \vec{H} &= 0\end{aligned}\tag{2.22}$$

where  $k^2 = \omega^2 \epsilon \mu$  is the wave number,  $\omega$  is the angular frequency of the wave,  $\epsilon$  is the permittivity of the medium, and  $\mu$  is the permeability of the medium. And they are derived from the Maxwell's equations below for a monochromatic wave

$$\begin{aligned}\nabla \cdot \mathbf{D} &= 0 \\ \nabla \cdot \mathbf{B} &= 0 \\ \nabla \times \mathbf{E} &= -\frac{\partial \mathbf{B}}{\partial t} \\ \nabla \times \mathbf{B} &= \mu \epsilon \frac{\partial \mathbf{E}}{\partial t}\end{aligned}\tag{2.23}$$

where  $\mathbf{D} = \epsilon \mathbf{E}$ .

Mie (1908) introduced a method to use a scalar function  $\psi$  in a spherical polar coordinates  $(r, \theta, \phi)$  (Fig. 2-2) to construct two vector functions which significantly simplifies the procedures to solve Eq. (2.22):

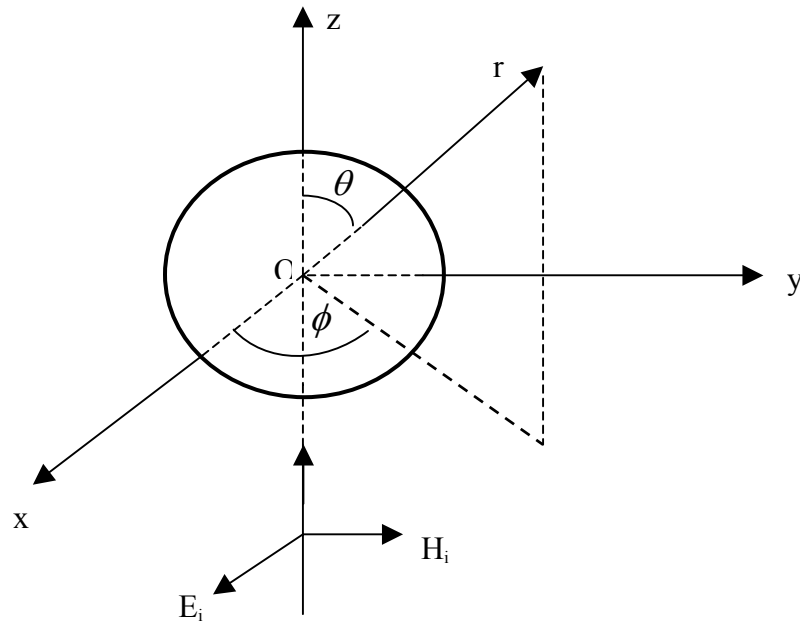


Figure 2-2 Spherical polar coordinate system

$$\begin{aligned}\vec{M} &= \nabla \times (\vec{r}\psi) \\ \vec{N} &= \frac{\nabla \times \vec{M}}{k}\end{aligned}\quad (2.24)$$

where  $\vec{M}$  and  $\vec{N}$  have the properties:

$$\begin{aligned}\nabla \cdot \vec{M} &= 0 \\ \nabla \cdot \vec{N} &= 0 \\ \nabla \times \vec{N} &= k\vec{M} \\ \nabla \times \vec{M} &= k\vec{N}\end{aligned}\quad (2.25)$$

The importance of this method is increased if  $\psi$  is a solution of a scalar wave equation in the spherical polar coordinates such as

$$\frac{1}{r} \frac{\partial}{\partial r} \left( r^2 \frac{\partial \psi}{\partial r} \right) + \frac{1}{r^2 \sin \theta} \frac{\partial}{\partial r} \left( \sin \theta \frac{\partial \psi}{\partial \theta} \right) + \frac{1}{r^2 \sin \theta} \frac{\partial^2 \psi}{\partial \phi^2} + k^2 \psi = 0. \quad (2.26)$$

then  $\vec{M}$  and  $\vec{N}$  will satisfy the vector wave equations:

$$\begin{aligned} \nabla^2 \vec{M} + k^2 \vec{M} &= 0 \\ \nabla^2 \vec{N} + k^2 \vec{N} &= 0 \end{aligned} \quad (2.27)$$

Obviously,  $\vec{M}$  and  $\vec{N}$  have all the required properties of an electromagnetic field. And it will be identical to find solutions for vector wave equations (2.22) and to find scalar solutions to the wave equation (2.26), but the mathematical complexity of the problem is drastically decreased in the latter case.

Solving the plane wave equations is a straightforward but lengthy procedure, and it is not the critical point of this dissertation research. A short outline is given in Appendix B and more details can be found in the Bohren's book. Here we apply the results for the transverse components of the scattered electric field for the case of a spherical particle embedded in a medium (Bohren and Huffman 1983):

$$\begin{aligned} E_{s\theta} &\sim E_0 \frac{e^{ikr}}{-ikr} \cos \phi J_1(\cos \theta) \\ E_{s\phi} &\sim -E_0 \frac{e^{ikr}}{-ikr} \sin \phi J_2(\cos \theta) \end{aligned}, \quad (2.28)$$

where

$$\begin{aligned}
J_1 &= \sum_n \frac{2n+1}{n(n+1)} (a_n \tau_n + b_n \pi_n) \\
J_2 &= \sum_n \frac{2n+1}{n(n+1)} (a_n \pi_n + b_n \tau_n)
\end{aligned} \tag{2.29}$$

Above,  $a_n$ ,  $b_n$  are the scattering coefficients and  $\tau_n$ ,  $\pi_n$  are the angular dependent functions, and their definitions can be found in Appendix B. So we can write the relation between incident and scattered field amplitudes as:

$$\begin{pmatrix} E_{\parallel s} \\ E_{\perp s} \end{pmatrix} = \frac{e^{ik(r-z)}}{-ikr} \begin{pmatrix} J_1 & 0 \\ 0 & J_2 \end{pmatrix} \begin{pmatrix} E_{\parallel i} \\ E_{\perp i} \end{pmatrix}. \tag{2.30}$$

Accordingly, the Mueller matrix is given by:

$$\begin{pmatrix} I_t \\ Q_t \\ U_t \\ V_t \end{pmatrix} = \frac{1}{k^2 r^2} \begin{pmatrix} S_{11} & S_{12} & 0 & 0 \\ S_{12} & S_{11} & 0 & 0 \\ 0 & 0 & S_{33} & S_{34} \\ 0 & 0 & -S_{34} & S_{33} \end{pmatrix} \begin{pmatrix} I_i \\ Q_i \\ U_i \\ V_i \end{pmatrix}, \tag{2.31}$$

and

$$\begin{aligned}
S_{11} &= \frac{1}{2} (|J_1|^2 + |J_2|^2), & S_{12} &= \frac{1}{2} (|J_1|^2 - |J_2|^2), \\
S_{33} &= \frac{1}{2} (J_1^* J_2 + J_1 J_2^*), & S_{34} &= \frac{i}{2} (J_1^* J_2 - J_1 J_2^*).
\end{aligned} \tag{2.32}$$

## 2.4 The Rayleigh Scattering Model

The Rayleigh scattering model is applicable when the size of the scattering particles is much smaller than the wavelength of the incident light. For a simple derivation, spherical scatterers are assumed and we start from the first few terms of scattering coefficients  $a_n$  and  $b_n$  (Antosiewicz 1964; Bohren and Huffman 1983),

$$\begin{aligned}
a_1 &= -\frac{2ix^3}{3} \frac{m^2-1}{m^2+3} - \frac{2ix^5}{5} \frac{(m^2-1)(m^2-2)}{(m^2+2)^2} + \frac{4x^6}{9} \left( \frac{m^2-1}{m^2+2} \right)^2 + O(x^7); \\
b_1 &= -\frac{ix^5(m^2-1)}{3} + O(x^7); \\
a_2 &= -\frac{ix^5}{15} \frac{m^2-1}{2m^2+3} + O(x^7); \\
b_2 &= O(x^7),
\end{aligned} \tag{2.33}$$

where  $m$  is the ratio of refractive index between the particle and medium and is equal to  $n_1/n$ ,  $x$  is the size parameter defined as,

$$x = \frac{2\pi na}{\lambda}, \tag{2.34}$$

where  $a$  is the radius of the spherical sample. The higher-order scattering coefficients are omitted. The amplitude matrix elements to the third term ( $x^3$ ) are

$$J_1 = \frac{3}{2} a_1 \cos \theta, \quad J_2 = \frac{3}{2} a_1. \tag{2.35}$$

where

$$a_1 = -\frac{i2x^3}{3} \frac{m^2-1}{m^2+2}. \tag{2.36}$$

The corresponding scattering matrix is then obtained as

$$\frac{9|\alpha|^2}{8k^2 r^2} \begin{pmatrix} 1 + \cos^2 \theta & \cos^2 \theta - 1 & 0 & 0 \\ \cos^2 \theta - 1 & 1 + \cos^2 \theta & 0 & 0 \\ 0 & 0 & 2 \cos \theta & 0 \\ 0 & 0 & 0 & 2 \cos \theta \end{pmatrix}. \tag{2.37}$$

## 2.5 The Rayleigh-Gans Scattering Model

For an arbitrarily shaped particle whose refractive index satisfies the following condition:

$$|m - 1| \ll 1, \quad (2.38)$$

where  $m$  is the complex refractive index of the particle relative to that of the host medium. The Rayleigh-Gans Model (Turner 1973; Bohren and Huffman 1983) may be used with which the amplitude matrix elements can be approximated by a suitable integration of  $J_i$  [the J-matrix elements] over the volume of the particle. Consider a plane wave propagating in the  $z$  direction and let it be scattered by a particle located at the origin of the coordinate system. The relation between the incident and scattered field can be written as

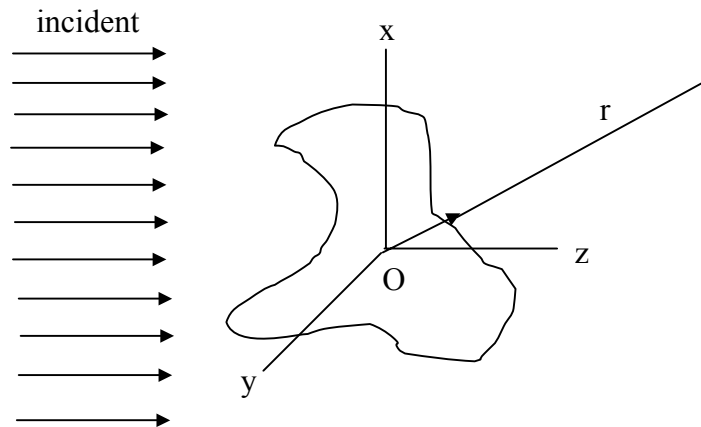


Figure 2-2 Light scattering by an arbitrary particle

$$\begin{pmatrix} E_{\parallel s} \\ E_{\perp s} \end{pmatrix} = \frac{e^{ik \cdot r}}{r} \begin{pmatrix} J_1(\theta, \phi) & J_3(\theta, \phi) \\ J_4(\theta, \phi) & J_2(\theta, \phi) \end{pmatrix} \begin{pmatrix} E_{\parallel i} \\ E_{\perp i} \end{pmatrix}, \quad (2.39)$$

where  $E_{\parallel i, \perp i}$  and  $E_{\parallel s, \perp s}$  are the parallel and perpendicular components of incident and scattered field measured relative to the scattering plane, respectively.

For the case without scattering, the electric vector for the plane wave can be written as

$$\mathbf{E}(\mathbf{k}, \nu, \mathbf{r}) = \mathbf{E}_0(\mathbf{k}, \nu, \mathbf{r}) \equiv \xi_\nu(\mathbf{k}) e^{i\mathbf{k}\cdot\mathbf{r}}. \quad (2.40)$$

where  $\mathbf{k}$  is the incident direction,  $\nu$  is the polarization and  $\xi_\nu(\mathbf{k})$  is the unit polarization vector. While considering the scattering by a particle of the same incident wave, the electric vector is modified as

$$\mathbf{E}(\mathbf{k}, \nu, \mathbf{r}) = E_0(\mathbf{k}, \nu, \mathbf{r}) + \mathbf{E}_{\text{sc}}(\mathbf{k}, \nu, \mathbf{r}). \quad (2.41)$$

where asymptotically (Turner 1973)

$$\lim_{r \rightarrow \infty} \mathbf{E}_{\text{sc}}(\mathbf{k}, \nu, \mathbf{r}) = \left( \frac{e^{i\mathbf{k}\cdot\mathbf{r}}}{r} \right) \sum_{\nu'=\perp}^{\parallel} \xi_{\nu'}(\mathbf{k}') J(\mathbf{k}', \nu', \mathbf{k}, \nu). \quad (2.42)$$

Above,  $\mathbf{k}'$ ,  $\nu'$  is the direction and polarization after scattering as we defined  $\mathbf{k}$  and  $\nu$ , respectively. To be equivalent to Eq. (2.39), we must have (look at the scattered light in the  $\theta$  and  $\phi$  direction)

$$\mathbf{k} = k\hat{z}; \mathbf{k}' = k(\sin\theta \cos\phi\hat{x} + \sin\theta \sin\phi\hat{y} + \cos\theta\hat{z}), \quad (2.43)$$

where  $\hat{x}, \hat{y}, \hat{z}$  are unit vectors along the x, y, z axes. Thus the polarization vector can be determined as

$$\begin{aligned}
\xi_{\parallel}(\mathbf{k}) &= \cos \phi \hat{x} + \sin \phi \hat{y} \\
\xi_{\parallel}(\mathbf{k}') &= \cos \theta \cos \phi \hat{x} + \cos \theta \sin \phi \hat{y} - \sin \theta \hat{z} \\
\xi_{\perp}(\mathbf{k}) &= -\sin \phi \hat{x} + \cos \phi \hat{y} \\
\xi_{\perp}(\mathbf{k}') &= -\sin \phi \hat{x} + \cos \phi \hat{y}
\end{aligned} \tag{2.44}$$

And the elements of the amplitude matrix in Eq. (2.39) can also be obtained as:

$$\begin{aligned}
J_1(\theta, \phi) &= J(\mathbf{k}', \parallel; \mathbf{k}, \parallel); J_2(\theta, \phi) = J(\mathbf{k}', \perp; \mathbf{k}, \perp) \\
J_3(\theta, \phi) &= J(\mathbf{k}', \parallel; \mathbf{k}, \perp); J_4(\theta, \phi) = J(\mathbf{k}', \perp; \mathbf{k}, \parallel)
\end{aligned} \tag{2.45}$$

We describe the right side of the equations above as integrals over the volume  $V$  of the scattering particle with using Maxwell's equations and have the following:

$$J(\mathbf{k}', \nu', \mathbf{k}, \nu) = \frac{k^2}{4\pi} \sum_{i,j=1}^3 \int_V d^3r E_{0i}^*(\mathbf{k}', \nu', \mathbf{k}, \nu) |m(\mathbf{r}) - 1| E_{0j}(\mathbf{k}, \nu, \mathbf{k}, \nu) \tag{2.46}$$

where  $m(\mathbf{r})$  is the relative refractive index tensor.  $\mathbf{E}$  and  $\mathbf{E}_0$  are defined by Eq. (2.41) and (2.40), respectively.

Applying the Rayleigh-Gans approximation as Eq. (2.38), Eq. (2.46) gives out the elements of the amplitude matrix as:

$$J(\mathbf{k}', \nu', \mathbf{k}, \nu) = \frac{k^2}{4\pi} \xi_{\nu'}^{\dagger}(\mathbf{k}') \cdot \xi_{\nu}(\mathbf{k}) \left[ \int_V e^{i(\mathbf{k}-\mathbf{k}')\cdot\mathbf{r}} (m(\mathbf{r}) - 1) d^3r \right]. \tag{2.47}$$

Combining Eq. (2.47) with Eq. (2.43) and (2.44), we have

$$\begin{aligned}
J_1(\theta, \phi) &= \left(\frac{k^2}{4\pi}\right) \left[ \int_V e^{i(\mathbf{k}-\mathbf{k}')\cdot\mathbf{r}} (m(\mathbf{r}) - 1) d^3r \right] \cos \theta \\
J_2(\theta, \phi) &= \left(\frac{k^2}{4\pi}\right) \int_V e^{i(\mathbf{k}-\mathbf{k}')\cdot\mathbf{r}} (m(\mathbf{r}) - 1) d^3r \\
J_3(\theta, \phi) &= J_4(\theta, \phi) = 0
\end{aligned} \tag{2.48}$$

Using the conversion from J-matrix to Mueller matrix, we can obtain

$$S(\theta, \phi) = \frac{k^4}{32\pi^2} \left| \int_V e^{i(\mathbf{k}-\mathbf{k}')\cdot\mathbf{r}} (m(\mathbf{r})-1) d^3r \right|^2 \begin{pmatrix} 1 + \cos^2 \theta & \cos^2 \theta - 1 & 0 & 0 \\ \cos^2 \theta - 1 & 1 + \cos^2 \theta & 0 & 0 \\ 0 & 0 & 2 \cos \theta & 0 \\ 0 & 0 & 0 & 2 \cos \theta \end{pmatrix}. \quad (2.49)$$

## 2.6 The Finite-Difference Time-Domain (FDTD) Method

Even though the FDTD modeling is not part of this dissertation research, we make a brief discussion (provided by our colleagues, see the references) of its principle here to help readers to understand the comparison between the measured and FDTD calculated Mueller matrix elements in later chapters. More details on the FDTD method can be found in (Brock, Hu et al. 2005; Lu, Yang et al. 2005; Brock, Hu et al. 2006).

In the FDTD method, light scattering by a biological cell is treated as an plane electromagnetic wave incident on the cell in an infinitely large host medium (Taflove and Hagness 2000). The incident light is described by the electromagnetic fields of  $(\mathbf{E}_i, \mathbf{B}_i)$  propagating in the direction of  $\mathbf{k}_0$  and the scattered light by the fields of  $(\mathbf{E}_s, \mathbf{B}_s)$  in the direction of  $\mathbf{k}$ . The host medium is described by a dielectric constant  $\epsilon_h$  while the cell is characterized by  $\epsilon(\mathbf{r}, \omega)$ , a dielectric function of spatial location  $\mathbf{r}$  and frequency of incident light, to represent its shape and optical structure. There are four major steps in obtaining observable information on the scattering properties of a scatterer with the FDTD method: calculation of the near-field in the time domain using the FDTD method; transformation of the near field from the time domain to the frequency domain using the discrete Fourier transform; transformation of the near field to the scattered field in the far zone in the frequency domain using the Green's identity; and calculation of the scattering

data in terms of the Mueller matrix elements and other parameters such as the scattering cross section (Brock, Hu et al. 2005; Lu, Yang et al. 2005; Brock, Hu et al. 2006).

In the FDTD calculation of near-fields, the two curl equations in the Maxwell's equations are converted into a set of finite difference equations by discretizing time into finite steps and space in the region containing the cell and its host medium into rectangular grid cells. According to the algorithm of Yee (Yee 1966), the six components of the electromagnetic fields are arranged within each grid cell at staggered locations in space. Examples of the finite-difference equations for  $E_x$ , and  $H_x$  are given by (Brock, Hu et al. 2005; Lu, Yang et al. 2005)

$$\mathbf{H}_x|_{l,j,k}^{n+1/2} = \mathbf{H}_x|_{l,j,k}^{n-1/2} + \frac{\Delta t}{\mu_0} \left( \frac{\mathbf{E}_y|_{l,j,k+1/2}^n - \mathbf{E}_y|_{l,j,k-1/2}^n}{\Delta z} - \frac{\mathbf{E}_z|_{l,j+1/2,k}^n - \mathbf{E}_z|_{l,j-1/2,k}^n}{\Delta y} \right); \quad (2.50)$$

$$\mathbf{E}_x|_{l,j,k}^{n+1} = \mathbf{E}_x|_{l,j,k}^n + \frac{\Delta t}{\varepsilon_{l,j,k}} \left( \frac{\mathbf{H}_z|_{l,j+1/2,k}^{n+1/2} - \mathbf{H}_z|_{l,j-1/2,k}^{n+1/2}}{\Delta y} - \frac{\mathbf{H}_y|_{l,j,k+1/2}^{n+1/2} - \mathbf{H}_y|_{l,j,k-1/2}^{n+1/2}}{\Delta z} \right). \quad (2.51)$$

Equations for the remaining electric and magnetic components are similar. Here  $\Delta t$  is the time step size,  $\Delta x$ ,  $\Delta y$ , and  $\Delta z$  are the grid cell dimensions in the  $x$ ,  $y$ , and  $z$  directions, respectively. The index  $i$ ,  $j$ ,  $k$ , and  $n$  is the number of increments taken in the  $x$ ,  $y$ ,  $z$ , and  $t$  directions, respectively. A  $1/2$  superscript or subscript denotes a half-step increment in the appropriate direction. In the calculations, this set of explicit finite-difference equations is solved in a time marching sequence with the electric and magnetic fields being updated alternately at half time increments.

As discussed previously, to fully characterize the scattering properties of a scatterer, the independent nonzero elements of the Mueller matrix need to be calculated. These elements are functions of the elements of the amplitude matrix (J-matrix), and the latter relates the far zone scattering field to the incident field in the matrix form when the fields are resolved into components parallel and perpendicular to the scattering plane. By using two incident waves of independent polarization in the  $x$  and  $y$  directions, the J-matrix elements can be calculated as (Yang and Liou 1996)

$$J = \begin{pmatrix} F_{\parallel,x} & F_{\parallel,y} \\ F_{\perp,x} & F_{\perp,y} \end{pmatrix} \begin{pmatrix} \cos \theta & \sin \theta \\ \sin \theta & -\cos \theta \end{pmatrix}; \quad (2.52)$$

and

$$\begin{pmatrix} F_{\parallel,x} \\ F_{\perp,x} \end{pmatrix} = \frac{-ik^3}{4\pi} \int_V \left( \frac{\varepsilon(\mathbf{r}', \omega)}{\varepsilon_0} - 1 \right) \begin{bmatrix} E_{\parallel,x}(\mathbf{r}', \omega) \\ E_{\perp,x}(\mathbf{r}', \omega) \end{bmatrix} e^{-ik \cdot \mathbf{r}'} d^3r$$

$$\begin{pmatrix} F_{\parallel,y} \\ F_{\perp,y} \end{pmatrix} = \frac{-ik^3}{4\pi} \int_V \left( \frac{\varepsilon(\mathbf{r}', \omega)}{\varepsilon_0} - 1 \right) \begin{bmatrix} E_{\parallel,y}(\mathbf{r}', \omega) \\ E_{\perp,y}(\mathbf{r}', \omega) \end{bmatrix} e^{-ik \cdot \mathbf{r}'} d^3r, \quad (2.53)$$

where  $\theta$  is the angle between  $\mathbf{k}$  and  $\mathbf{k}_0$  and the subscript  $x$  or  $y$  indicates an incident light polarized in the  $x$  or  $y$  direction, respectively. To calculate the angular dependence of the Mueller matrix elements, the four volume integrals in Eq. (2.53) must be evaluated for each scattering direction, which is time consuming for large scatterers.

## 2.7 The Effective Medium Theory

Effective medium theory was first proposed by Maxwell-Garnett (1904) to understand the dispersion of refractive index for molecular solutions, and the results of this effective medium approximations (EMA) are still frequently used today in many

fields (Niklasson, Granqvist et al. 1981). A basic assumption of EMA is that the typical size of an inhomogeneity,  $x$ , must be much smaller than the wavelength  $\lambda$  of the illuminated light,  $x \ll \lambda$ . This basic limitation of EMAs is usually expressed in the form of size parameter  $d$  that relates the inclusion's characteristic dimension  $a$  to the wavelength in the host medium:

$$d = \frac{\pi a n_r}{\lambda} \ll 1, \quad (2.54)$$

where  $n_r$  is the real part of the refractive index of host material and  $\lambda$  is the wavelength,  $a$  is the characteristic dimension of the inclusion. However, this requirement cannot be met in many situations such as the study of the biological tissues. Consequently, an ongoing research is to extend the region of applicability of EMA to larger sizes of inclusions, which is generally called extended effective medium approximations (Michael I. Mishchenko 2000).

As one of the most popular EMAs, Bruggeman mixing rules (Bruggeman, 1935) have been used widely since it provides a good and yet simple model to explain experimental data in many cases (Perrin and Lamy 1990; Ossenkopf 1991). Compared with the Maxwell-Garnett theory, Bruggeman made a significant improvement with applying the symmetrical fashion in this theory. The effective dielectric constant of a composite medium depends in general on the size and shape of the individual inclusions and on the distribution form for the inclusions throughout the composite material. The usual derivation of EMAs is based on electrostatic considerations of the electric field and

displacement within the heterogeneous material (Bruggeman, 1935). The appropriate expressions for effective dielectric constants are also valid at finite (nonzero) frequencies if the size of the inclusions is much smaller than the wavelength within the host material.

A derivation of the classical EMAs can be obtained by applying the requirement that the scattering amplitude  $A$  vanishes in the forward direction for the case that spherical inclusions are embedded in an effective medium (Stroud E. 1978; van de Hulst 1957; Bohren et al. 1979; Niklasson, Granqvist et al. 1981)

$$A(\theta_s = 0) = 0, \quad (2.55)$$

where  $\theta_s$  is the scattering angle. This assumption is necessary if the effective dielectric function is introduced to describe the wave propagation because of requirement on self-consistency (Stroud E. 1978).

For a simple example derivation, we consider a heterogeneous medium consisting of a binary inclusion of grains with complex dielectric constants  $\epsilon_1$  and  $\epsilon_2$  and volume fractions  $f_1$  and  $f_2$ . The Mie scattering formalism is used when the grains are spherical and the solution obtained at the forward direction of the scattering angle  $\theta_s = 0$  is

$$A(0) = \frac{1}{2} \sum_{n=1}^{\infty} (2n+1)(a_n + b_n), \quad (2.56)$$

where  $a_n$  and  $b_n$  are the Mie scattering coefficients as we met in the early section, and they depend on the size of the inclusions and their relative refractive indices to the medium in which they are embedded.

For particles with a size in the Rayleigh scattering region, only the first element of the amplitude matrix  $J_j$  sustains. The first term of the scattering coefficient  $a_1$  of a homogeneous sphere can be expanded in a power series of the size parameter. By keeping only the leading term as we did previously, the scattering amplitude of grains can be written as a sum of contributions from individual grains that have refractive indices  $n_1$  and  $n_2$  and corresponding volume fractions  $f_1$  and  $f_2$  embedded in an effective medium that has an effective dielectric constant  $\epsilon_{\text{eff}}$ . With all these conditions, the vanishing forward scattering amplitude has the following form:

$$A(0) = -i \left( \frac{2\pi r}{\lambda} \right)^3 \epsilon_{\text{eff}}^{3/2} \left[ f_1 \frac{\epsilon_1 - \epsilon_{\text{eff}}}{\epsilon_1 + 2\epsilon_{\text{eff}}} + f_2 \frac{\epsilon_2 - \epsilon_{\text{eff}}}{\epsilon_2 + 2\epsilon_{\text{eff}}} \right] = 0. \quad (2.57)$$

Solving the equation above leads directly to the Bruggeman mixing rule:

$$f_1 \frac{\epsilon_1 - \epsilon_{\text{eff}}}{\epsilon_1 + 2\epsilon_{\text{eff}}} + f_2 \frac{\epsilon_2 - \epsilon_{\text{eff}}}{\epsilon_2 + 2\epsilon_{\text{eff}}} = 0, \quad (2.58)$$

which provides an equation to calculate the effective dielectric constant or refractive index of the mixed medium.

## 2.8 Refractive Index Determination

Boundaries of a homogeneous biological tissue or interfaces within a heterogeneous tissue play a unique role in our understanding of tissue optics. On one hand, light distribution within a tissue for a given configuration of source has to be solved in terms of specific boundary value problems and thus appropriate boundary conditions are required. On the other hand, detection of light signals external to the tissue invariably

involves light transportation through tissue boundary and the effect of boundary needs to be accounted for to accurately determine the optical parameters of the tissue. In the cases where light scattering is negligible, light interaction with interfaces can be clearly understood in terms of refractive index mismatch based on the theory of classical electrodynamics (Jackson 1975).

With a reflectometry system to be described in Chapter 3, the curves of coherent reflectance ( $R_s$  or  $R_p$ ) versus incident angle can be measured from a glass-sample interface formed by holding a turbid sample against the base of a glass prism. The complex index of refraction of the turbid sample  $n = n_r + in_i$  at each wavelength is obtained with a method of least-squares based on the Marquardt-Levenberg nonlinear regression algorithm (Marquardt 1963) by fitting the calculated values,  $\tilde{R}_s(\theta)$  and  $\tilde{R}_p(\theta)$ , to the measured values of  $R_s$  and  $R_p$ , respectively, using the known index  $n_0$  of the prism. The calculated coherent reflectance at the prism-sample interface is given by the Fresnel's equations as (Jackson 1999)

$$\tilde{R}_s(\theta) = \left| \frac{n_0 \cos \theta - \sqrt{(n_r + in_i)^2 - n_0^2 \sin^2 \theta}}{n_0 \cos \theta + \sqrt{(n_r + in_i)^2 - n_0^2 \sin^2 \theta}} \right|^2; \quad (2.59)$$

and

$$\tilde{R}_p(\theta) = \left| \frac{(n_r + in_i)^2 \cos \theta - n_0 \sqrt{(n_r + in_i)^2 - n_0^2 \sin^2 \theta}}{(n_r + in_i)^2 \cos \theta + n_0 \sqrt{(n_r + in_i)^2 - n_0^2 \sin^2 \theta}} \right|^2. \quad (2.60)$$

The fitting error between the measured and calculated coherent reflectance is described by a coefficient of determination,  $R^2$ , ranging between 0 and 1, and is defined by

$$R^2 = 1 - \frac{\sum_{i=1}^N (R_i - \tilde{R}_i)^2}{\sum_{i=1}^N (R_i - \bar{R})^2}, \quad (2.61)$$

where  $R_i$  and  $\tilde{R}_i$  denotes the measured and calculated reflectance at  $i$ th angle of incidence  $\theta_i$ , respectively, and  $\bar{R}$  is the mean value of measured reflectance over  $N$  values of  $\theta$ .

## **Chapter 3 Experimental Methods**

In this chapter, the experimental designs are presented for the measurement of Mueller matrix elements of cellular scatters with a photoelastic modulator (PEM) based goniometer system and the measurement of refractive indices for turbid samples and skin tissues with a reflectometry system. The procedures for sample preparation are also described.

### **3.1 PEM Based Goniometer System**

The polarized light beam can be represented by the Stokes parameters (Bohren and Huffman 1983). If light is scattered by an ensemble of particles, the Stokes vectors of the incident beam and scattered beam are, for each scattering angle  $\theta$ , related by a set of 4x4 Mueller matrices representing the scatterers and optical devices processing the incident and scattered beams. The elements of the Mueller matrix of the scatterers depend on the scattering angles and contain information about the size parameter, shape, refractive index, and structure of the scatters (Kuik, Stammes et al. 1991; Volten, de Haan et al. 1998).

#### **3.1.1 The Measurement of Muller Matrix Elements**

The experimental setup to measure the scattering matrix elements of the samples is depicted in Fig. 3-1. The incident laser beam at wavelength  $\lambda$  passes through a linear polarizer (PGM5210, Casix) and a PEM (PEM90, Hinds Instrument), whose working principle can be found in Appendix A, before being scattered by an ensemble of

randomly oriented scatterers, and then the scattered light may be analyzed by a quarter-wave plate (Model 5540, New Focus) and a polarizer (PRH8010, Casix) before it arrives at a photomultiplier tube (PMT) (R6356, Hamamatsu).

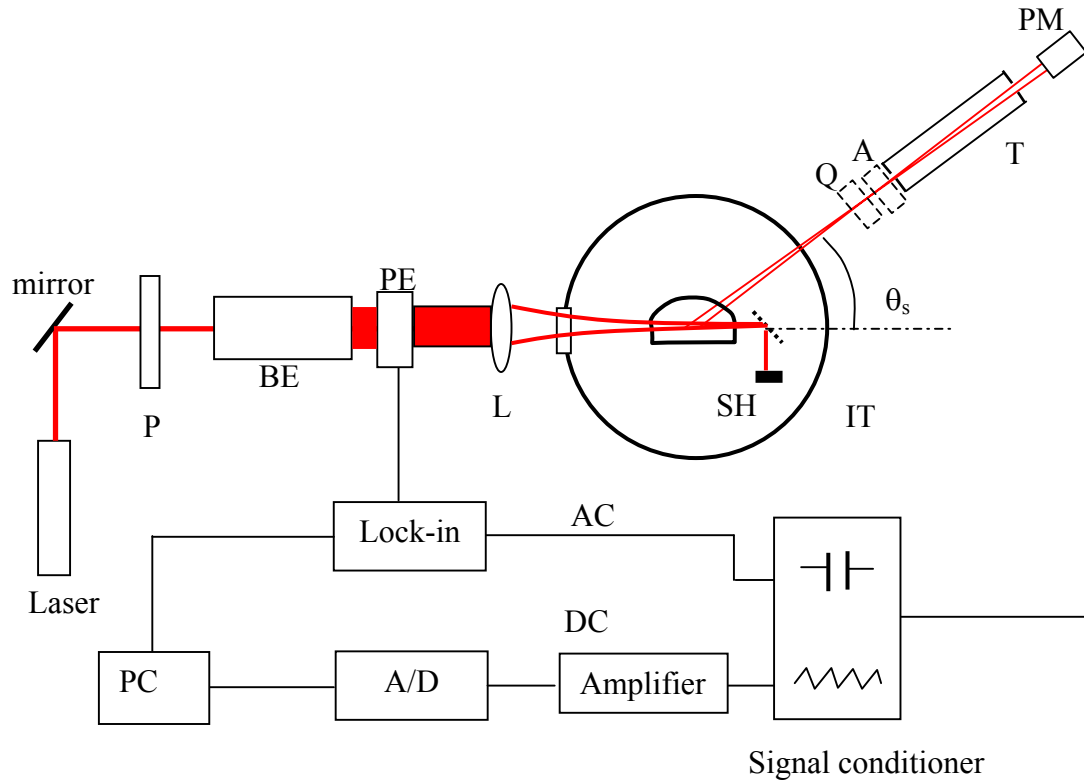


Figure 3-1 Schematic of the experimental setup: P: polarizer, BE: Beam expander, PE: PE modulator; B: beam expander, L: focusing lens, SH: sample holder, IT: immersion tank, Q: quarter-wave plate, A: analyzer, T: apertured tube, PM: photomultiplier, A/D: analog-to-digital converter, PC: Personal Computer.

With the Stokes parameters, the irradiance of the scattered light reaching the PMT can be written as (Kuik, Stammes et al. 1991)

$$\mathbf{I}_s(\Theta) = c_1 \mathbf{A}(\gamma_A) \mathbf{Q}(\gamma_Q) \mathbf{S}(\Theta) \mathbf{M}(\gamma_M) \mathbf{P}(\gamma_P) \mathbf{I}_i, \quad (3.1)$$

where  $\mathbf{I}_i$  is the Stokes vector of the beam leaving the light source;  $c_1$  is a scaling constant;  $\mathbf{A}$ ,  $\mathbf{Q}$ ,  $\mathbf{S}$ ,  $\mathbf{M}$ ,  $\mathbf{P}$  are the Mueller matrices of analyzer, quarter-wave plate, sample, modulator, and polarizer, respectively.  $\gamma_A$ ,  $\gamma_Q$ ,  $\gamma_M$  and  $\gamma_P$  are the angles between optical axis of each device and the reference plane, defined as the plane containing the incident and scattered light and measured anticlockwise from the reference plane when looking in the direction of beam propagation.

The elements of  $\mathbf{S}$  can be determined with different configurations of the components. Two configuration examples are given below.

**Configuration 1: one polarizer ( $0^\circ$ ) and one modulator ( $45^\circ$ )**

In this configuration, the modulator is oriented at  $45^\circ$  with respect to the scattering plane and the polarizer P is oriented at  $0^\circ$  (Fig. 3-2):

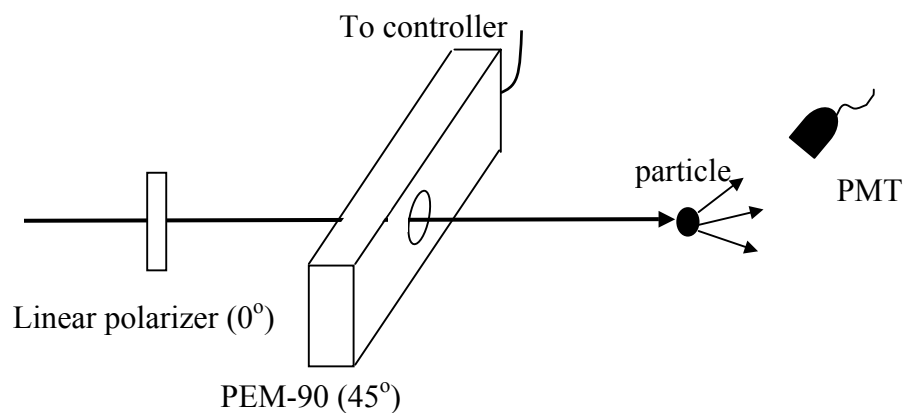


Figure 3-2 One polarizer and modulator

The Stokes vectors of the light as it is emerging from the modulator are given by the matrix product below (Bohren and Huffman 1983)

$$I_i = \frac{1}{2} \underbrace{\begin{pmatrix} 1 & 0 & 0 & 0 \\ 0 & \cos \phi & 0 & -\sin \phi \\ 0 & 0 & 1 & 0 \\ 0 & \sin \phi & 0 & \cos \phi \end{pmatrix}}_c \underbrace{\begin{pmatrix} 1 & 1 & 0 & 0 \\ 1 & 1 & 0 & 0 \\ 0 & 0 & 0 & 0 \\ 0 & 0 & 0 & 0 \end{pmatrix}}_b \underbrace{\begin{pmatrix} 1 \\ 0 \\ 1 \\ 0 \end{pmatrix}}_a = \frac{1}{2} \begin{pmatrix} 1 \\ \cos \phi \\ 0 \\ \sin \phi \end{pmatrix}, \quad (3.2)$$

where  $\phi$  is the instantaneous angle of retardation for the modulator ( $\phi = \phi_0 \sin \omega t$ ). Matrix  $a$  is for the polarized laser beam, matrix  $b$  is the expression for the polarizer at  $0^\circ$ , and matrix  $c$  is for the modulator at  $45^\circ$ . The light is scattered by the scatterer ( $\mathbf{S}$ ) before it reaches the detector and this can be expressed by

$$I_s = \mathbf{S} I_i; \quad (3.3)$$

$$I_s = \begin{pmatrix} I_s \\ Q_s \\ U_s \\ V_s \end{pmatrix} = \frac{1}{2} \begin{pmatrix} S_{11} & S_{12} & S_{13} & S_{14} \\ S_{21} & S_{22} & S_{23} & S_{24} \\ S_{31} & S_{32} & S_{33} & S_{34} \\ S_{41} & S_{42} & S_{43} & S_{44} \end{pmatrix} \begin{pmatrix} 1 \\ \cos \phi \\ 0 \\ \sin \phi \end{pmatrix} = \frac{1}{2} \begin{pmatrix} S_{11} + S_{12} \cos \phi + S_{14} \sin \phi \\ S_{21} + S_{22} \cos \phi + S_{24} \sin \phi \\ S_{31} + S_{32} \cos \phi + S_{34} \sin \phi \\ S_{41} + S_{42} \cos \phi + S_{44} \sin \phi \end{pmatrix}. \quad (3.4)$$

And

$$I_s = \frac{1}{2} (S_{11} + S_{12} \cos \phi + S_{14} \sin \phi), \quad (3.5)$$

where

$$\begin{aligned} \sin \phi &= \sin(\phi_0 \sin \omega t) = 2 \sum_{k=1}^{\infty} J_{2k-1}(\phi_0) \sin(2k-1)\omega t, \\ \cos \phi &= \cos(\phi_0 \sin \omega t) = J_0(\phi_0) + 2 \sum_{l=1}^{\infty} J_{2l}(\phi_0) \cos 2l\omega t. \end{aligned} \quad (3.6)$$

Substitute Eq. (3.6) into Eq. (3.5) with only terms up to  $2\omega$ :

$$I_s = c[S_{11} + 2J_1(\phi_0)S_{14} \sin \omega t + 2J_2(\phi_0)S_{12} \cos 2\omega t + S_{12}J_0(\phi_0)], \quad (3.7)$$

where  $c$  is a scaling constant for a specified optical arrangement and higher order terms with  $\sin(2k-1)\omega t$  and  $\cos 2l\omega t$  have been omitted. It turns out to be convenient to adjust the amplitude of the modulation so that  $J_0(\phi_0) = 0$ . With this  $\phi_0$  value, we have  $J_1(\phi_0) = 0.5192$ ,  $J_2(\phi_0) = 0.4318$ , and then Eq. (3.7) can be rewritten as

$$I_s = c[S_{11} + 1.0384S_{14} \sin \omega t + 0.8636S_{12} \cos 2\omega t]. \quad (3.8)$$

Obviously,  $S_{11}$  is related to the DC signal,  $S_{14}$  to the  $\omega$  signal and  $S_{12}$  to the  $2\omega$  signal.

### Configuration 2: Two polarizers ( $0^\circ$ and $45^\circ$ ) and one modulator ( $45^\circ$ )

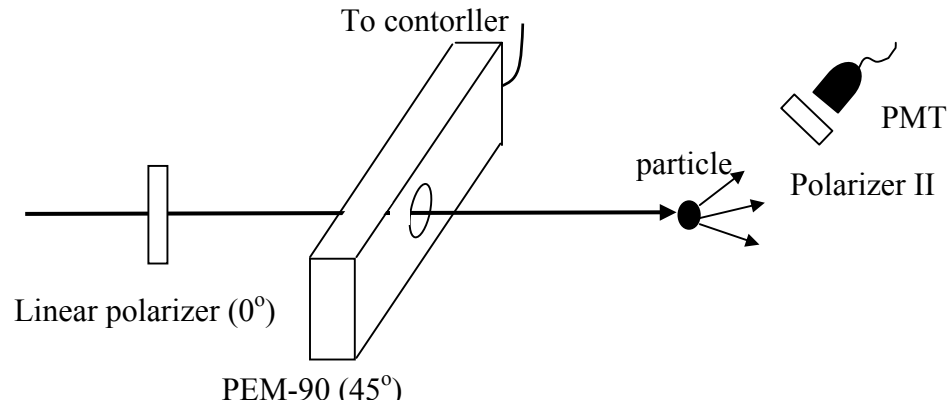


Figure 3-3 Two polarizers and one modulator

The only difference of configuration 2 from configuration 1 is that we add another polarizer II, which is oriented at  $45^\circ$  with respect to the scattering plane and is placed in front of the PMT. Accordingly, we have

$$I_s(\Theta) = c_1 A(\gamma_A) S(\Theta) M(\gamma_M) P(\gamma_P) I_i. \quad (3.9)$$

The product of last 4 elements on the right side of the equation above is given by

$$I_s = \frac{1}{2} c_1 A(\gamma = 45^\circ) \begin{pmatrix} S_{11} + S_{12} \cos \phi + S_{14} \sin \phi \\ S_{21} + S_{22} \cos \phi + S_{24} \sin \phi \\ S_{31} + S_{32} \cos \phi + S_{34} \sin \phi \\ S_{41} + S_{42} \cos \phi + S_{44} \sin \phi \end{pmatrix}. \quad (3.10)$$

After the matrix multiplication, we have

$$I_s = \begin{pmatrix} I_s \\ Q_s \\ U_s \\ V_s \end{pmatrix} = \frac{1}{2} c_1 \begin{pmatrix} S_{11} + S_{31} + (S_{12} + S_{32}) \cos \phi + (S_{14} + S_{34}) \sin \phi \\ 0 \\ S_{11} + S_{31} + (S_{12} + S_{32}) \cos \phi + (S_{14} + S_{34}) \sin \phi \\ 0 \end{pmatrix}. \quad (3.11)$$

And again,

$$I_s = c[S_{11} + S_{31} + (S_{12} + S_{32}) \cos \phi + (S_{14} + S_{34}) \sin \phi]. \quad (3.12)$$

Following the same procedures as in configuration 1, the following can be derived

$$I_s = c[S_{11} + S_{31} + 1.0384(S_{14} + S_{34}) \sin \omega t + 0.8636(S_{12} + S_{32}) \cos 2\omega t]. \quad (3.13)$$

Hence,  $S_{11} + S_{31}$  is related to the DC signal,  $S_{14} + S_{34}$  to the  $\omega$  signal and  $S_{12} + S_{32}$  to the  $2\omega$  signal.

### 3.1.2 Signal Processing

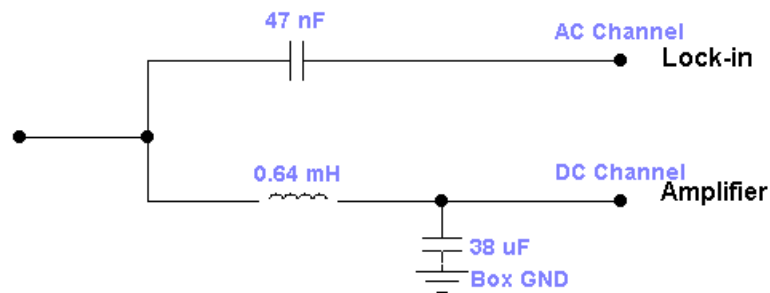


Figure 3-4 Schematic diagram of the signal conditioner

The AC signal ( $1\omega$  and  $2\omega$ ) from the PMT is separated from the DC part by a signal conditioner (Fig. 3-4). The DC component is input to the AD board (KPCI-3100, Keithley) after a preamplifier (DLPCA-200, FEMTO) and the AC component is connected to two lock-in amplifiers (SR830, Stanford Research Systems) with two different reference frequencies ( $1\omega$  and  $2\omega$ ). The loss of DC,  $1\omega$  and  $2\omega$  component together with phase shift through the separation is listed in Table 3-1. The ratio ( $\eta_1$ ) of the losses between DC and AC is obtained from this table by a simple division.

**Table 3-1** Signal attenuation and phase shift in the signal conditioner

Signal	Signal Ratio (r)	Phase shift ( $\phi'$ ) ( $^\circ$ )
DC	1	---
1f	$1.38 \pm 0.15$	341
2f	$1.11 \pm 0.15$	347

The DC signal right after the separation is directed into an amplifier with a gain ( $\eta_2$ ) which need be taken into account when normalizing the matrix elements to  $S_{11}$ . The signal collection with the AD board for the DC component and Lock-ins for the AC component brings another factor ( $\eta_3$ ) to the normalization. Considering all the three factors above, we have

$$c_{2(3)} = c_1 \cdot \eta_1 \cdot \eta_2 \cdot \eta_3, \quad (3.14)$$

where  $c_1$  is the scaling constant for DC signal, and  $c_2$  and  $c_3$  are the normalization constants for the second harmonic signal ( $2\omega$ ) and the first harmonic signal ( $\omega$ ) to the DC signal, respectively. The calibrations were carried out and the three factors were

determined for the  $\omega$  and  $2\omega$  signals. Their expressions as a function of  $c_1$  were obtained as:  $c_2 = 364c_1$  and  $c_3 = 303c_1$ .

### 3.1.3 Experimental Determinations of the 16 Elements

With different combinations of optical devices, we can determine all the 16 elements in the Mueller matrix of the scatterers from the DC, the first harmonic and the second harmonic components of the signal  $I_s$  from the PMT. Table 3-2 below lists these combinations.  $\gamma_P$ ,  $\gamma_M$ ,  $\gamma_Q$ , and  $\gamma_A$  are, respectively, the orientation angles of the Polarizer, Modulator, Quarter-Wave Plate, and Analyzer used during the measurement. A bar for  $\gamma_Q$  or  $\gamma_A$  means that the optical component(s) is (are) not used. The coefficients  $DC(\Theta)$ ,  $S(\Theta)$  and  $C(\Theta)$  correspond to the DC, the  $\sin\omega t$  and the  $\cos 2\omega t$  components of the detected signal, respectively.

Table 3-2 Eight combinations of the optical elements with different orientation angles

Combination	$\gamma_P$	$\gamma_M$	$\gamma_Q$	$\gamma_A$	DC	$S(\Theta)$	$C(\Theta)$
1	$0^\circ$	$45^\circ$	-	-	$S_{11}$	$S_{14}$	$S_{12}$
2	$0^\circ$	$45^\circ$	-	$0^\circ$	$S_{11} + S_{21}$	$S_{14} + S_{24}$	$S_{12} + S_{22}$
3	$0^\circ$	$45^\circ$	-	$45^\circ$	$S_{11} + S_{31}$	$S_{14} + S_{34}$	$S_{12} + S_{32}$
4	$0^\circ$	$45^\circ$	$0^\circ$	$45^\circ$	$S_{11} + S_{41}$	$S_{14} + S_{44}$	$S_{12} + S_{42}$
5	$45^\circ$	$0^\circ$	-	-	$S_{11}$	$-S_{14}$	$S_{13}$
6	$45^\circ$	$0^\circ$	-	$0^\circ$	$S_{11} + S_{21}$	$-(S_{14} + S_{24})$	$S_{13} + S_{23}$
7	$45^\circ$	$0^\circ$	-	$45^\circ$	$S_{11} + S_{31}$	$-(S_{14} + S_{34})$	$S_{13} + S_{33}$
8	$45^\circ$	$0^\circ$	$0^\circ$	$45^\circ$	$S_{11} + S_{41}$	$-(S_{14} + S_{44})$	$S_{13} + S_{43}$

**Combination 1:** The elements  $S_{11}$ ,  $S_{14}$  and  $S_{12}$  can be determined from the following signals:

$$\begin{aligned} S_{11} &= c_1 I_{s1}(0) \\ S_{12} &= c_2 I_{s1}(2\varpi), \\ S_{14} &= c_3 I_{s1}(\varpi) \end{aligned} \quad (3.15)$$

where  $I_{s1}(0)$  refers to the DC component of signals output from PMT,  $I_{s1}(\omega)$  and  $I_{s1}(2\omega)$  to the amplitude of the first harmonic term with  $\sin\omega t$  and the second harmonic term with  $\cos 2\omega t$  in Eq. (3.8), respectively. The subscript number (1-8) is used to separate the signals obtained from different combinations. Another issue for the matrix element determination from the measured signal is to determine the polarity of the AC signals, which was done by referring to the phase values that accompany with the signal amplitude from the lock-ins. In a single goniometer scan, the signal phase may have a turnover of about  $180^\circ$  to express a polarity change for the AC components. The normalization to determine the phase value that elicits a positive or negative sign to the signals was carried out with the measurement of sphere suspensions since the theoretical calculations are available by using the Mie theory. This determination is then applied in processing the measured data for cell samples with a comparison strategy: the same sign is given to the AC signal of cell scattering measurement when the phase value is close to what is defined as positive or negative for sphere samples.

**Combination 2:** The elements  $S_{21}$ ,  $S_{22}$  and  $S_{24}$  can be determined from the following signals by following the same procedures:

$$\begin{aligned}
S_{21} &= c_1[I_{s_2}(0) - I_{s_1}(0)] \\
S_{22} &= c_2[I_{s_2}(2\varpi) - I_{s_1}(2\varpi)] . \\
S_{24} &= c_3[I_{s_2}(\varpi) - I_{s_1}(\varpi)]
\end{aligned} \tag{3.16}$$

**Combination 3:** The elements  $S_{31}$ ,  $S_{32}$  and  $S_{34}$  can be determined from the following signals:

$$\begin{aligned}
S_{31} &= c_1[I_{s_3}(0) - I_{s_1}(0)] \\
S_{32} &= c_2[I_{s_3}(2\varpi) - I_{s_1}(2\varpi)] . \\
S_{34} &= c_3[I_{s_3}(\varpi) - I_{s_1}(\varpi)]
\end{aligned} \tag{3.17}$$

**Combination 4:** The elements  $S_{41}$ ,  $S_{42}$  and  $S_{44}$  are obtained from the following signals:

$$\begin{aligned}
S_{41} &= c_1[I_{s_4}(0) - I_{s_1}(0)] \\
S_{42} &= c_2[I_{s_4}(2\varpi) - I_{s_1}(2\varpi)] . \\
S_{44} &= c_3[I_{s_4}(\varpi) - I_{s_1}(\varpi)]
\end{aligned} \tag{3.18}$$

**Combination 5:** The element  $S_{13}$  can be determined as:

$$S_{13} = c_2 I_{s_5}(2\varpi) . \tag{3.19}$$

**Combination 6:** The element  $S_{23}$  can be determined from the following signals:

$$S_{23} = c_2[I_{s_6}(2\varpi) - I_{s_5}(2\varpi)] . \tag{3.20}$$

**Combination 7:** The element  $S_{33}$  can be determined from the following signals:

$$S_{33} = c_2[I_{s_7}(2\varpi) - I_{s_5}(2\varpi)] . \tag{3.21}$$

**Combination 8:** The element  $S_{43}$  can be determined from the following signals:

$$S_{43} = c_2[I_{s_8}(2\varpi) - I_{s_5}(2\varpi)] . \tag{3.22}$$

### 3.2 Design and Control of the Goniometer System

A goniometer system was constructed to measure the angle-resolved light scattering signals. The electronic circuitry collects the DC,  $1\omega$  and  $2\omega$  signals simultaneously with three channels. The angles of the optical axes of the optical elements are measured counterclockwise relative to the horizontal plane when looking in the direction of the light beam. Three different lasers with the wavelength 442nm (HeCd Laser, Model number: 2056R-IBM-A01, Melles Griot), 633nm (HeNe laser, Model number: 05-LHP-271-299, Melles Griot) and 850nm (Diode Laser, Model number: SDL-5412, SDL) or 862nm (Diode Laser, Model number: L850P030, ThorLabs) are used individually to generate an incident laser beam. The HeNe and HeCd lasers produce highly collimated beams. However, the beams produced by diode lasers are divergent which need be collimated before use. To achieve this goal, we employ an aspheric lens (C350TM-B, Geltech) right after the laser diode and the focused light then passes through two convex lenses with their focuses overlapped at a pinhole (100 $\mu$ m in diameter) to make the laser beam collimated. The collimated beams produced by three individual lasers are processed by a polarizer and a PEM before being scattered by an ensemble of randomly oriented samples (cells or spheres). The scattered light, after an optional analyzer and quarter wave plate, is detected by a PMT that moves along a circular track at the edge of an Al plate with a radius 300mm in the horizontal plane. The detector assembly is driven by a stepping motor and controlled by a PC. For the cell scattering measurements, the PMT is rotated from 11 $^\circ$  to 168 $^\circ$  from the direction of the incident beam.

### 3.2.1 The Sample Holder

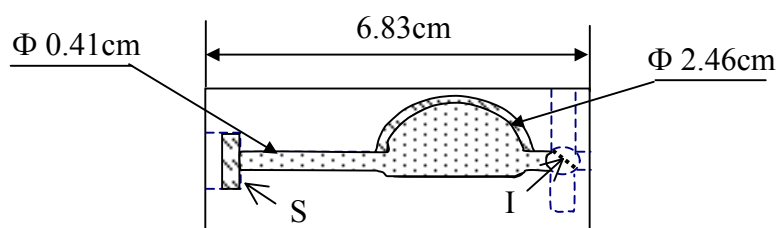


Figure 3-5 Design for the sample holder

Because of the very weak signal of scattered light at large scattering angles, it is critical to reduce the ambient light background due to the scattering of the incident light beam by the sample holder. The background reduction is especially important since we have to use low concentrations of cell suspensions to avoid multiple scattering (Volten, de Haan et al. 1998). Furthermore, the portion of the signal due to the residue background need be subtracted from the measured signals. To increase the signal-to-noise ratio, we designed a special sample holder that was depicted in Fig. 3-5. The sample holder is made of a black plastic body with a flat sapphire window S (12.7mm in diameter). A reflecting insert I of black plastic is used to direct the transmitted beam to the side channel inside the holder body, marked by the dashed line, and can be removed for aligning the incident laser beam through the holder. The plane glass window, instead of a curved glass window, is effective to reduce the beam distortion by these interfaces. The sample holder is fixed at the center of the Al plate and can be adjusted in the horizontal or vertical direction.

### 3.2.2 Scattering Volume

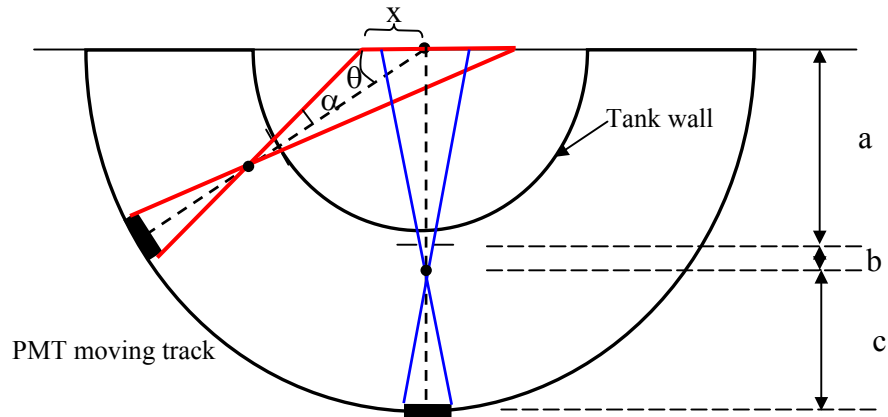


Figure 3-6 Determination of the correction factor for the scattering volume

We need to consider the variation of scattering volume  $V$  with the scattering angle in processing of the angle-resolved data (Volten, de Haan et al. 1998).  $V$ , as seen by the detector, is determined by the geometry of the incident beam profile inside the sample holder, the distance between the sample and the PMT, the diameter of the pinhole, and the dimension of the effective area of the PMT sensor. A correction factor as a function of scattering angle is derived to normalize the measured signals for the effect of varying  $V$ . Since it is a cylinder with the same base diameter (equal to the beam waist diameter) so  $V$  is proportional to the height  $x$ . In Fig. 3-6, two positions for the PMT are shown, for which one is at  $90^\circ$  and the other one is at an angle less than  $90^\circ$ . It is straightforward to obtain the following relationship:

$$\frac{x(\theta)}{\sin \alpha} = \frac{a+b}{\sin(\theta+\alpha)} \quad (3.23)$$

which yields

$$x(\theta) \approx \frac{a+b}{\sin \theta} \sin \alpha = \frac{x(90^\circ)}{\sin \theta}, \quad (3.24)$$

where  $x(\theta)$  is the height of the cylinder at scattering angle  $\theta$ . In the derivation above, we applied the approximation of  $\theta + \alpha \approx \theta$  and  $\tan \alpha \approx \sin \alpha$  since  $x \ll a + b$ . The following equations were obtained from Fig. 3-6 with the simple geometry

$$d_1/d_2 = b/c \quad \text{and} \quad 2x(90^\circ)/d_1 = (a+b)/b, \quad (3.25)$$

where  $a = 20$  cm,  $b + c = 30$  cm. The diameter for the pinhole is  $d_1 = 1.6$ mm and the width of the effective area (sensor size:  $4 \times 13$ mm) for the PMT is  $d_2 = 4.0$ mm. With all these conditions, Eq. (3.25) gives the solution for  $x(90^\circ) = 2.67$ mm that will be substituted into Eq. (3.24). Considering that  $x(\theta)$  has to be smaller than the radius of the sample holder ( $d/2$ ), we have

$$v_{corr} = \sin \theta \quad \text{for} \quad 12^\circ \leq \theta \leq 168^\circ. \quad (3.26)$$

For the case when the angle is smaller than  $12^\circ$  or bigger than  $168^\circ$ , the volume correction factor is a constant and equal to

$$v_{corr} \approx \sin 12^\circ. \quad (3.27)$$

Finally, we obtain the scattering volume correction factor as (plotted in Fig. 3-7)

$$v_{corr} = \begin{cases} \sin \theta, & 12^\circ \leq \theta \leq 168^\circ \\ \sin 12^\circ, & 10 < \theta < 12 \text{ or } 168 < \theta < 170 \end{cases} \quad (3.28)$$

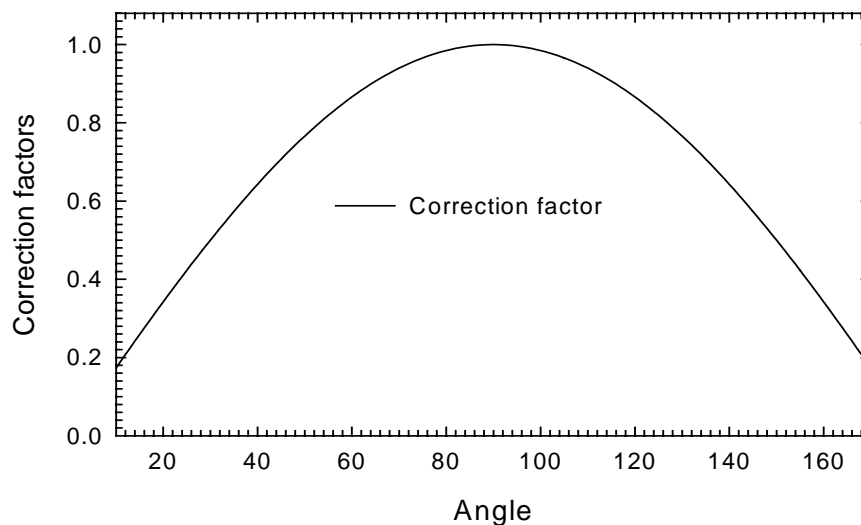


Figure3-7 Correction factor as a function of scattering angle by which the measure signal has to be multiplied to correct for the changed scattering volume as seen by the PMT.

### 3.2.3 The Scattering Angle Range

According to the discussion in the previous section, the scattered light received by the detector at the angle  $\theta$  is from multiple scatterers at different positions within the scattering volume  $V$ , which effectively makes the scattering signals from an angular range instead of a single angle. As depicted in Fig.3-8, scatterer  $n_1$  is at the center of the sample holder and  $n_2$  is an arbitrarily chosen scatterer in  $V$  seen by the detector at the angle  $\theta$ .

For the scatter  $n_2$ , the actual angle is  $\theta' = \theta + \alpha$  instead of  $\theta$ . Then we have

$$\frac{x}{\sin \alpha} = \frac{a}{\sin(\alpha + \theta)}, \quad (3.29)$$

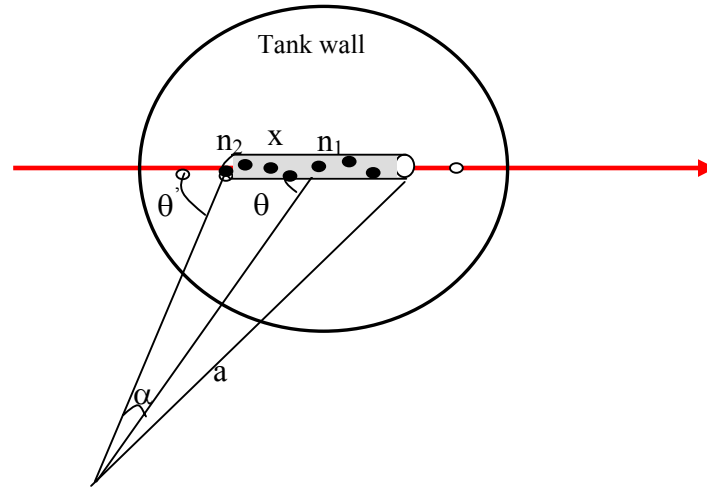


Figure 3-8 The scattering angle range

and

$$\sin \alpha = \frac{x \sin \theta}{\sqrt{x^2 + a^2 - 2ax \cos \theta}} \quad (3.30)$$

where  $a=50\text{cm}$ ,  $x = \frac{y}{\sin \theta}$  ( $12^\circ \leq \theta \leq 168^\circ$ ) or  $\frac{y}{\sin 12^\circ}$  ( $\theta < 12^\circ$  or  $168^\circ < \theta < 180^\circ$ ), and

$y=x(90^\circ)$ . Consider the case  $12^\circ \leq \theta \leq 168^\circ$ , we have

$$\sin \alpha = \frac{y}{\sqrt{\frac{y^2}{\sin^2 \theta} + a^2 - 2a \frac{y}{\sin \theta} \cos \theta}} \quad (3.31)$$

By plotting the function above, one can obtain  $\sin \alpha = 0.006$ , and this gives  $\alpha = 0.34^\circ$ .

Similarly, for  $\theta < 12^\circ$  or  $168^\circ < \theta < 180^\circ$ :

$$\sin \alpha = \frac{y}{\sqrt{\frac{y^2}{\sin^2 12^\circ} + a^2 - 2a \frac{y}{\sin 12^\circ} \cos \theta}} \quad (3.32)$$

And we have  $\alpha = 0.37^\circ$ . So the range of angle is  $\theta - 0.37^\circ \leq \theta' \leq \theta + 0.37^\circ$ .

### 3.2.4 Goniometer System Control and Alignment

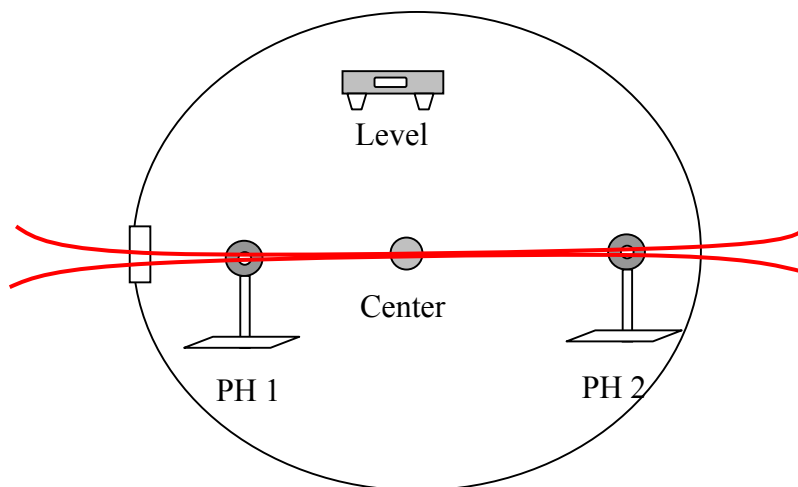


Figure 3-9 Goniometer system alignment. PH: Pin Hole

The goniometer system described in the preceding sections requires alignment before each experiment. The incident light beam is expanded and focused by a lens to obtain a long waist that should be aligned in the horizontal plane with the waist center overlapped with the center of the goniometer (Fig. 3-9). The plate of the goniometer need be leveled by adjusting its three feet. The light beam is checked to stay in the same height relative to the plate by passing it through two pin holes whose heights are kept constant. The PMT is accordingly adjusted to the same level by checking the propagating light on its window. Following that, the sample holder is mounted onto the plate and its position is carefully altered with the adjustable platform to ensure the light pass through its center. The PMT is driven from  $11^\circ$  to  $168^\circ$  through an angular mark at  $90^\circ$  on the plate to verify the angular scan precision. The AD board generates a series of TTL pulses at 1000Hz that is sent to the motor, and the number of pulses is counted by another digital channel of the AD board. A stop command is sent when the desired steps are met. However, there is a

tiny time gap between the counter accomplishment and stop command enforced, which brings the error on the movement steps. The average absolute error on the angle determined by the method above is approximately  $0.32^\circ$  at  $\theta = 90^\circ$ .

### 3.3 Reflectometry System

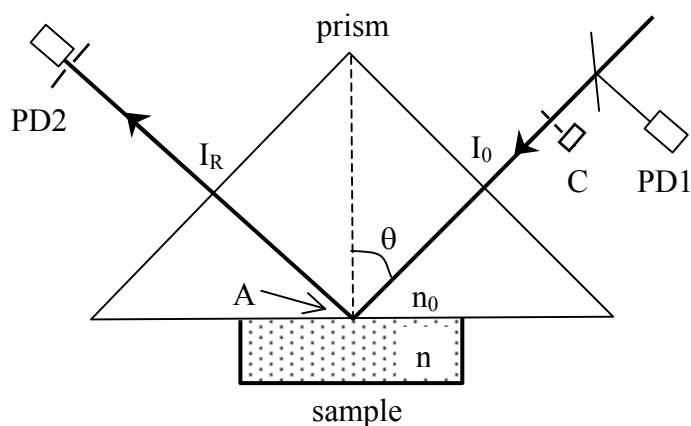


Figure 3-10 The schematic of the reflectometry system

The method of measuring critical angle of total reflection has long been used to determine refractive index of transparent liquid samples interfacing with a high-index glass prism and extended to absorbing and turbid samples by measuring the coherent reflectance curve  $R(\theta)$  (Meeten and North 1995). We adopted this approach to determine the refractive index of a tissue or intralipid sample by measuring the coherent reflectance  $R$  as a function of incident angle  $\theta$  at the interface between the sample and a glass prism. The measured  $R(\theta)$  is fitted with the calculated values of coherent reflectance from the Fresnel's equations which require the assumed value of the complex refractive index of the sample,  $n = n_r + in_i$  (Jackson 1975), and the known refractive index,  $n_0$ , of the prism.

The value of  $n$  is inversely determined using an iteration process to achieve least-squared difference between the measured and calculated  $R(\theta)$  values.

### 3.3.1 Experimental System

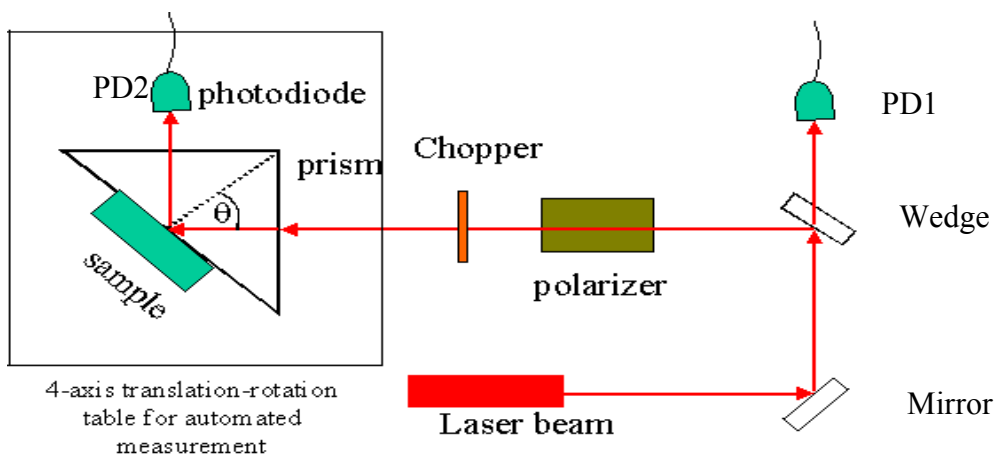


Figure 3-11 Experimental Setup for refractive index measurement

The above approach has been realized for this study with an automated system which was designed to provide 4 degrees of freedom to rotate and translate a sample and a photodiode detector for the measurement of  $R(\theta)$ . A schematic of the optical setup was shown in Fig. 3-11. A laser beam first incidents on an optical wedge that directs a fraction of the beam to a reference photodiode (see Fig. 3-13 or 3-14 at the end of this chapter). The reflected beam passes through a polarizer (PRH8010, Casix) to produce a light beam with either s (perpendicular to the plane of Fig. 3-11) or p (in the plane of Fig. 3-11) polarization. Next the beam enters a right-angle BK7 prism (30-42-30cm) (RAP0903, Casix) and is reflected off the base surface. The prism and sample holder are mounted on a 2-axis rotation-translation stage so that the angle of incidence  $\theta$  can be

varied while the laser beam is kept at the center of the prism base surface. After exiting the prism, the specularly reflected light is detected with another photodiode (Fig. 3-13 or 3-14) mounted on another 2-axis rotation-translation stage. A Visual Basic program was developed to control the four stepping motors for the prism and the second photodiode and collect the data from a lock-in amplifier at the chopping frequency of 370Hz.

The incident laser beam is collimated for the experiment by two apertures before entering the prism. Neutral-density filters are placed before the polarizer to reduce the incident power to about 0.5-4  $\mu\text{W}$  (measured in front of the prism) and ensure photodiodes' linear response to the reflected light signals. The experimental procedures are as the following: the specular reflectance  $R$  is determined from the measured specularly reflected light signal in a range of incident angle  $\theta$  from  $46^\circ$  to  $80^\circ$ . The  $R(\theta)$  curves are fitted to the calculated values from the Fresnel's equations to determine the complex index of the sample which are used as the fitting parameters. In determining the measured values of reflectance, we take into account the absorption of light when propagating in the BK7 glass prism and reflection loss at the entrance and exit surfaces of the prism.

### **3.3.2 The Prism Motion Control**

The prism and the photodiode detector are rotated and translated relative to a fixed incident laser beam for the measurement of the coherent reflectance curve  $R(\theta)$ . The angle at which light enters the prism need be changed to obtain the reflectance curve

at the sample-prism interface. To adjust the incident angle  $\theta$  to another value larger than  $45^\circ$ , the prism is rotated through an angle  $\phi$  around its base center satisfying

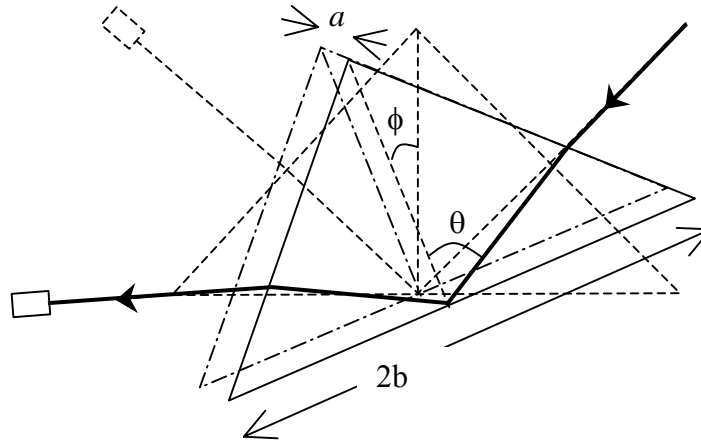


Figure 3-12 Varied positions of the prism

$$\sin \phi = n_0 \sin(\theta - 45^\circ) \quad (3.33)$$

and then translates over a distance  $a$  given by

$$a = b \left\{ \frac{\sin(90^\circ - \theta)}{\sin[45^\circ + \theta]} - \frac{\sin(45^\circ - \phi)}{\sin(90^\circ + \phi)} \right\} \quad (3.34)$$

where  $2b = 42.43\text{mm}$  is the length of the prism base, as shown in Fig. 3-12.

### 3.4 Sample Acquisition and Preparation

The optical properties of cellular samples and turbid media were experimentally investigated in this dissertation: Human B-cells, HL-60 cells, human and porcine skin tissues. The aqueous suspensions of polystyrene microspheres were used to calibrate our goniometer system. The preparation techniques are described below.

### **3.4.1 Polystyrene Microsphere Suspensions Preparation**

Polystyrene microspheres with 1.0  $\mu\text{m}$  in diameter (coefficient of variance: 3%) were purchased as a suspension in deionized water with a nominal concentration of 10% by weight (5100B, Duke Scientific Corporation). The suspension concentration is a critical factor in the determination of the scattering signal strength by the scatterers. To avoid the multiple scattering, the concentration cannot be too large, however, if the concentration is too small, the signal will be relatively weak and make the signal to noise ratio be unfavorably small. By diluting with deionized water, we prepared the microsphere suspensions with nominal number densities of  $4.8 \times 10^2$  microspheres/ $\mu\text{l}$ , based on the nominal concentration of the original suspension from the manufacturer. If aggregated spheres were observed, a small drop of dispersing agent (TWEEN 20, USB) was added to the suspension to reduce aggregation.

### **3.4.2 Cell Sample Preparation**

B cell suspensions were prepared for goniometer measurements from cultured NALM-6 cells. The NALM-6 cell line is derived from human B-cells extracted from the peripheral blood of a patient with acute lymphoblastic leukaemia (Hurwitz, Hozier et al. 1979). The NALM-6 cells were cultured in a standard media containing the following: 75 mls of AmnioMax Basal (Invitrogen Corp., Carlsbad, California), 12.5 mls of AmnioMax Supplement (Invitrogen Corp., Carlsbad, California), 87.5 mls of Minimal Essential Media (Invitrogen Corp., Carlsbad, California), 20 mls of Fetal Bovine Serum (Invitrogen Corp., Carlsbad, California), 2 mls of L- Glutamine (Invitrogen Corp.,

Carlsbad, California), and 2 mls of Penicillin/ Streptomycin (Invitrogen Corp., Carlsbad, California). Fresh culture media was added to the NALM-6 cells 6 days before they were used in each goniometer measurement to ensure that the majority of the cells were in resting (G0) phase due to lack of nutrients, as opposed to the addition of fresh media every 3-4 days when the NALM-6 cells were maintained in log phase when not being prepared for measurements.

The experimental concentration of B-cell suspension was diluted from the original NALM-6 cell culture by 9:1 with fresh media to a concentration of about  $2.34 \times 10^2$  cells/ $\mu$ L after a signal linearity check on the concentration to satisfy the single-scattering condition. The same preparation procedures were followed for the HL-60 cells.

### **3.4.3 Skin Sample Preparation**

Large patches of full-thickness porcine skin were removed from the back of the neck of 6-month-old domestic pigs at the Department of Comparative Medicine, Brody School of Medicine, East Carolina University after the animals were sacrificed for medical classes. Fresh human skin tissue patches were obtained from the patients undergoing abdominoplasty procedures at the plastic surgery clinic of the Brody School of Medicine, East Carolina University. A study protocol approved by the IRB of School of Medicine, East Carolina University was strictly followed and a consent form was signed by each participating patient before the surgery.

Each skin patch was stored in a bucket of crushed ice ( $\sim 2^\circ\text{C}$ ) inside a refrigerator immediately after surgery. Samples with sizes of about  $1\text{cm} \times 1\text{cm}$  were prepared by

removing the hair on the skin surface with scissors and subcutaneous fat tissue with a razor blade and warming the skin to a room temperature of about 22°C with 0.9% saline drops. Care was taken to preserve the stratum corneum layer of the skin epidermis.

The following method was employed to obtain the skin samples (Ma et al, 2005). To obtain the dermis samples, a 1 cm square of porcine skin tissue was glued (super glue or cyanoacrylate) on a specially designed microtome on its epidermis side at room temperature. A small razor blade was used to section the dermis samples and the thickness ranged from 0.3mm to 1.2 mm. It typically took about 8 minutes to finish the whole procession. For the epidermis samples, we removed the hair on skin surface and most of the fat layer of the skin. In our measurement of the coherent reflectance curve, care has been taken to firmly press the skin tissue sample with either epidermis or dermis side against the prism. To obtain the reflection on the interface between the prism and the skin sample, the thickness of the sample is not a critical issue, and we chose the thin slice for the purpose to seal it behind the prism easily.

During the reflectance measurement for the skin samples, a constant pressure about  $2.06 \times 10^5$  Pa from a nitrogen tank was applied to push the soft rubber and delivery a same force to the whole measurement area on the sample. The pressure dependence of the refractive index is depicted in the latter chapter. The whole procession time for each sample is about 2-3 hours (6 measurements in total and 3 per polarization), To decrease the effect of dehydration, the transparent plastic tap was used to completely seal the

sample to the side of the prism, and no critical structure difference was found for the sample before mounting and after the measurement was completed.

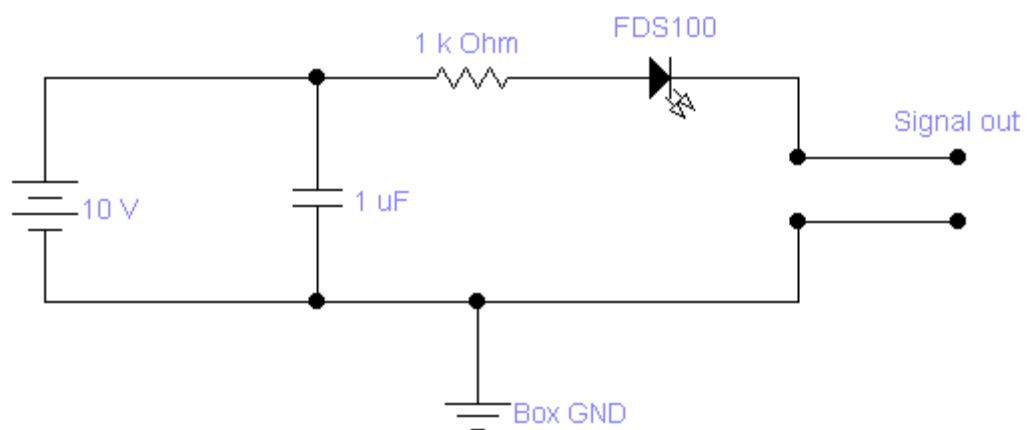


Figure 3-13 Schematic diagram for the Si photodiode

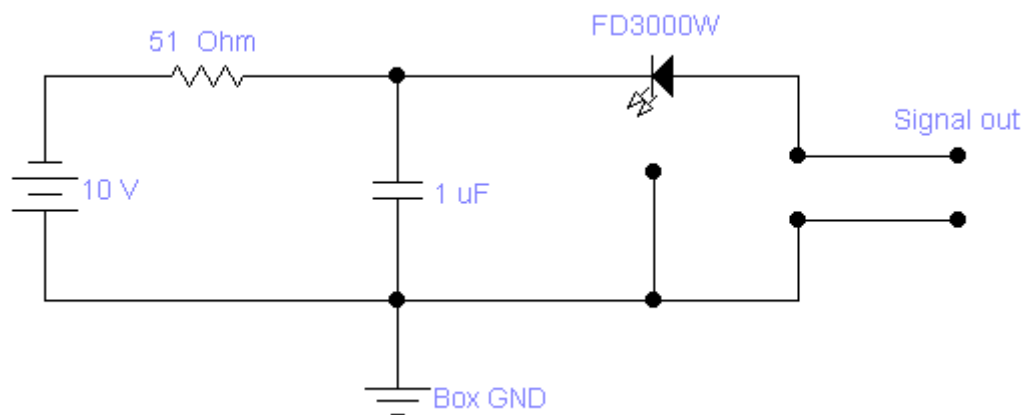


Figure 3-14 Schematic diagram for the GaAs photodiode

## Chapter 4 Cell Scattering Measurement

In this Chapter, we present the Mueller matrix elements of cell suspension samples determined from the goniometer measurements using a photoelastic modulation scheme. This system was calibrated at three different wavelengths (442, 633, 850nm or 862nm) by comparing the measured elements of the microsphere suspension to the calculated elements using the Mie theory. Experimental results of the 16 Mueller matrix elements are shown for both human B-cells and HL-60 cells.

### 4.1 Goniometer System Calibration

The goniometer system was first calibrated with the suspension samples of polystyrene microsphere of 1 $\mu$ m in diameter (5100B, Duke Scientific Corporation). To ensure single-scattering approximation, the sphere concentration was reduced by a factor of about 50,000 from the purchased aqueous solution of 10% by weight (2.4 $\times 10^7$  spheres/ $\mu$ l) to 4.8 $\times 10^2$  spheres/ $\mu$ L. At this concentration level, the  $S_{11}$  signal was found to change linearly with the concentration. The DC, fundamental and 2<sup>nd</sup> harmonic components were acquired to determine  $S_{11}$ ,  $S_{12}$  and  $S_{34}$  (see section 3.1.1 and Eq. 3.8). The data processing consists of four steps: (1) subtraction of background signals measured with deionized water in the sample holder; (2) removal of the effect of different sample volume “seen” by the detector at different angular positions with a volume scaling factor; (3) determination of the element  $S_{11}$  within an adjustable constant from the DC signal and other elements from the DC or harmonic signals by combining the

measured amplitude and phase angle of the lock-in signals; (4) normalization of the processed signals by dividing other DC and harmonic signals by the DC signal measured in the first combination to determine the matrix elements normalized to  $S_{11}$ . For the second step of data processing, a volume-scaling factor was numerically calculated from the system geometry and the angular range of the apertured detector tube,  $6.46 \times 10^{-3}$  rad or about  $0.37^\circ$ , as a function of  $\theta_s$  and was shown in Fig. 4-1.

The reduction of the background noise is critical in our design improvement of the goniometer system to ensure scattering measurement with sufficient signal-to-noise ratios, especially at the backward scattering direction where the background noise is unfavorably large. We employed four particular procedures to achieve this goal. First, the base and the half circle (0 to  $-180^\circ$  in scattering angle) of the water immersion tank wall were all painted black to decrease reflection; Second, the suspension sample was carefully added to the sample holder with a 10ml syringe and another 50ml syringe was penetrated into the tunnel of the sample holder to completely remove the air bulbs; Third, the collimated portion of the transmitted beam was directed to the side at the end of the inside tunnel of the sample holder to avoid being scattered by the tank-water and other interfaces and picked up as signals. Fourth, a long copper tube (inside diameter: 7.5mm, length: 300mm, see Fig. 3-6) with a pinhole (1.6mm in diameter) at one end, which was painted black both inside and outside, was placed in front of the PMT to reject scattered light from outside of the sample region of measurement. Fig. 4-2 showed a typical result of the signal to noise ratios in our measurement for sphere suspension.

The calibration measurements were carried out with the same sphere suspensions at each of the three wavelengths of 442, 633 and 850nm (or 862nm) and repeated before each measurement of cell suspensions as a part of system alignment and calibration. The beam sizes for these three wavelengths were measured with the knife-edge method and determined as 0.47mm, 0.26mm, and 0.95mm, respectively. Typical results of Mueller matrix elements  $S_{11}$ ,  $s_{12}$  and  $s_{34}$  were shown in Figs. 4-3 to 4-5 at the three wavelengths. The measured element  $S_{11}$  was plotted with an adjustable parameter, corresponding to the constant  $c_1$  in Eq. (3.8), to fit to the calculated curve based on the Mie theory with refractive indices of water as  $n_h$  and polystyrene sphere as  $n_{sp}$  (see the caption of the figures). The angular distributions of other normalized matrix elements,  $s_{ij}$ , were obtained by the ratios of measured elements to the measured  $S_{11}$  without any adjustable parameter. From the sphere results, one can see that  $S_{11}$  agrees well with the calculated values while other elements agree to lesser degrees. Specifically, the characteristic oscillations in the angle-resolved elements match consistently with the calculated values from a single sphere but the oscillation amplitudes are reduced. We attribute the difference between the amplitudes of oscillation to the angle-averaging effect by the multiple spheres contributing to the detected signals and possible residue sphere aggregation in the suspension causing breakdown in single-scattering approximation. The same calibration procession was repeated on the day when cell samples were used for measurement.

## 4.2 Matrix Elements of the B-cells

Among the diverse arrays of biological cells, human blood cells attract active research interests because of their important roles in the metabolism and immune systems of the human body. B-cells are one of two major types of lymphocytes of the white blood cells (Parker 1993). Compared to other human cells, normal B-cells are relatively small with near-spherical shapes for their cytoplasm membranes and relatively simple intracellular structures containing one large nucleus, except in the dividing stage, and few cytoplasmic organelles (Brock, Hu et al. 2006). We chose the human B-cells as the subject for our angle-resolved Mueller matrix study of light scattering to extend the previous efforts with either only experimental measurements (Bickel, Davidson et al. 1976; Bickel and Stafford 1981; Volten, de Haan et al. 1998) or modeling based on the Mie theory (Mourant, Canpolat et al. 2000; Zharinov, Tarasov et al. 2006).

Suspension samples of B-cells were prepared from the NALM-6 cell culture (Hurwitz, Hozier et al. 1979) by a 9:1 dilution with fresh media to a concentration of about  $2.34 \times 10^2$  cells/ $\mu\text{L}$  which was set by a similar signal linearity check to ensure the single-scattering approximation. With the signal acquisition procedures similar to those described in the previous section, the Mueller matrix elements  $S_{11}$  and other fifteen elements that were normalized by  $S_{11}$  were determined as a function of scattering angle  $\theta_s$  at each of the three wavelengths of 442, 633 and 862nm. Determinations of these elements for each suspension sample required eight goniometer scans in two groups (four scans/group) with a different analyzer or quarter wave plate configuration and took about

30 minutes to complete four scans (one group). Each sample was replaced after four scans with fresh ones that were kept in an incubator at 37°C during the day of measurements. All measurements were performed at a room temperature of about 22°C. At each wavelength, the measurements were repeated on two different cell samples to obtain four sets of angle-resolved Mueller matrix elements (each sample contributes two sets of measurements). The measured results were plotted in Figs. 4-6~4-13 with symbols and error bars representing the mean and standard deviation of the four data sets, respectively. The elements  $S_{11}$  contained an adjustable parameter that was determined from the microsphere calibration results performed at each wavelength before the cell scattering measurements.

As it was discussed in Chapter 2, at most seven of the sixteen elements in the Mueller matrix are independent under the assumption that the scatterer remains at the same orientation without structure change during the measurement period. This is not our case because the suspended cells have varied morphology and can rotate randomly. During the measurement, the structures of cells are subjected to change beside their unstable orientations. The Mueller matrix of a cell suspension sample is the addition of individual Mueller matrices for each cell contributing to the measured signals (~100 to 300) under the single scattering approximation. Therefore, the sixteen elements of the Mueller matrix for a suspension cell sample are in general independent of each other. This motivates us to determine all of the sixteen elements instead of seven.

### 4.3 Matrix Elements of HL-60 Cells

HL-60 cells are used as an in vitro model of acute promyelocytic leukaemia and are attractive for studies of human myeloid cell differentiation and apoptosis (Birnie 1988). They are able to grow in suspension culture without added conditioned media. HL-60 cells have been proven to be a convenient source of various mRNAs and proteins (such as tumor necrosis factor) (Wang, Creasey et al. 1985) found in hematopoietic cells (Dalton, Ahearn et al. 1988; Kang, Lee et al. 2001).

With their relatively complicated structure compared to that of B-cells, HL-60 cells were chosen to increase the complexity of our measurement and provided comparison of matrix elements between different cell samples. The suspension sample of HL-60 cells were prepared from the high concentrated cell culture by a 9:1 dilution with RPMI-1640 medium to a concentration of about  $2.34 \times 10^2$  cells/ $\mu\text{L}$  which was same as we used for B- cell measurements. Same procedures as in the previous section were strictly followed to complete the experimental data acquisition at each of the three wavelengths of 442, 633 and 850nm. Angle-resolved Mueller matrix elements were plotted in Figs. 4-14~4-21 with symbols and error bars representing the mean and standard deviation of the four data sets, respectively.

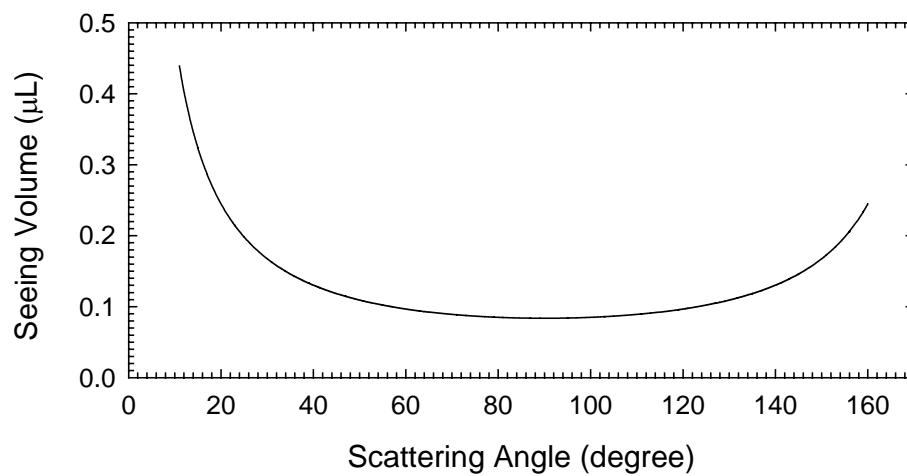


Figure 4-1 The calculated sample volume “seen” by the detector versus the scattering angle  $\theta_s$ .

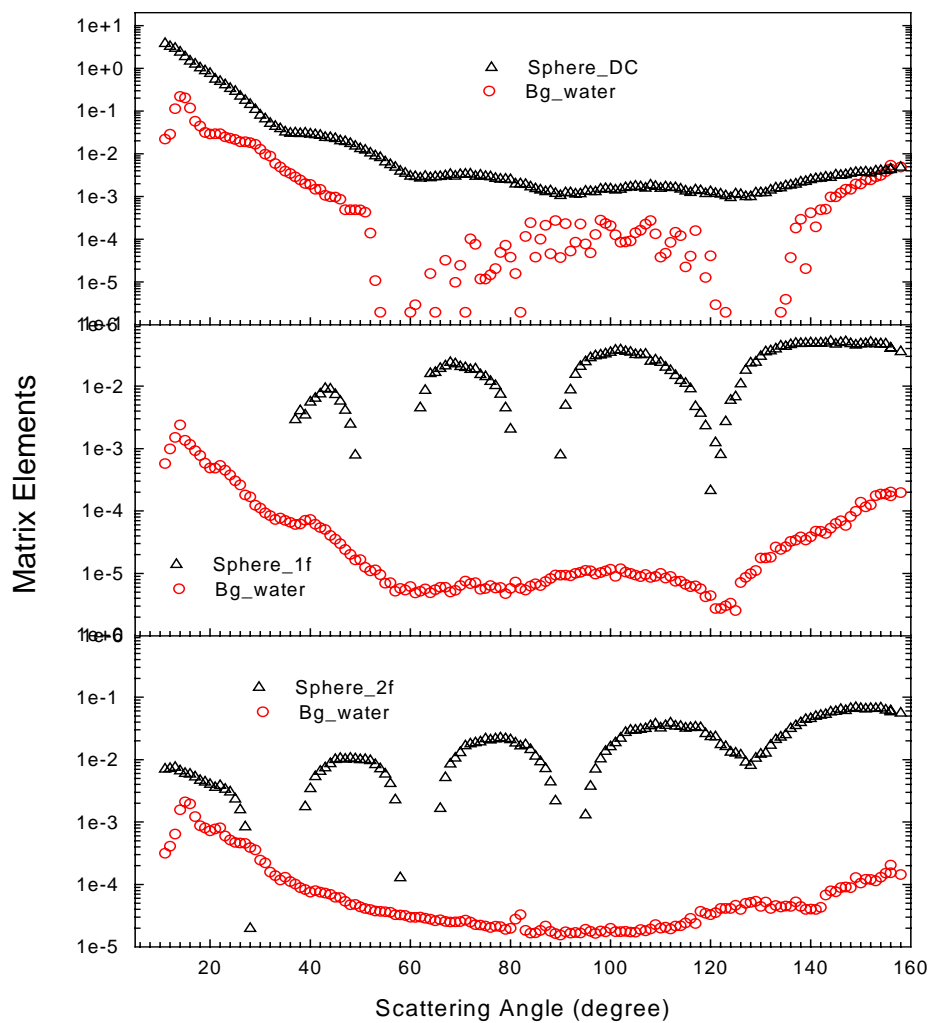


Figure 4-2 Comparison between the signal (triangle) and the background noise (circle) for sphere suspension at 633nm.

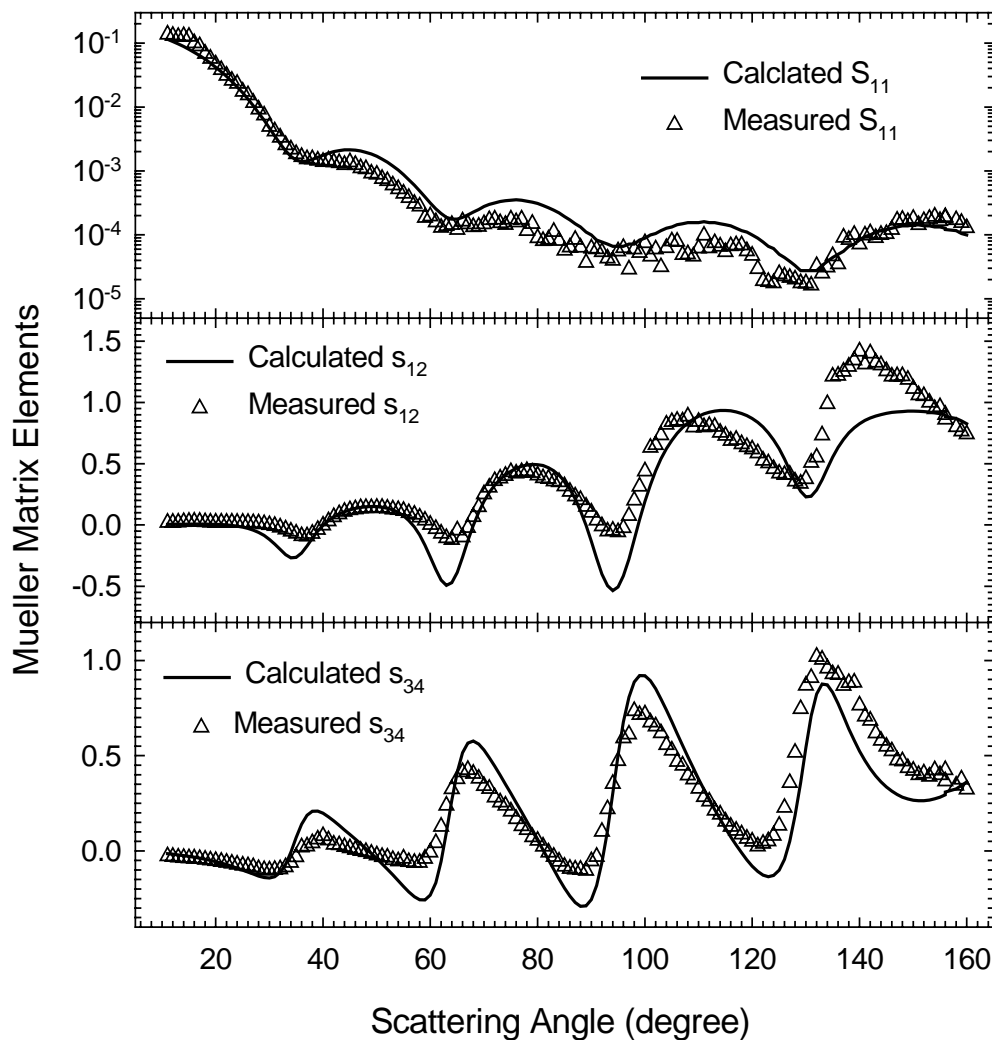


Figure 4-3 The measured and calculated Mueller matrix elements  $S_{11}$ ,  $s_{12}=S_{12}/S_{11}$  and  $s_{34}=S_{34}/S_{11}$  versus the scattering angle  $\theta_s$  for water suspension of polystyrene microsphere with diameter of  $1.00\mu\text{m}$  at  $633\text{nm}$ . The solid lines were obtained from the Mie theory with  $n_h=1.332$  and  $n_{sp}=1.582$  for a single sphere and the measured  $S_{11}$  was fitted to the calculated results with one adjustable constant. The normalized elements were plotted with no fitting.

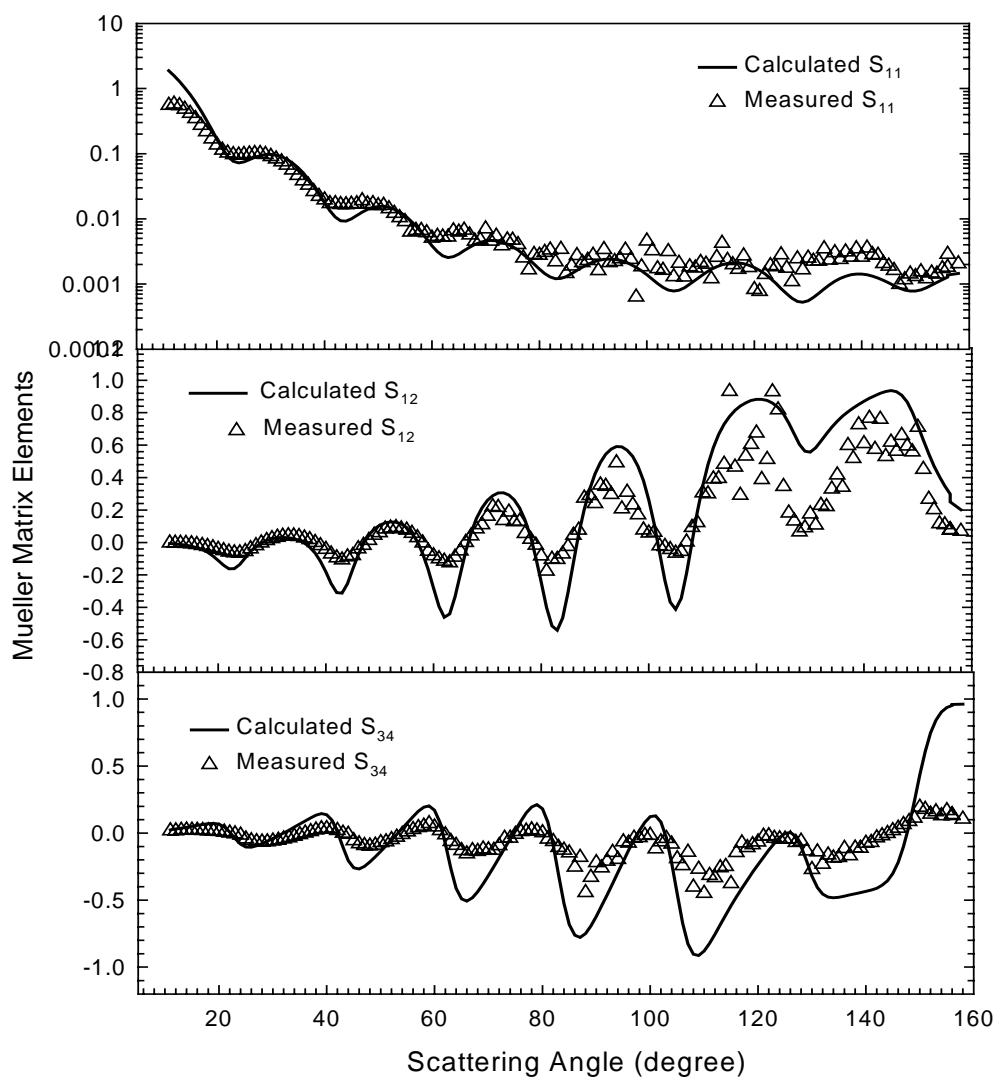


Figure 4-4 The measured and calculated Mueller matrix elements  $S_{11}$ ,  $s_{12}=S_{12}/S_{11}$  and  $s_{34}=S_{34}/S_{11}$  versus the scattering angle  $\theta_s$  for water suspension of polystyrene microsphere with diameter of  $1.00\mu\text{m}$  at  $442\text{nm}$ . The solid lines were obtained from the Mie theory with  $n_h=1.3380$  and  $n_{sp}=1.601$ .

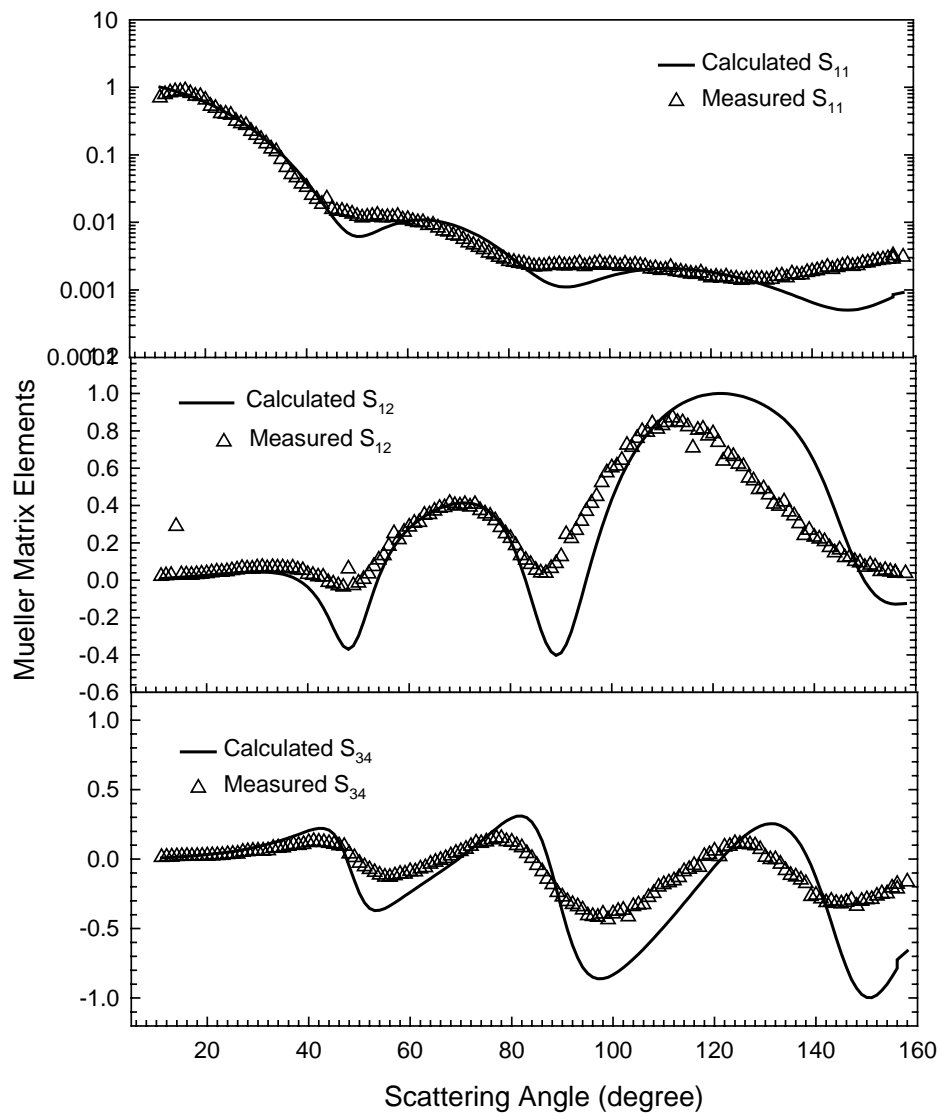


Figure 4-5 The measured and calculated Mueller matrix elements  $S_{11}$ ,  $s_{12}=S_{12}/S_{11}$  and  $s_{34}=S_{34}/S_{11}$  versus the scattering angle  $\theta_s$  for water suspension of polystyrene microsphere with diameter of  $1.00\mu\text{m}$  at  $850\text{nm}$ . The solid lines were obtained from the Mie theory with  $n_h=1.3290$  and  $n_{sn}=1.575$ .

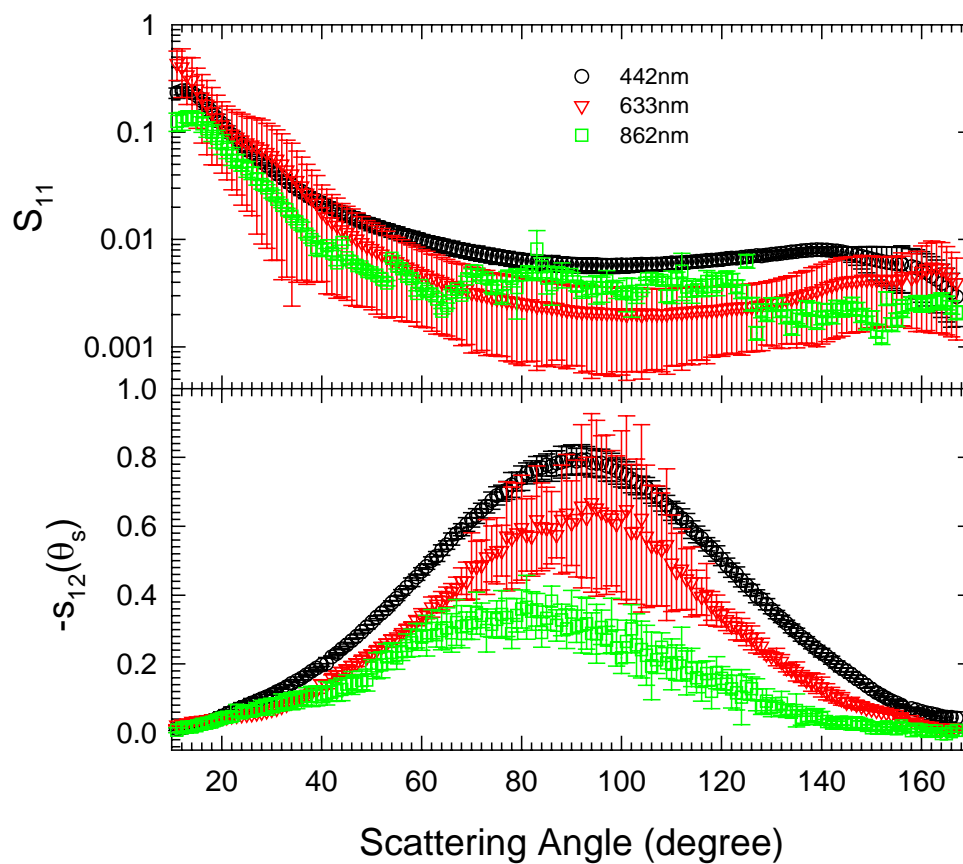


Figure 4-6 The angle-resolved Mueller matrix elements  $S_{11}$  and  $-s_{12}(\theta_s)$  of B-cell suspension samples at the wavelengths of 442, 633 and 862nm. The data points and error bars represent the mean and standard deviation of four measurements with different cell samples at different days.

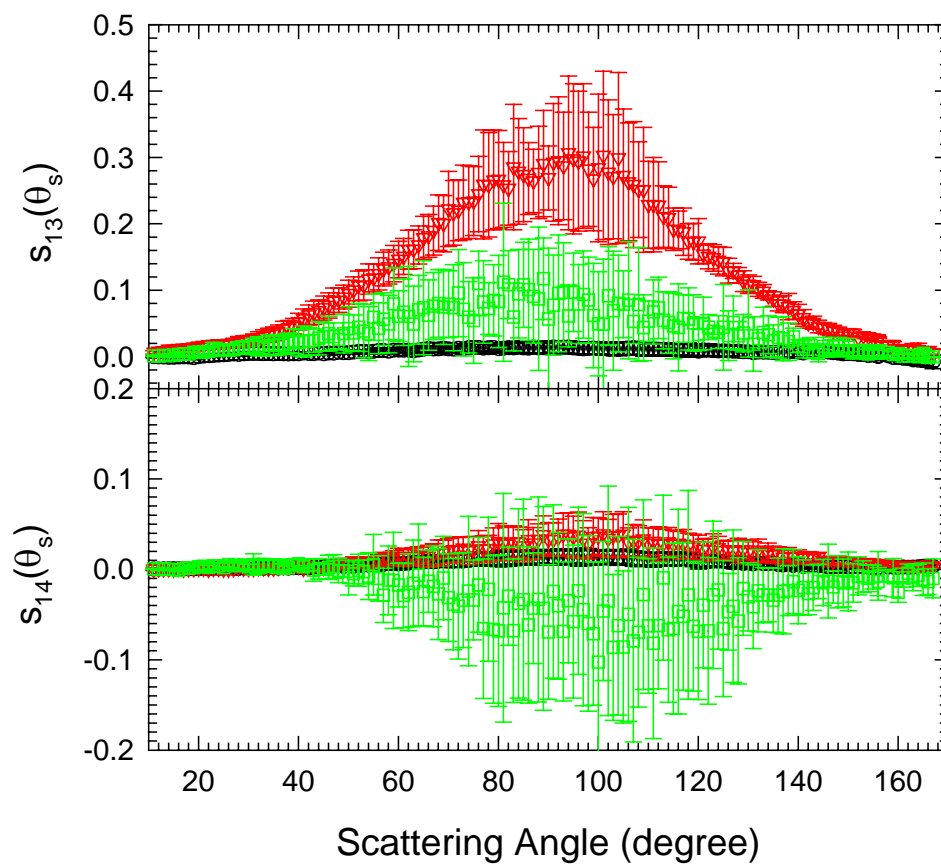


Figure 4-7 Same as Figure 4-6 for the angle-resolved Mueller matrix elements  $s_{13}(\theta_s)$  and  $s_{14}(\theta_s)$  of B-cell suspension samples at the wavelength of 442, 633 and 862nm.

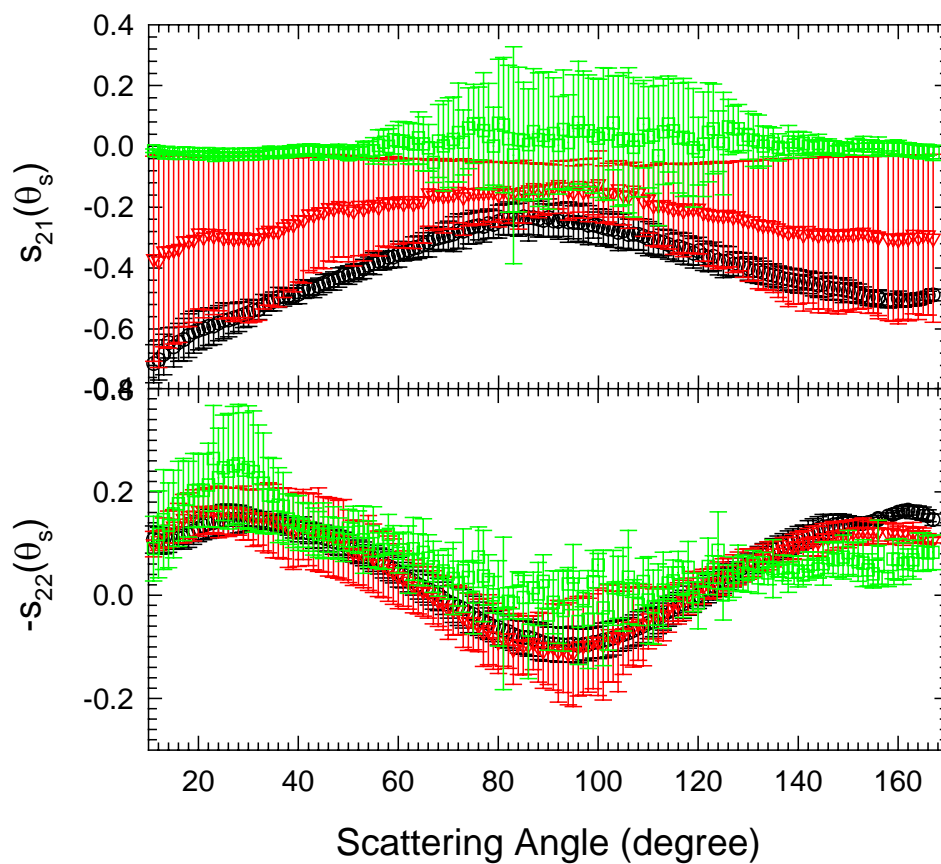


Figure 4-8 Same as Figure 4-6 for the angle-resolved Mueller matrix elements  $s_{21}(\theta_s)$  and  $-s_{22}(\theta_s)$  of B-cell suspension samples at the wavelengths of 442, 633 and 862nm.

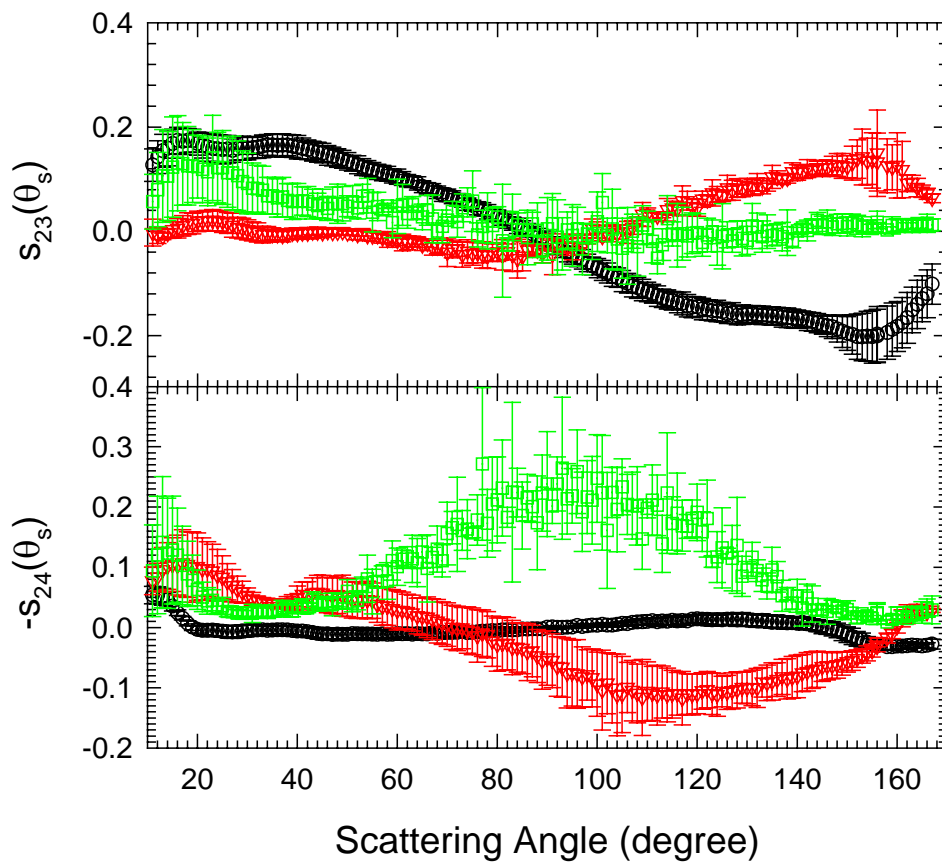


Figure 4-9 Same as Figure 4-6 for the angle-resolved Mueller matrix elements  $s_{23}(\theta_s)$  and  $-s_{24}(\theta_s)$  of B-cell suspension samples at the wavelengths of 442, 633 and 862nm.

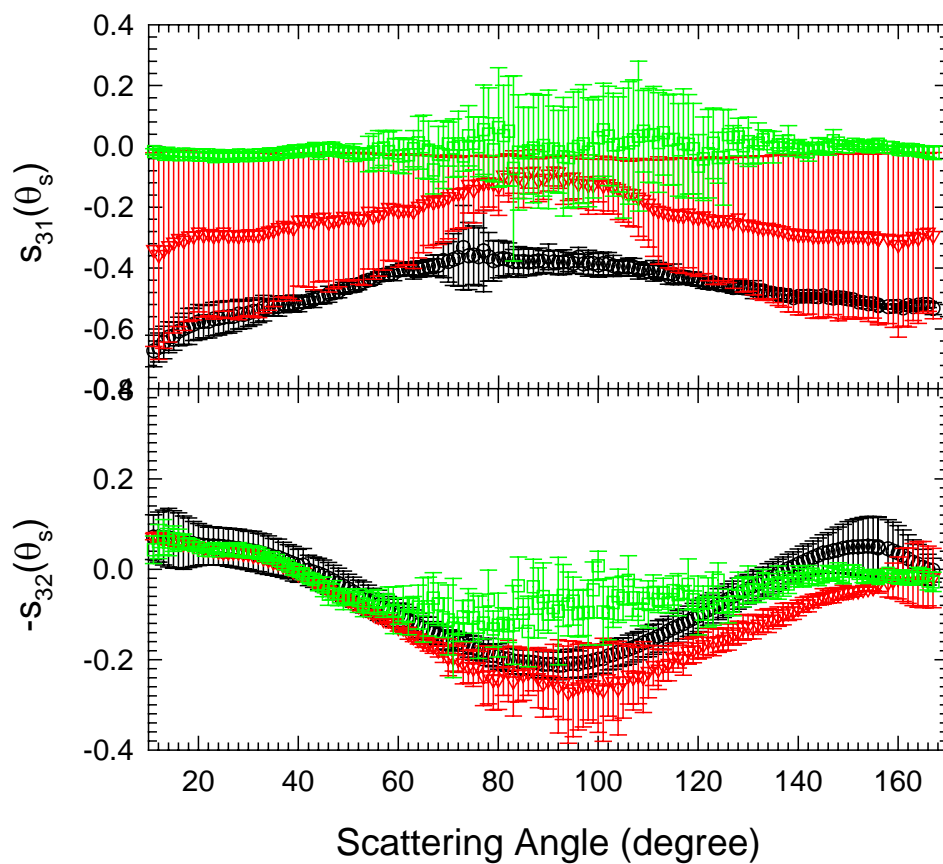


Figure 4-10 Same as Figure 4-6 for the angle-resolved Mueller matrix elements  $s_{31}(\theta_s)$  and  $-s_{32}(\theta_s)$  of B-cell suspension samples at the wavelengths of 442, 633 and 862nm.

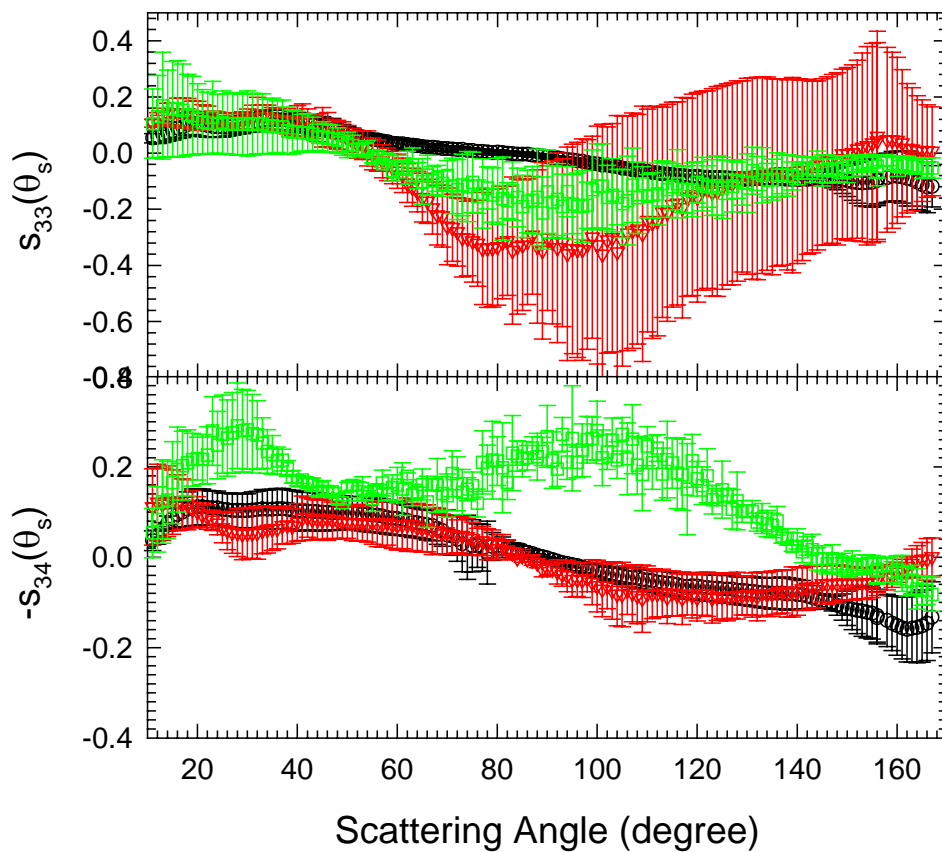


Figure 4-11 Same as Figure 4-6 for the angle-resolved Mueller matrix elements  $s_{33}(\theta_s)$  and  $-s_{34}(\theta_s)$  of B-cell suspension samples at the wavelengths of 442, 633 and 862nm.

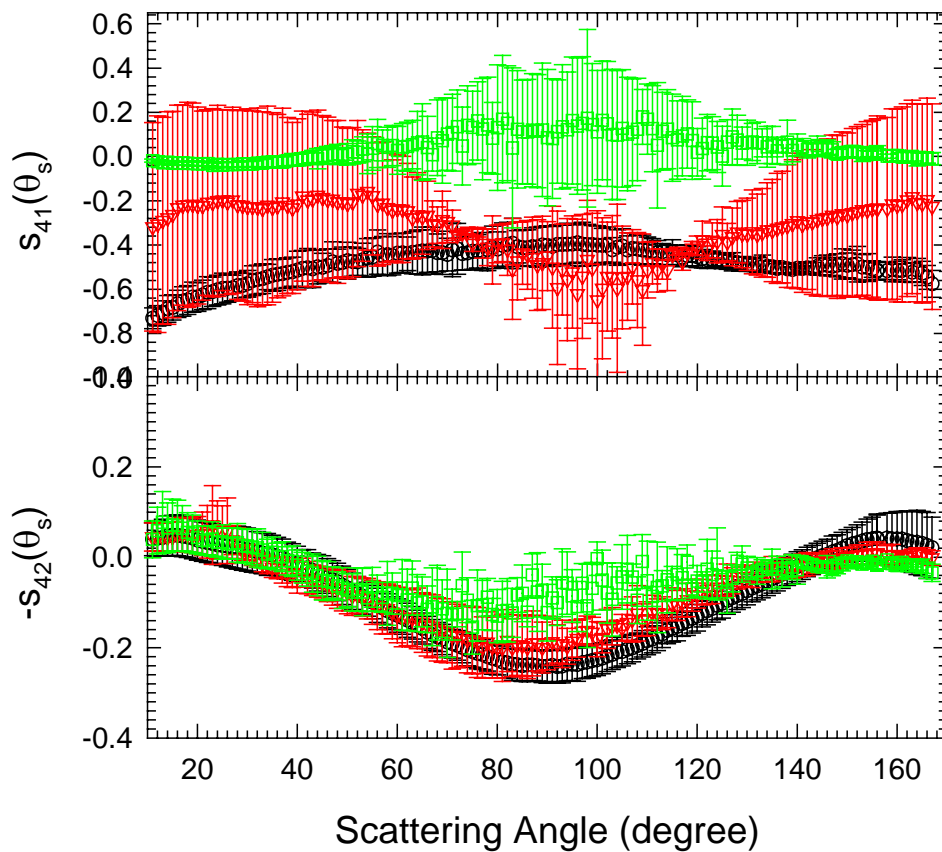


Figure 4-12 Same as Figure 4-6 for the angle-resolved Mueller matrix elements  $s_{41}(\theta_s)$  and  $-s_{42}(\theta_s)$  of B-cell suspension samples at the wavelengths of 442, 633 and 862nm.

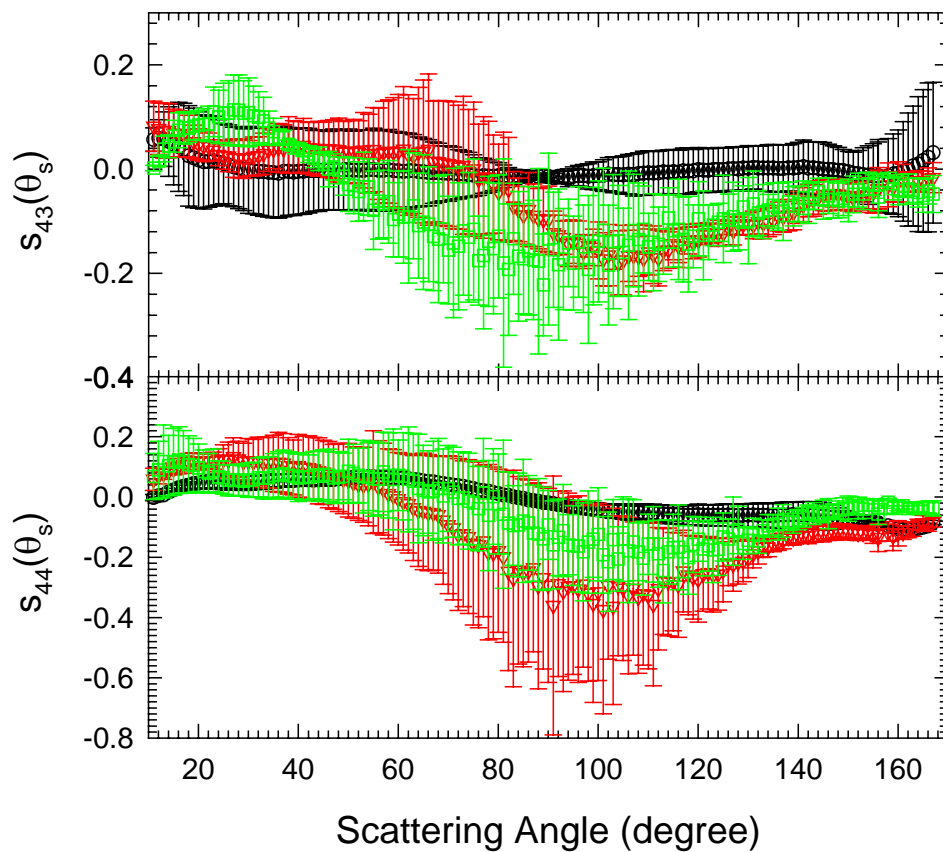


Figure 4-13 Same as Figure 4-6 for the angle-resolved Mueller matrix elements  $s_{43}(\theta_s)$  and  $s_{44}(\theta_s)$  of B-cell suspension samples at the wavelengths of 442, 633 and 862nm.

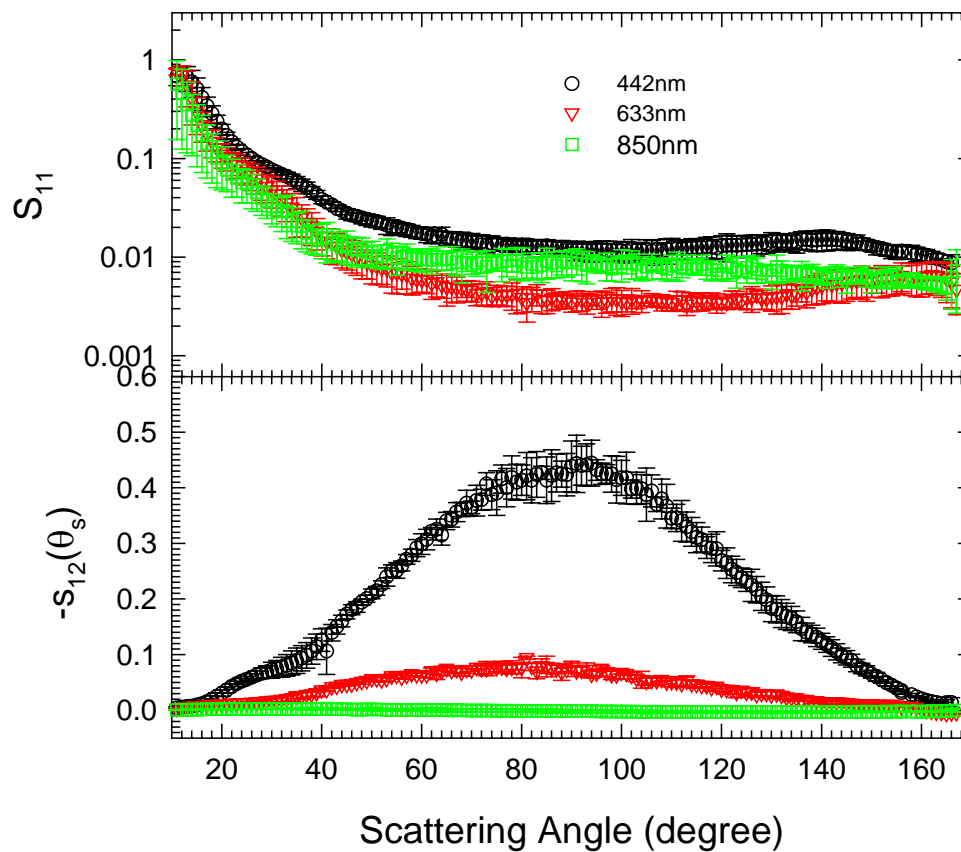


Figure 4-14 The angle-resolved Mueller matrix elements  $S_{11}$  and  $-s_{12}(\theta_s)$  of HL-60 cell suspension samples at the wavelengths of 442, 633 and 850nm. The data points and error bars represent the mean and standard deviation of three measurements with different cell samples at different days.

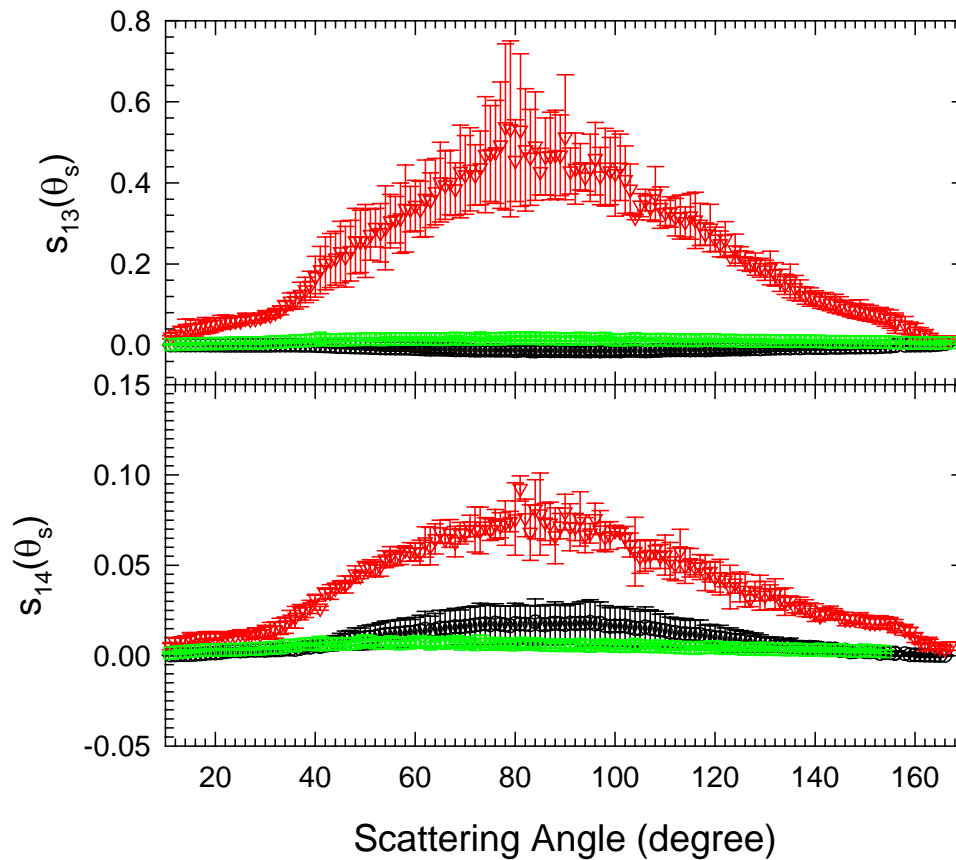


Figure 4-15 Same as Figure 4-14 for the angle-resolved Mueller matrix elements  $s_{13}(\theta_s)$  and  $s_{14}(\theta_s)$  of HL-60 cell suspension samples at the wavelengths of 442, 633 and 850nm.

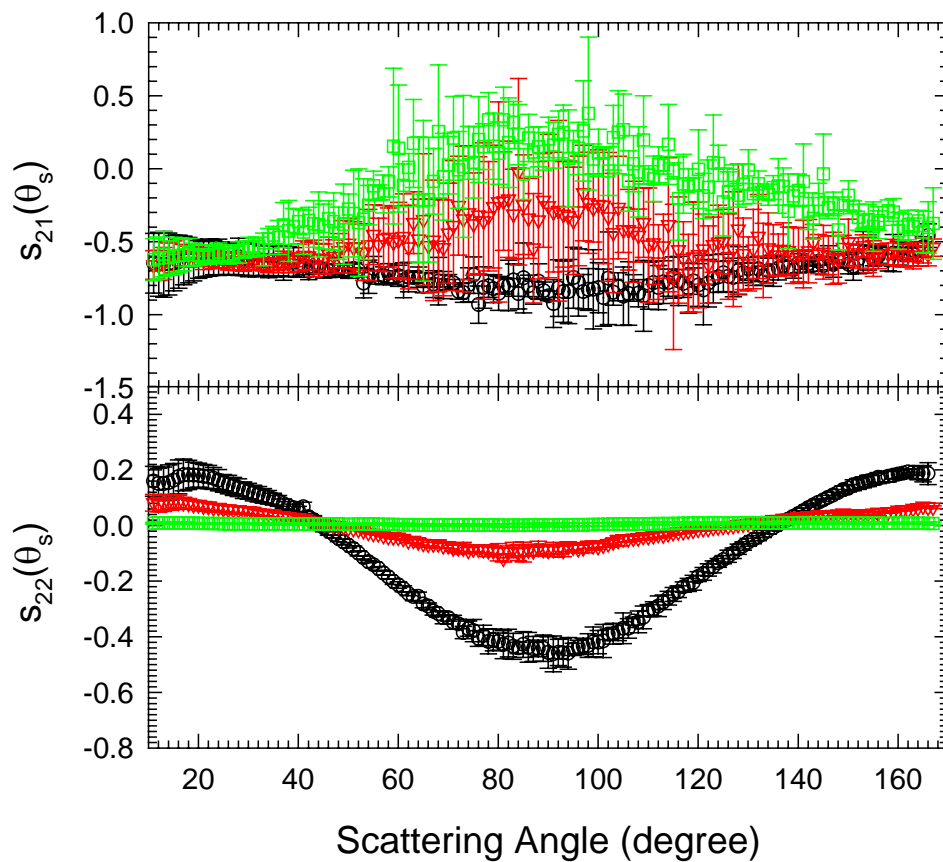


Figure 4-16 Same as Figure 4-14 for the angle-resolved Mueller matrix elements  $s_{21}(\theta_s)$  and  $s_{22}(\theta_s)$  of HL-60 cell suspension samples at the wavelengths of 442, 633 and 850nm.

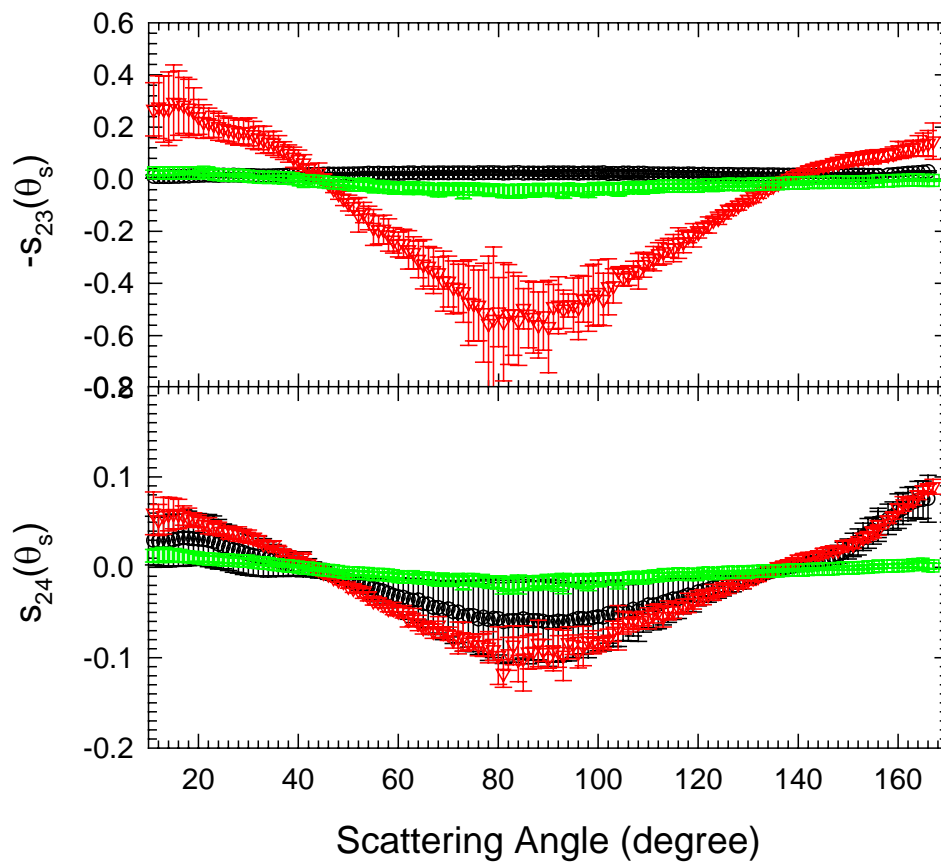


Figure 4-17 Same as Figure 4-14 for the angle-resolved Mueller matrix elements  $-s_{23}(\theta_s)$  and  $s_{24}(\theta_s)$  of HL-60 cell suspension samples at the wavelengths of 442, 633 and 850nm.

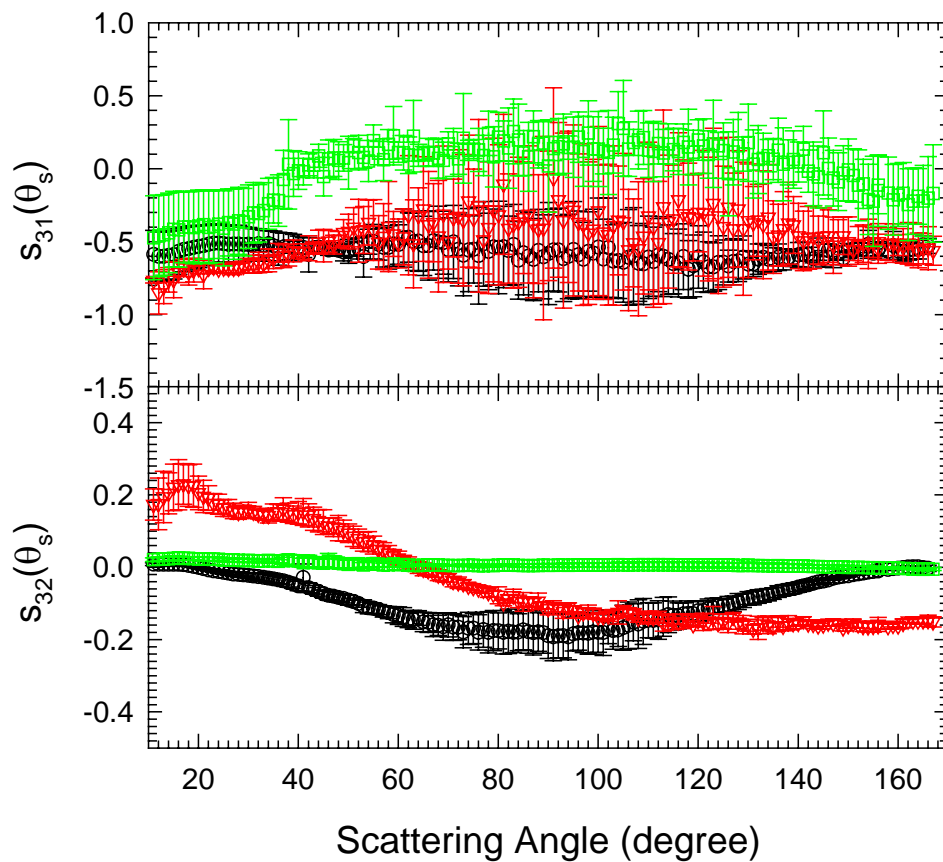


Figure 4-18 Same as Figure 4-14 for the angle-resolved Mueller matrix elements  $s_{31}(\theta_s)$  and  $s_{32}(\theta_s)$  of HL-60 cell suspension samples at the wavelengths of 442, 633 and 850nm.

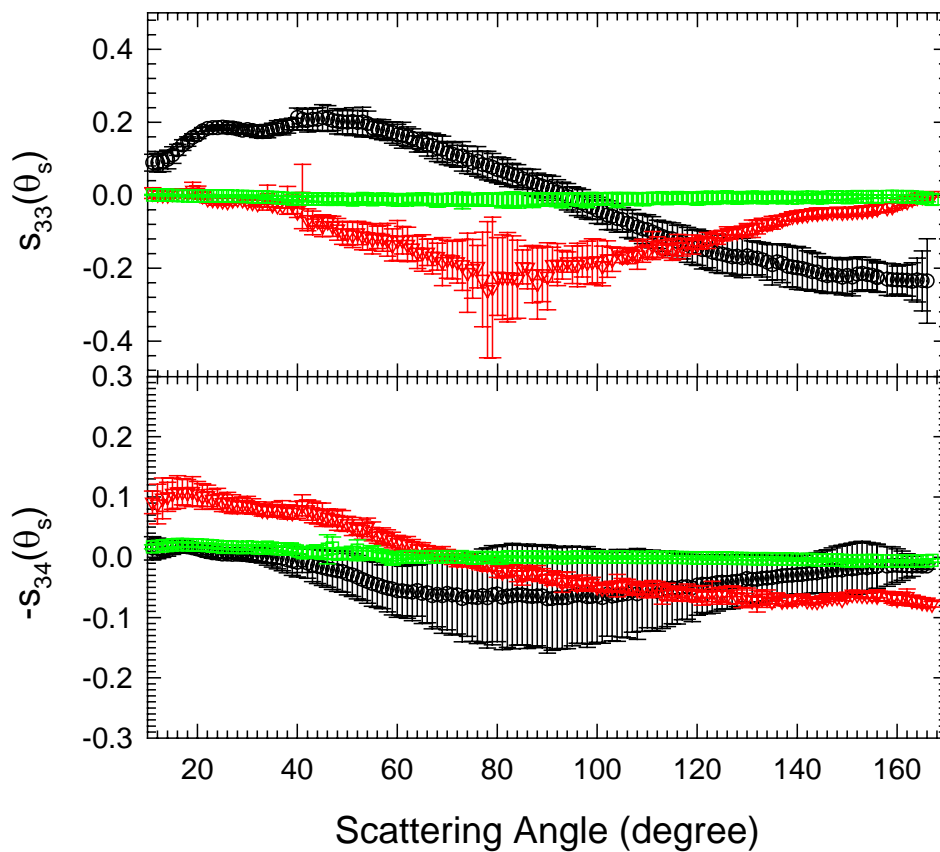


Figure 4-19 Same as Figure 4-14 for the angle-resolved Mueller matrix elements  $s_{33}(\theta_s)$  and  $-s_{34}(\theta_s)$  of HL-60 cell suspension samples at the wavelengths of 442, 633 and 850nm.

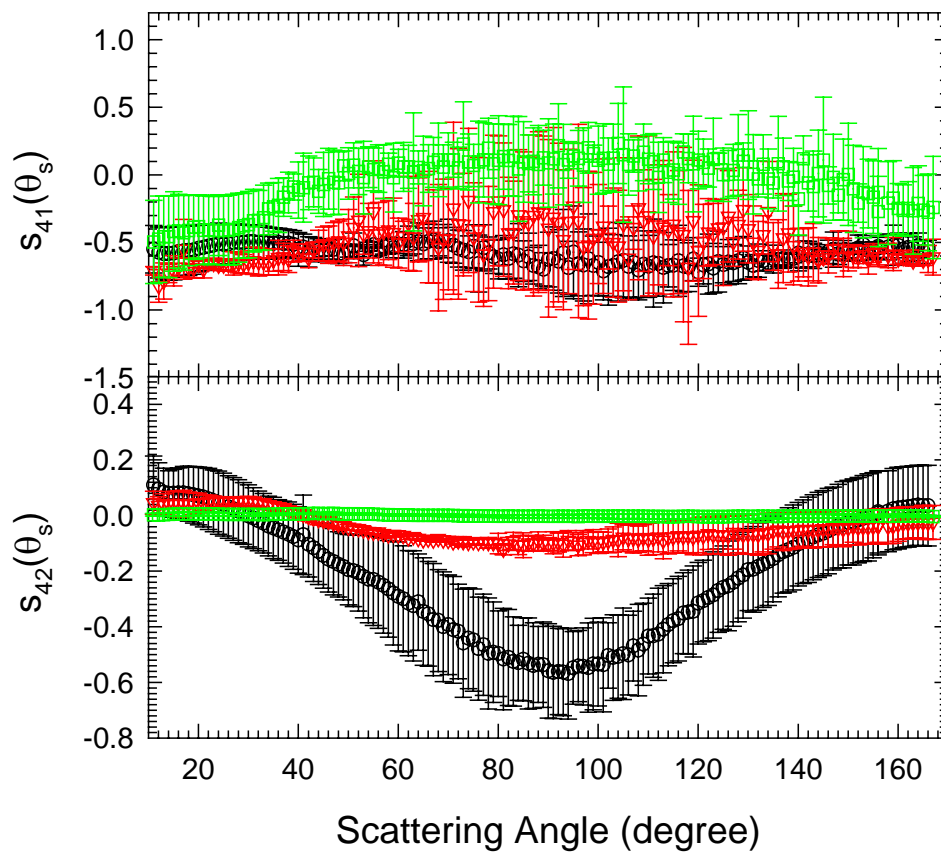


Figure 4-20 Same as Figure 4-14 for the angle-resolved Mueller matrix elements  $s_{41}(\theta_s)$  and  $s_{42}(\theta_s)$  of HL-60 cell suspension samples at the wavelengths of 442, 633 and 850nm.

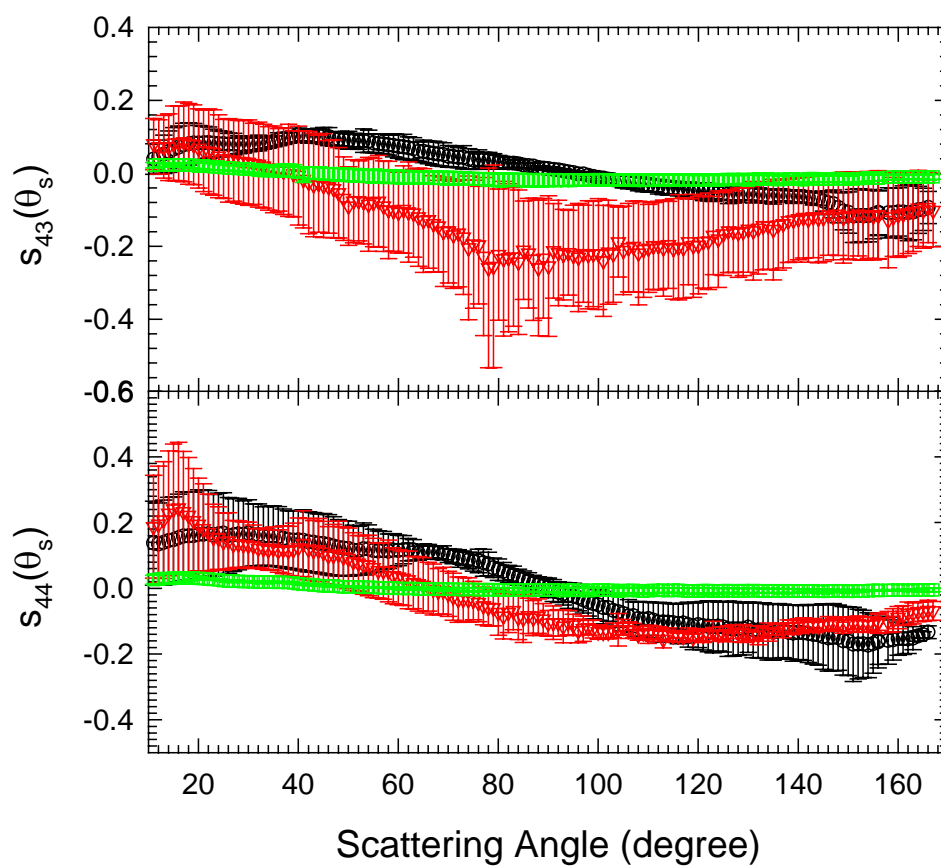


Figure 4-21 Same as Figure 4-14 for the angle-resolved Mueller matrix elements  $s_{43}(\theta_s)$  and  $s_{44}(\theta_s)$  of HL-60 cell suspension samples at the wavelengths of 442, 633 and 850nm.

## **Chapter 5 Study of Turbid and Skin Samples**

In this Chapter, we present the results of experimental and modeling studies of turbid and skin samples. First, the system calibration with water is discussed, which is followed by the refractive index determination of turbid samples at eight different wavelengths by the measurement of the coherent reflectance curves. The distribution of diffuse reflection and the pressure dependence for tissue samples are discussed, and the results of refractive index for porcine and human skin are shown for both the dermis and epidermis samples.

### **5.1 System Calibration with Water**

Deionized water was used to calibrate our reflectometry system because its refractive index and dispersion relation are well known (Eisenber.H 1965; Kurtz, Wikings.Ae et al. 1965; Zuev and Sonchik 1969; Hale and Query 1973). The coherent reflectance curve  $R(\theta)$  of deionized water has been measured and provides baseline data for investigations of diffusely reflected light contribution to  $R(\theta)$ . The incident beam, modulated at 370Hz with a mechanical chopper (SR540, Stanford Research System), was provided by one of seven cw lasers generating radiation at eight wavelengths of 325, 442, 532 (AMGM5, Beta Electronics), 633, 850, 1064 (Nd: YAG, DPIR-2300, Casix), 1310 (ML776H8F, Mitsubishi Electric) and 1550 (ML976H6F, Mitsubishi Electric) nm with  $I_0$  adjusted to be 05-4  $\mu$ W. The incident beam was linearly polarized in either s or p-orientation with a Glan-Thompson polarizer (PRH8010, Casix). Two Si or GaAs photodiodes were used to measure  $I_0$  and  $I_R$  with a pinhole of 2mm diameter in front of

the photodiode on the reflection side of the prism to reduce contribution of diffuse reflection to  $I_R$ . The control of the four stepping motors and acquisition of  $I_R$  data with a lock-in amplifier and  $I_0$  data with a A/D board were accomplished with an in-house developed software through a PC. The incident angle  $\theta$  was varied between  $46^\circ$  and  $80^\circ$  with a step size of  $0.125^\circ$  and resolution of  $0.0064^\circ$  and the rotation angles and translation distances of the prism and photodiode were tabulated for each  $\theta$  at different wavelengths. Water was injected into the sample holder using a 10ml syringe and air bulbs were carefully removed before measurement to avoid the scattering on the sample-glass interface.

Typical results of the coherent reflectance curves of  $R_s(\theta)$  and  $R_p(\theta)$  measured with a s-polarized and p-polarized incident beam, respectively, from a sample of deionized water at 633nm were shown in Fig. 5-1. The calculated coherent reflectance curves based on the Fresnel's equations (see section 2.8) were fitted to the measured data by adjusting the refractive index of the sample. The agreement between the calculated and measured data was gauged by a coefficient of determination  $R^2$  (see section 2.8) at about 0.999. The real refractive index  $n_r$  was determined from the fitting as 1.332 and 1.333 for s- and p-polarization, respectively, while the imaginary index  $n_i$  as less than  $5 \times 10^{-4}$ , representing the lower limit of  $n_i$  determination by this method. These measurements were repeated at other 7 wavelengths and the values of  $n_r$  agreed well with the published values (Hale and Querry 1973) within the experimental error.

## 5.2 The Complex Refractive Index of Liquid Solution

We choose the sphere suspension and intralipid solution as the turbid samples to study the refractive index because they have been used widely as the tissue phantoms (Flock, Jacques et al. 1992). Different concentrations of intralipid (diluted from the original 20% solution) (Fresenius Kabi Clayton, L.P.) are measured at different wavelengths to obtain the dependence of refractive index on concentrations and wavelengths by plotting the experimental results.

We first studied if the reflected light signals measured with the photodiode (PD2 in Fig. 3-10) would correctly yield coherent reflectance for the turbid samples of intralipid and skin tissues. For this purpose, the collimated beam of  $\lambda=633\text{nm}$  was used to measure the distribution of light reflected from the interface between the sample and prism at either  $\theta = 45^\circ$  or  $75^\circ$  by rotating the photodiode PD2 around the center of the fixed prism base. The reflected light signal was measured between  $-4^\circ$  and  $4^\circ$  on both sides of the incident angle and was plotted in Fig. 5-2 against the rotation angle of PD2. The ratio of specular reflection to diffuse reflection, which was obtained by dividing the reflected light signal at  $0^\circ$  to that at  $3.5^\circ$ , was about 1000 for water and 100 for dermis at  $45^\circ$ , 400 and 300, respectively, at  $70^\circ$ . These results demonstrate that the coherently reflected light is much larger than the diffusely reflected light even for skin tissue samples.

To understand the interaction of light wave with a turbid medium, we have selected suspensions of polystyrene microspheres with diameter  $d=1.0\mu\text{m}$  and 10%

concentration by weight in distilled water (5100B, Duke Scientific Corporation) as the turbid samples for our study. We determined the complex refractive index for microsphere suspensions at eight wavelengths from 325nm to 1550nm. The results obtained at the wavelength 633nm were shown in Fig. 5-3. The dependence of the real part of the refractive index on wavelength was shown in Fig. 5-4. Each value was obtained by fitting one of three reflectance measurements for  $R_s$  or  $R_p$ . The real refractive index showed a normal dispersion relation of index decreasing with increasing wavelength. However, an oscillation of the index as a function of wavelength can be seen clearly.

We have also determined the refractive index of intralipid solution samples at different concentrations by diluting the 20% intralipid with deionized water. The liquid sample was in contact with the prism base within a sample holder centered at the prism base. The measurements of  $R_s(\theta)$  and  $R_p(\theta)$  were repeated three times for each sample to obtain the mean values of complex refractive indices by nonlinear regression of each coherent reflectance curve at different intralipid concentrations and wavelengths. The agreement between the measured values of  $R_s(\theta)$  and  $R_p(\theta)$  and the calculated ones from Fresnel's equations was acceptable with  $R^2$  above 0.990 and thus very close to that of the deionized water. One typical coherent reflectance curve of 20% intralipid was depicted in Fig. 5-5 at a wavelength of 633nm. The concentration dependence of the mean value of real refractive index at all 8 wavelengths was found to be linear and two examples at  $\lambda=442$  and 1310nm were shown in Fig. 5-6. For wavelengths larger than 600nm the imaginary refractive indices were less than the accuracy afforded by the reflectometry

system,  $1 \times 10^{-3}$ , and thus appeared fluctuating. For short wavelengths, such as 442nm, the imaginary index was sufficiently large and revealed concentration dependence close to linear. The wavelength dependence of the complex refractive index of the 20% intralipid sample was presented in Fig. 5-7. The parameter  $R^2$  had a range from 0.970 to 0.999. The total uncertainty in  $n$  was estimated to be about  $\Delta n_r = \pm 0.002$  and  $\Delta n_i = \pm 0.001$ .

The uncertainty of the refractive index determination mainly depends on the accuracy on the incident angle determination as well as fitting with Fresnel's equations. The essential experimental apparatus was depicted in Fig. 3-11. Two factors need be taken into account for the error on the incident angle determination:

- 1) **Stepping motor (motor 1) accuracy.** Considering the reality that the steps of the motor movement may be lost during the measurement period, we carried out a group of calibrations and obtained that an average of 15 per 7500 steps were lost.

And this causes the angle difference  $\Delta\theta_1$  given by

$$\Delta\theta_1 = k \cdot \tau, \quad (5.1)$$

where  $k$  is the number of steps lost and  $\tau$  is the angular resolution of the motor.

This gives  $\Delta\theta_1 = 0.0064^\circ \times 15 = 0.096^\circ$ ;

- 2) **Alignment.** The experimental alignment may cause the angle determination error  $\Delta\theta_2$  as (see Fig. 5-8):

$$\Delta\theta_2 = 2\Delta x / L, \quad (5.2)$$

where  $\Delta x = 1.0\text{mm}$  is the diameter of the laser beam and  $L=900\text{mm}$  is the distance between the prism and the pin hole used for alignment. This gives  $\Delta\theta_2=0.0022^\circ$

Consider an example case that the real critical angle for the sample is  $62^\circ$  and the wavelength employed for the experiment is  $633\text{nm}$ . The difference on the index determination caused by the total angle determination error ( $\Delta\theta_1+\Delta\theta_2$ ) is

$$\Delta n = n_{633} \cdot [\sin(62^\circ + \Delta\theta_1 + \Delta\theta_2) - \sin 62^\circ] = 0.0012 \quad (5.3)$$

### 5.3 Refractive Index Determination for Skin Tissues

Skin tissue is composed of two major layers: epidermis and dermis, and two examples of skin slides are shown in Fig. 5-9. The complex refractive index has been obtained at 8 different wavelengths between  $325$  and  $1550\text{nm}$  for both the epidermis and dermis samples. With these data we investigated various dispersion schemes for interpolation of the index data at other wavelengths in this spectral region.

#### 5.3.1 Results for Porcine Skin Tissues

Porcine skin tissues have been used widely as an animal model of the human skin tissues because of their closest similarity among mammals to those of the human skin (Lavker, Dong et al. 1991). We have determined the complex refractive indices of fresh porcine skin tissues that were obtained from the dorsal neck area of white domestic 6-month old pigs at the Brody School of Medicine, East Carolina University. Good contact between a skin sample and the prism base is important to eliminate or reduce air gaps

over the illuminated area and reduce surface roughness of the skin samples. To achieve this goal, we designed a sample holder in which the skin tissue was pressed against the prism by a pistol pressurized with a nitrogen gas cylinder to maintain a constant pressure (Fig. 5-10). By pressing either the epidermis or dermis side of the skin sample against the prism base, the coherent reflectance curves of skin epidermis or dermis were measured, respectively. To determine a proper pressure for skin sample measurements, the effect of the pressure on the index determination need be evaluated. An observable structure change from the fresh skin sample was found when a high pressure ( $>5.0 \times 10^5$  Pa) was employed which was mainly caused by the fast dehydration under the condition of high pressures. The dependence of the real refractive index of a porcine skin dermis sample on applied pressure was shown in Fig. 5-11. It can be seen from the data that the real index is not sensitive to air pressure between  $2 \times 10^5$  and  $5 \times 10^5$  Pa and all our subsequent measurements of coherent reflectance of skin tissue samples were carried out at a fixed pressure of  $2.06 \times 10^5$  Pa (30psi or 2.0atm).

At each of the 8 wavelengths, 3 skin samples from different pigs were used to measure the coherent reflectance curves of  $R_s(\theta)$  and  $R_p(\theta)$ . The measurement was repeated three times for each sample and typical results of  $R_s(\theta)$  and  $R_p(\theta)$  were shown in Fig. 5-12 for the dermis and epidermis of a skin sample, the top one was the example for “good fitting” with  $R^2$  larger than 0.99 and the bottom one was shown for the low limit on  $R^2$  about 0.92. Nonlinear regressions of  $R_s(\theta)$  and  $R_p(\theta)$  data by the Fresnel’s equations were worse than the cases of water and intralipid samples with  $R^2$  ranging between 0.920 and 0.999. Among a total of about 140 measurements of the porcine skin

dermis samples, a majority of 94% had  $R^2$  larger than 0.990 with only 6% between 0.97 and 0.99. In contrast, more than half (57%) of the 140 measurements for porcine skin epidermis had  $R^2$  ranging from 0.97 to 0.99 with 28% larger than 0.990 and 15% between 0.92 and 0.97. This difference may be attributed to the different surface conditions of the skin samples. The surface of a fresh porcine skin sample is a horny layer of stratum corneum with dead keratinocytes and embedded hairs, after surface cleaning with scissors, and thus is harder and less homogeneous than the dermis side of the prepared skin samples. Even under a pressure of  $2.06 \times 10^5$  Pa to achieve good contact with the prism, the epidermis-prism interface is expected to have a significant degree of roughness that causes more contribution of diffuse reflection to  $R(\theta)$  than that of the deep soft reticular dermis side of porcine skin samples. It is for these reasons that coherent reflectance need be measured at a large number of incident angles, especially those over  $65^\circ$ , to minimize the surface effect on the real refractive index determination through nonlinear regression. The mean values and standard deviations of the complex refractive index from 9 measurements with a s- or p-polarized beam were plotted as a function of wavelength in Fig. 5-13 for the porcine skin epidermis and Fig. 5-14 for the dermis.

### **5.3.2 Human Skin Results**

Fresh human skin tissue patches were obtained from the patients undergoing abdominoplasty procedures at the plastic surgery clinic of the Brody School of Medicine, East Carolina University. The complex refractive index for both the epidermis and dermis tissues has been obtained at the same 8 wavelengths. We obtained one skin tissue patch

from each of the 12 female patients with ages between 27 and 63-year old, 10 are Caucasian and 2 are African Americans, with the skin data information compiled in Table 5-1. All reflectance curve measurements were performed at the room temperature within 30 hours after the abdominoplasty procedure.

Two typical sets of coherent reflectance curves from the epidermis and dermis sides of the skin samples of two patients with different skin types were presented in Fig. 5-15 together with the fitted curves based on the Fresnel's equations. To determine the sensitivity of the refractive index on the nonlinear regression, we analyzed the relation between  $R^2$  and  $n$  with selected data of the coherent reflection curves and typical results were shown in Fig. 5-16. Based on this analysis, we estimated that the uncertainty in obtaining the real and imaginary refractive index was about  $\Delta n_r = \pm 0.006$  and  $\Delta n_i = \pm 0.005$ , respectively, for the turbid tissues of both the epidermis and dermis. At each wavelength, 8 or 12 skin samples from each of 2 or 3 patients were used to measure the coherent reflectance curves of  $R_s(\theta)$  and  $R_p(\theta)$  with half for the epidermis measurement and half for dermis. The measurement of  $R_s(\theta)$  and  $R_p(\theta)$  was repeated three times on the same skin sample and thus the data set at each wavelength consisted of 12 or 18 curves with an incident beam of s- or p-polarization. Nonlinear regression to the coherent reflectance curve data by the Fresnel's equations was done individually to obtain the complex refractive index from each measurement. The coefficient of determination  $R^2$  ranged from 0.960 to 0.999 for the data from the measurement of the epidermis side and from 0.978 to 0.998 for the dermis side. The mean values and standard deviations of the complex refractive index have been calculated at each wavelength from the data sets.

These results were plotted as a function of wavelength in Fig. 5-17 for the epidermis samples and Fig. 5-18 for the dermis samples.

We investigated various dispersion schemes to identify appropriate ones for the calculation of real refractive index of human skin tissues at wavelengths between 300 and 1600nm based on our experimental results at 8 wavelengths. Among those reported on the index data of ocular tissues (Kroger 1992; Atchison and Smith 2005), we selected three schemes to fit to our data: the Cauchy dispersion equation

$$n_r = A + \frac{B}{\lambda^2} + \frac{C}{\lambda^4} \quad (5.4)$$

the Cornu equation

$$n_r = A + \frac{B}{(\lambda - C)} \quad (5.5)$$

and the Conrady equation

$$n_r = A + \frac{B}{\lambda} + \frac{C}{\lambda^{3.5}} \quad (5.6)$$

The coefficients of each dispersion scheme determined with the least-square principle from our index data were given in Table 5-2.

Table 5-1. The human skin sample data

ID #	age	Race	Tissue location	Skin type	Measurement
1	42	Caucasian	abdomen	III	Pressure dependence
2	40	Caucasian	abdomen	I	633nm,532nm
3	27	African American	abdomen	V	442nm
4	63	Caucasian	abdomen	II	1064, 850nm
5	56	Caucasian	abdomen	II	325,1550nm
6	54	Caucasian	arm	II	1310, 633nm
7	34	Caucasian	abdomen	II	1064, 325nm
8*	55	Caucasian	abdomen	I	532,633nm
9*	49	Caucasian	abdomen	III	442,1310nm
10*	41	Caucasian	abdomen	II	850,1550nm
11*	39	African American	abdomen	V	532, diffuse reflection
12	44	Caucasian	abdomen	III	Pressure dependence

\* The skin structures of the samples from these patients have been examined through histology.

Table 5-2. The coefficients of different dispersion equations \*

Dispersion equation	A	B	C
Cauchy	1.3696	$3.9168 \times 10^3$	$2.5588 \times 10^3$
Cornu	1.2573	$4.5383 \times 10^2$	$2.8745 \times 10^3$
Conrady	1.3549	$1.7899 \times 10$	$-3.5938 \times 10^6$

\* These coefficients were obtained on the basis of Eqs. (5.4) to (5.6) with wavelength in the unit of nanometers.

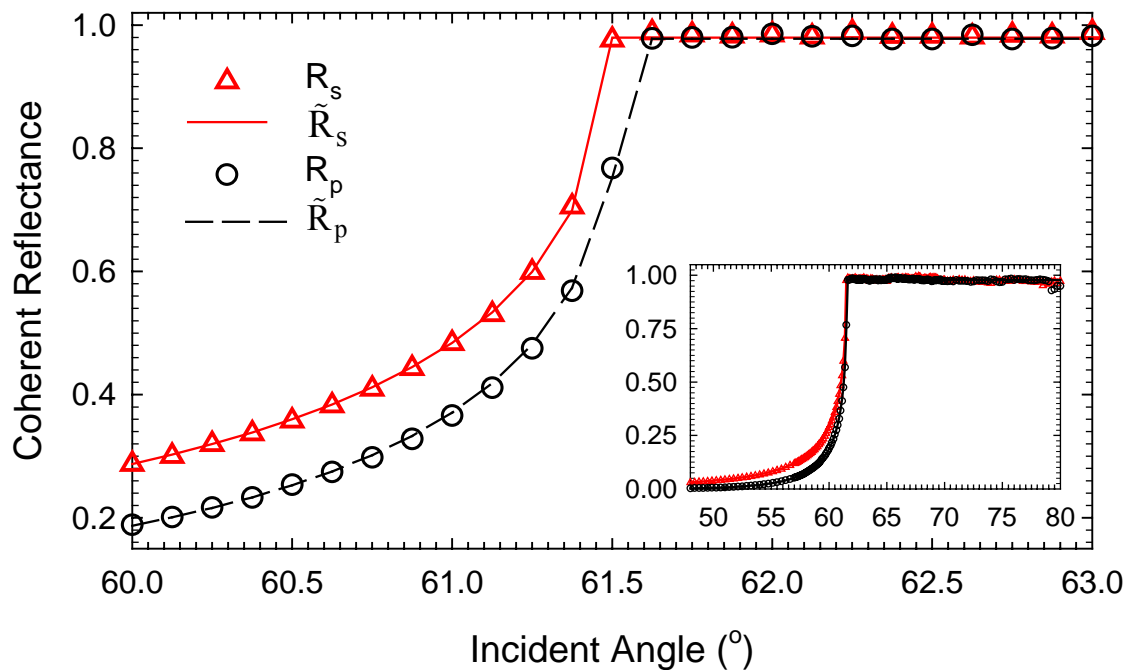


Figure 5-1 The measured and calculated coherent reflectance versus incident angle of deionized water with s- and p-polarized incident beam at  $\lambda = 633\text{nm}$ . Insert: full angular range.

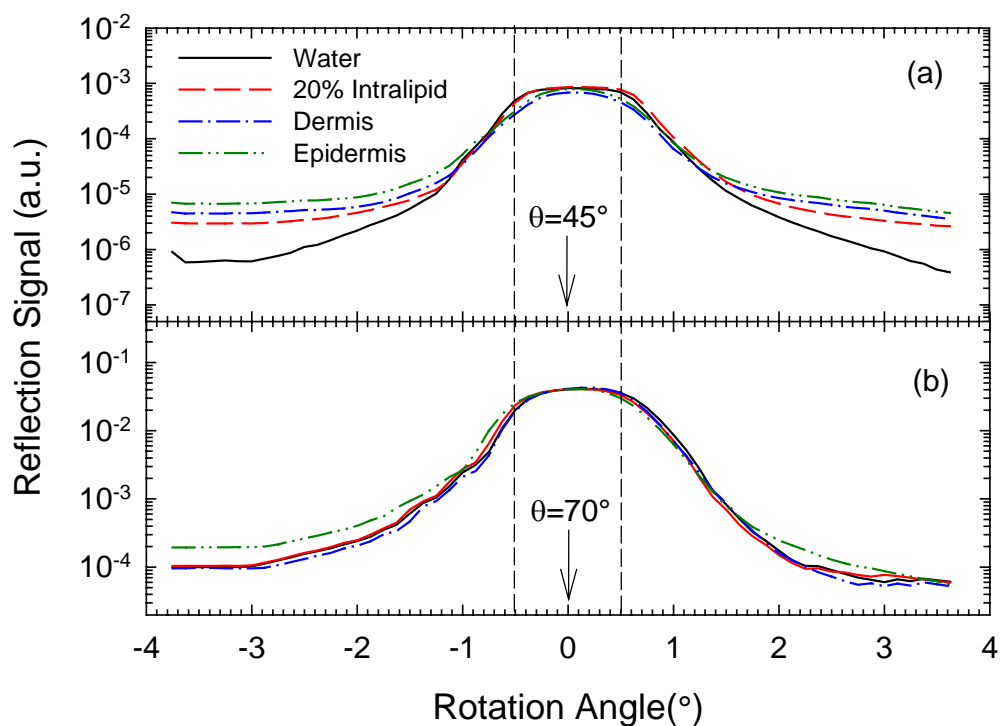


Figure 5-2 The reflection signal versus rotation angle of the detector at the incident angle of (a)  $\theta=45^\circ$ ; (b)  $\theta=70^\circ$  with a s-polarized beam at  $\lambda=633\text{nm}$  for deionized water, 20% intralipid solution, porcine skin epidermis and dermis with an angular stepsize of  $0.125^\circ$ . The error bars of about  $\pm 5\%$  were removed for clear view and the two dashed lines indicate the angular acceptance range of the aperture in front of the photodiode.

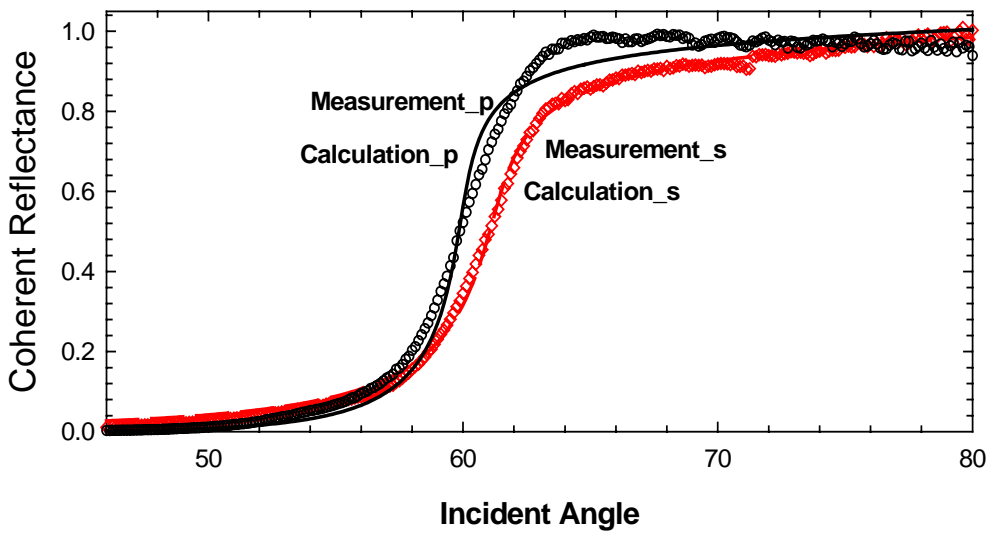


Figure 5-3 Measured (symbols) and calculated (lines) coherent reflectance versus incident angle for 10% sphere suspension at 633nm for both s and p polarization.

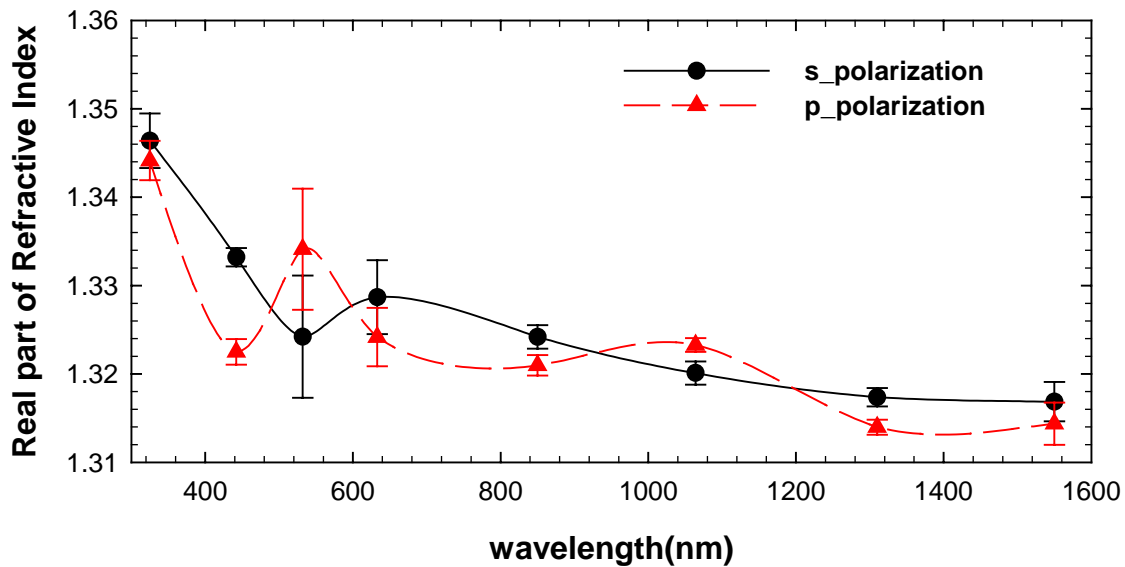


Figure 5-4 Wavelength dependence of the refractive index for 10% sphere suspension. Each data point and associated error bar are the mean and standard deviation obtained from 3 measurements. The lines are for guide of the eyes.

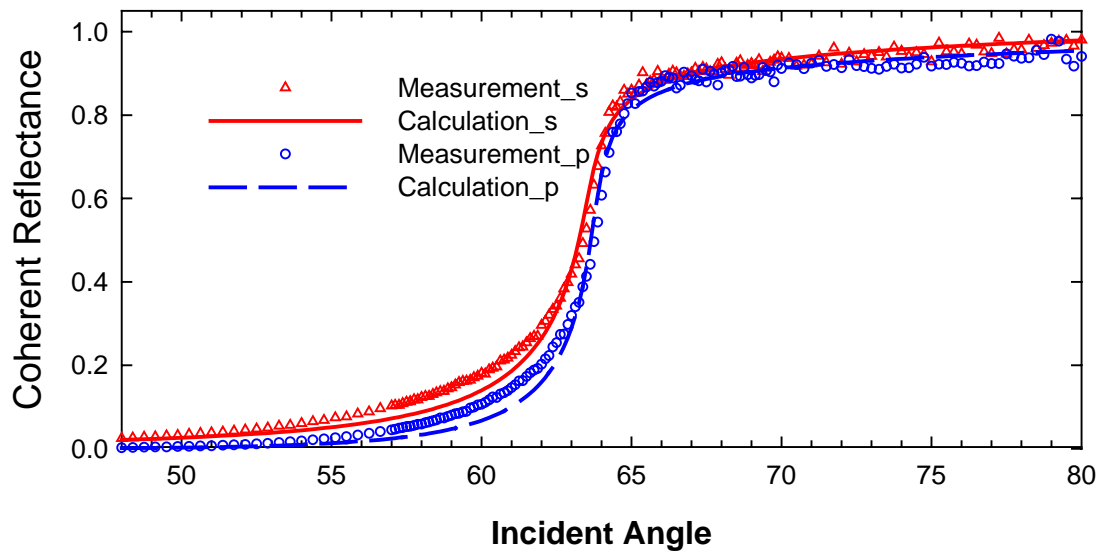


Figure 5-5 Refractive index measurement of 20% intralipid at 633nm for both s and p polarization.

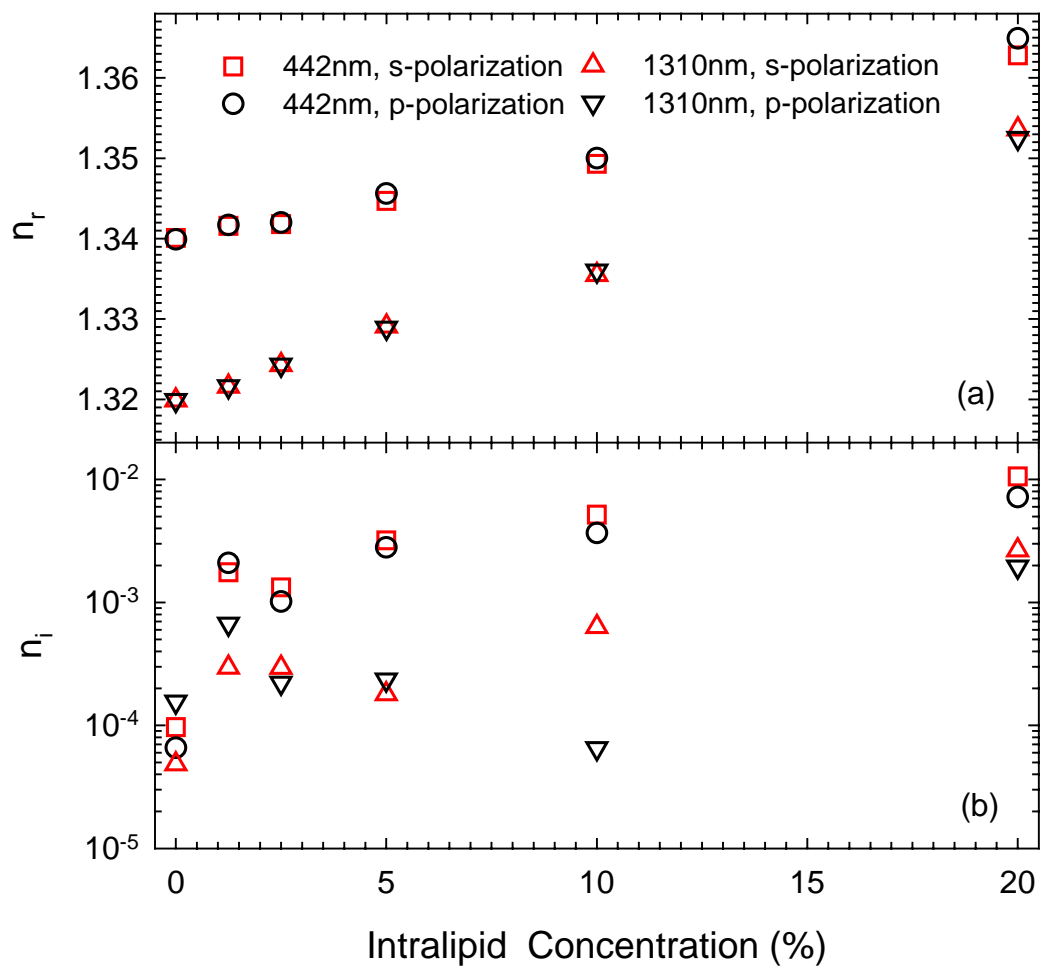


Figure 5-6 The refractive indices of intralipid samples versus concentration. (a) real part; (b) imaginary part.

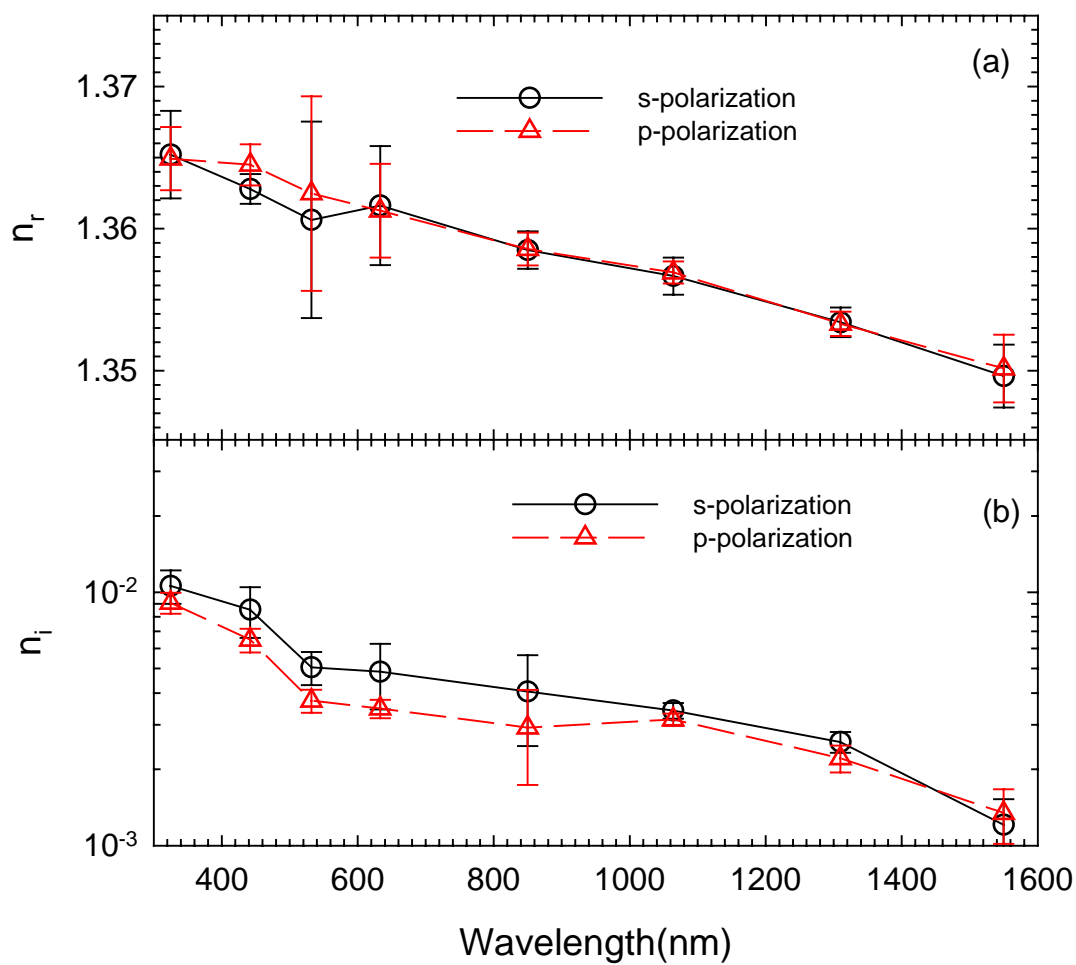


Figure 5-7 The (a) real and (b) imaginary refractive indices of 20% intralipid versus wavelength. Each data point and associated error bar are the mean and standard deviation obtained from 3 measurements. The lines are for guide of the eyes.

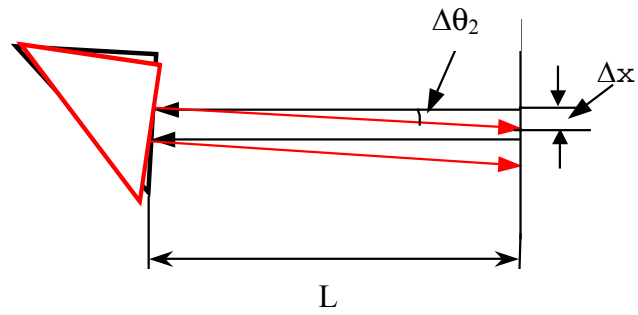


Figure 5-8 Effect of laser beam diameter on angle determination accuracy.

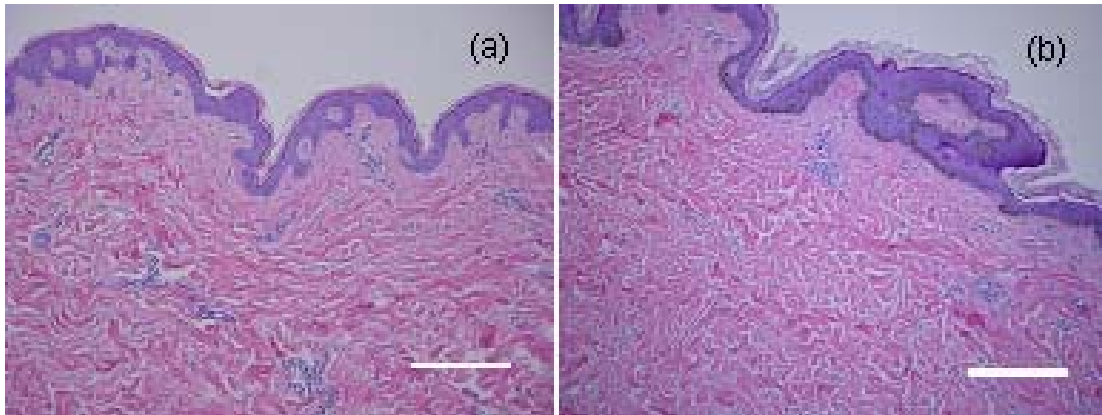


Figure 5-9 The microscope images of the histology slides of the skin samples from two patients: (a). ID no. 9 (skin type: III); (b). ID no. 11 (skin type: V). Bar = 100 $\mu$ m.

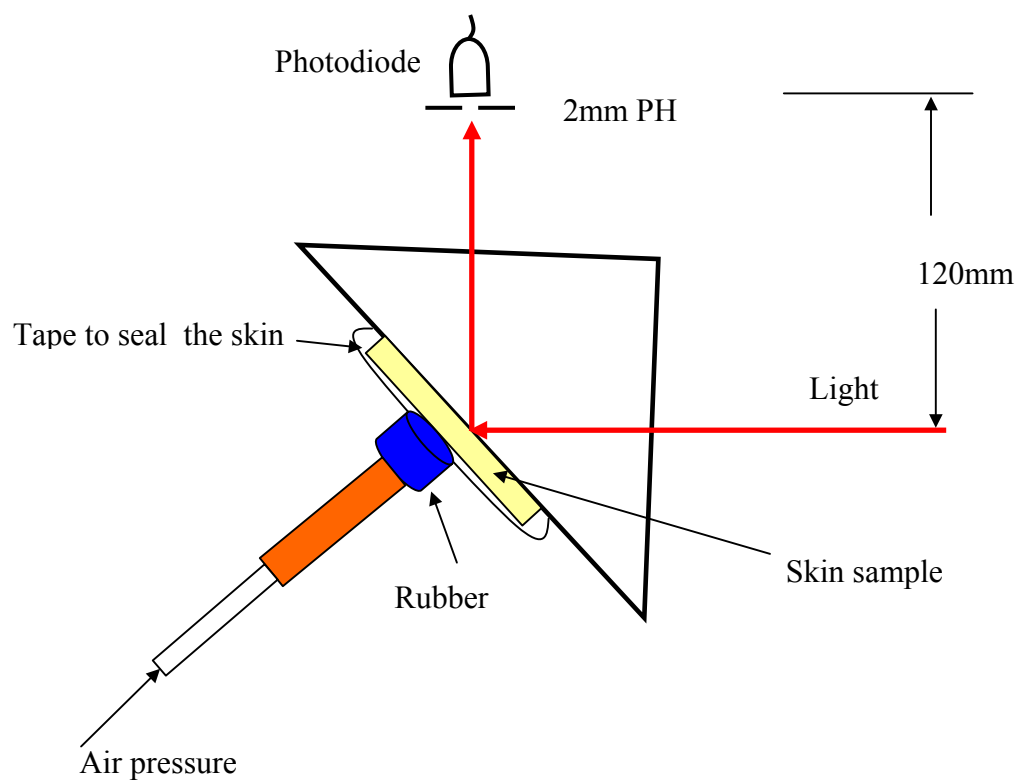


Figure 5-10 Schematic of skin tissue mounted for measurement. PH: Pin hole.

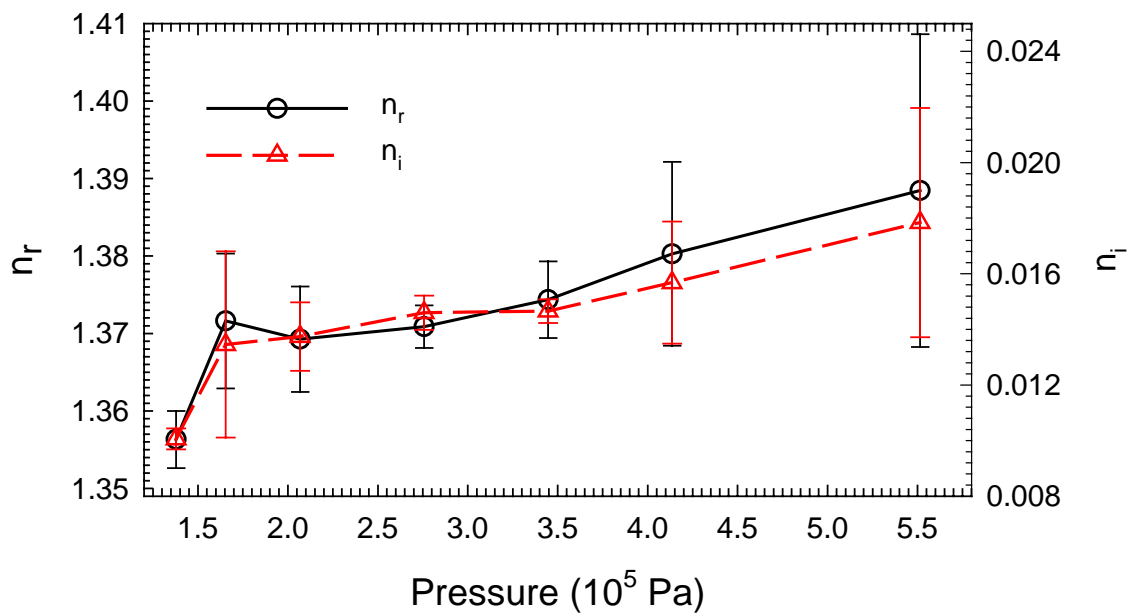


Figure 5-11 The real (circle) and imaginary (triangle) refractive index of porcine skin dermis versus pressure. Each data point and associated error bar are the mean and standard deviation obtained from 3 measurements. The lines are for guide of the eyes.

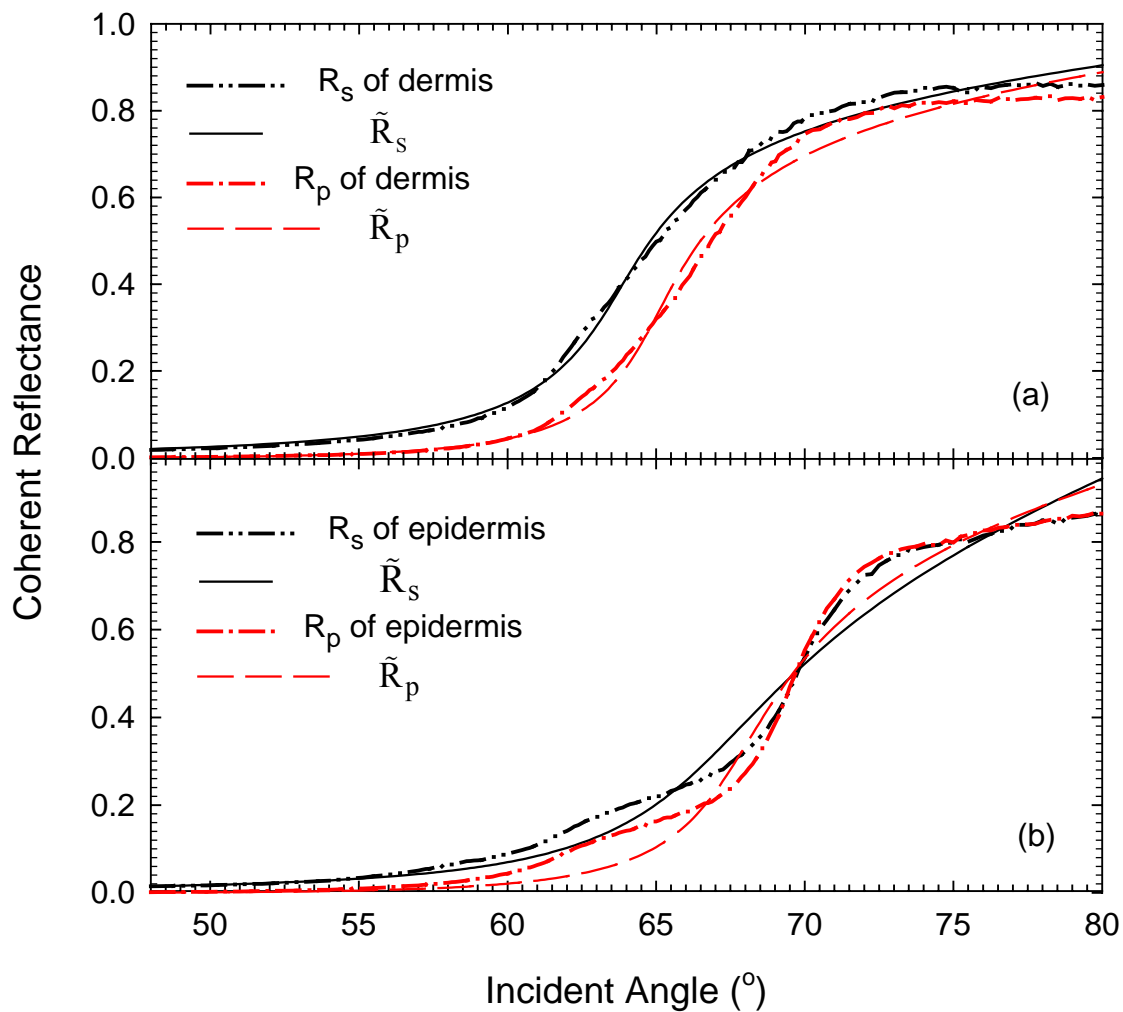


Figure 5-12 The coherent reflectance for porcine skin versus the incident angle at  $\lambda=1064\text{nm}$ : (a) dermis; (b) epidermis.

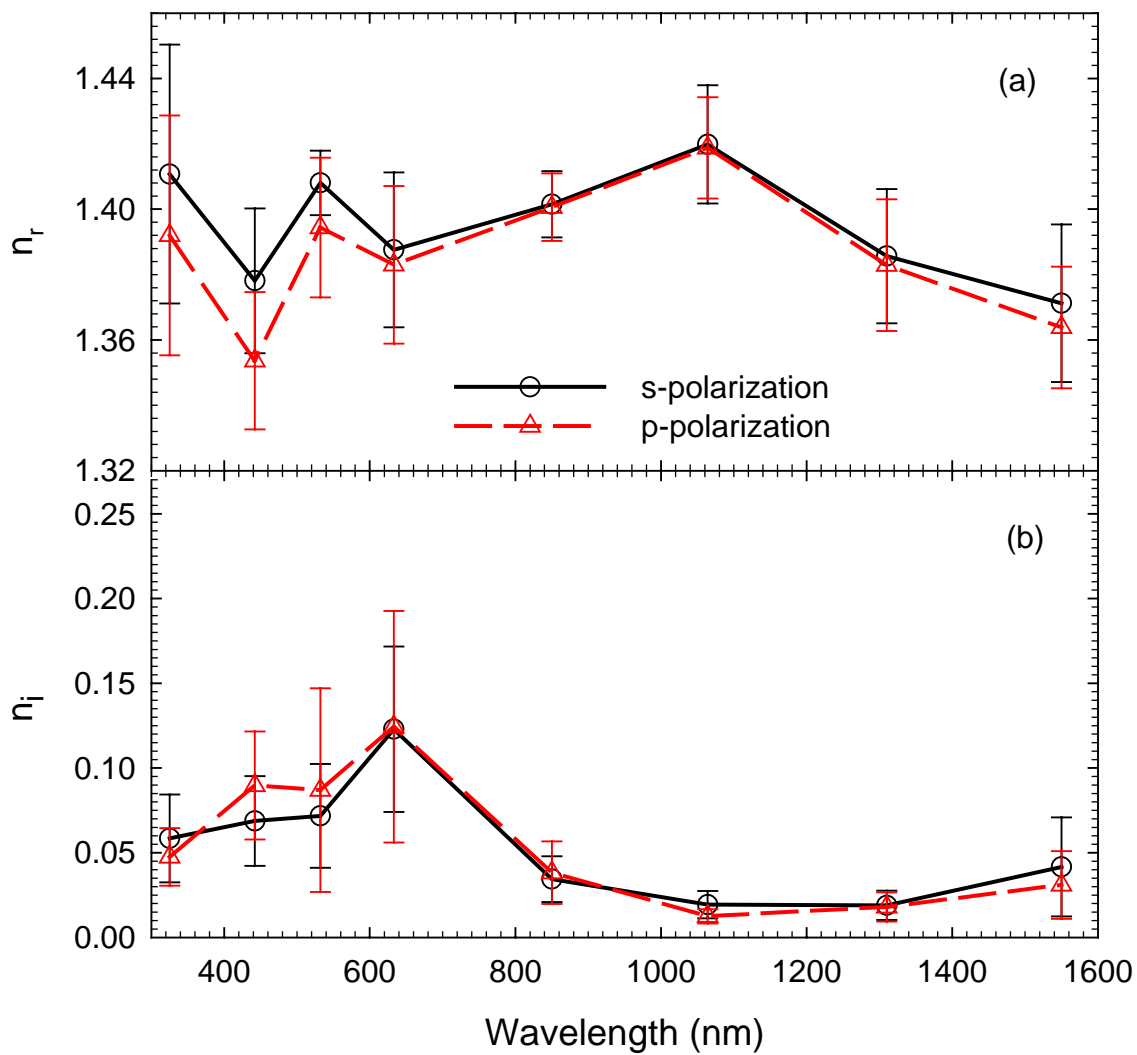


Figure 5-13 The (a) real and (b) imaginary refractive indices of porcine skin epidermis versus wavelength. Each data point and associated error bar are the mean and standard deviation obtained from 9 measurements. The lines are for guide of the eyes.

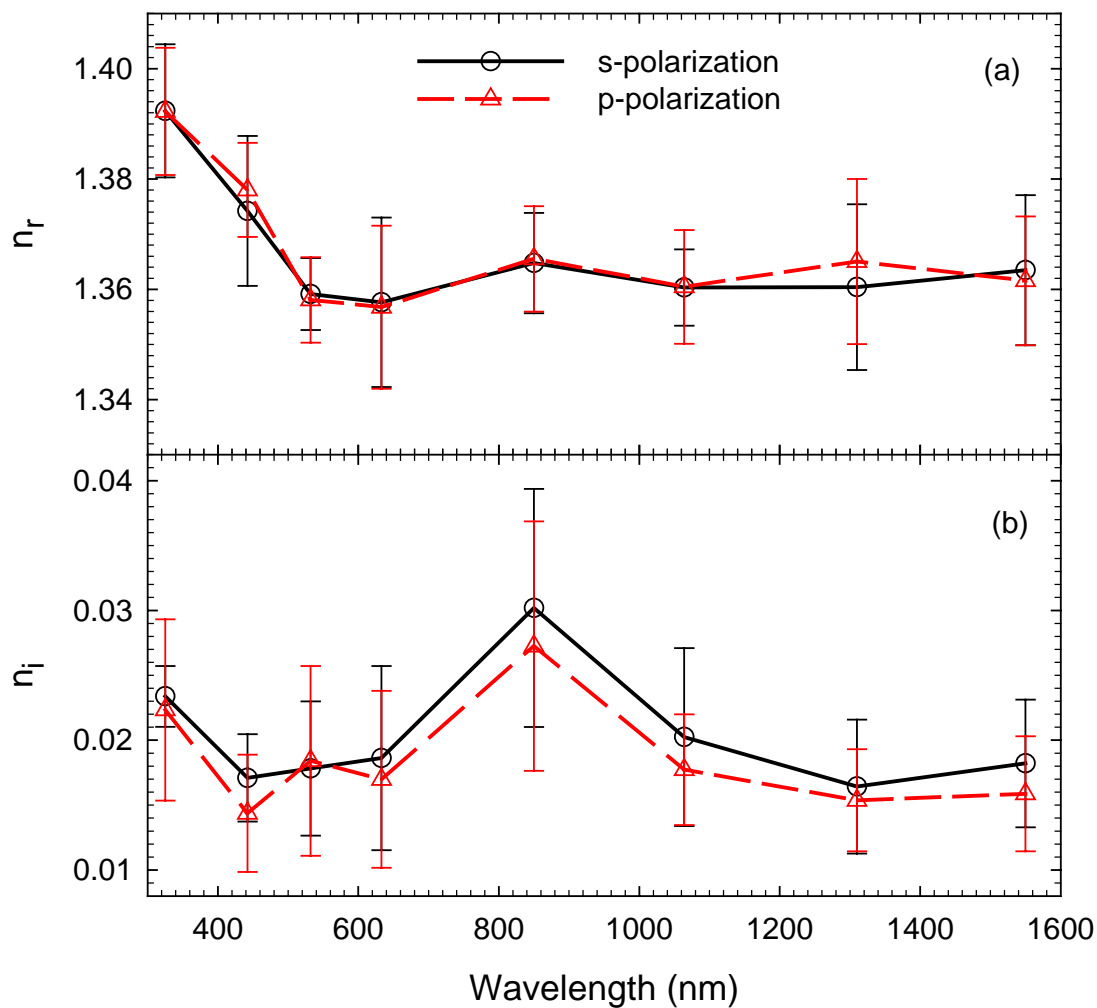


Figure 5-14 The (a) real and (b) imaginary refractive index of porcine skin dermis versus wavelength. Each data point and associated error bar are the mean and standard deviation obtained from 9 measurements. The lines are for guide of the eyes.

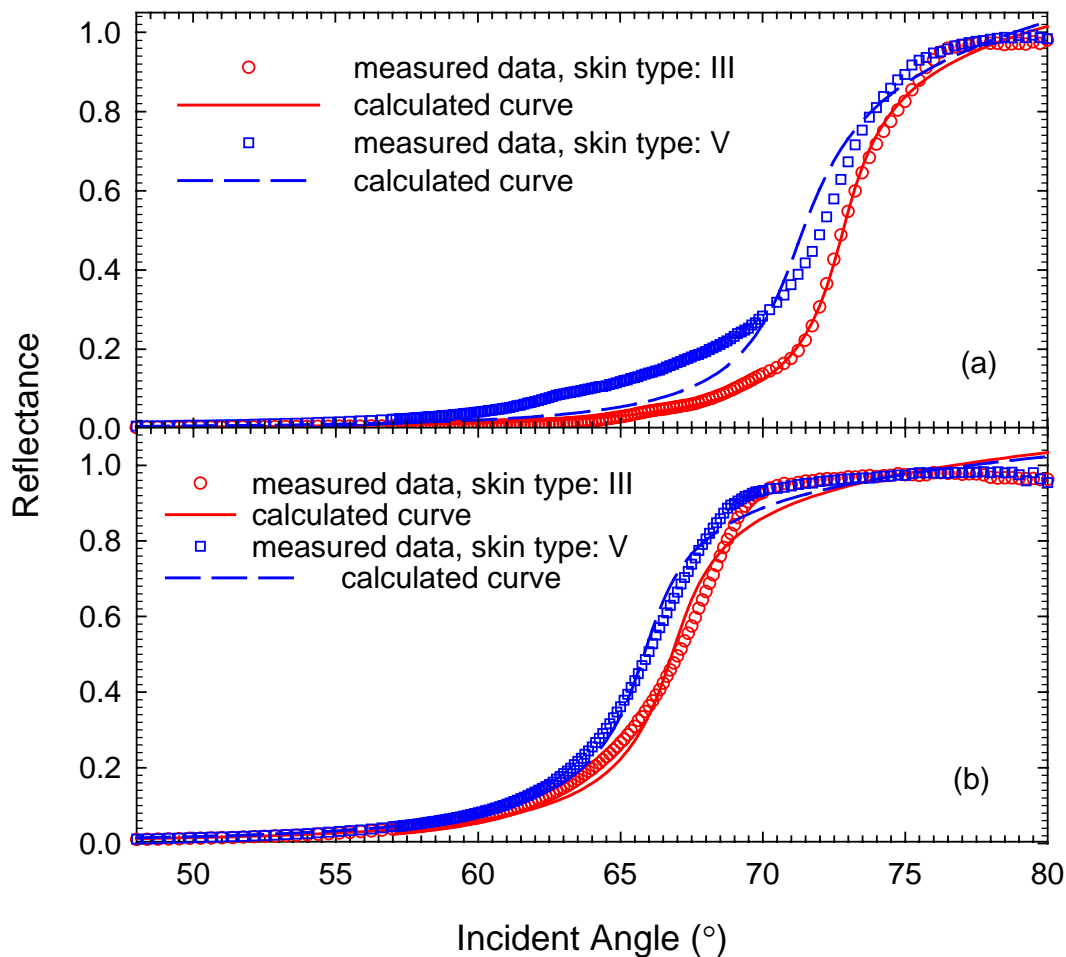


Figure 5-15 The typical measured coherent reflectance curves of two skin samples from two patients at  $\lambda=442\text{nm}$  with a s-polarized incident beam: (a) epidermis; (b) dermis. The solid lines are calculated curves based on the Fresnel's equations with the following values of the complex refractive index: (a)  $n = 1.445 + i1.00 \times 10^{-2}$  for ID #3 (skin type: V) and  $n = 1.458 + i8.34 \times 10^{-3}$  for ID #9 (skin type: III); (b)  $n = 1.394 + i9.30 \times 10^{-3}$  for ID #3 and  $n = 1.404 + i9.20 \times 10^{-3}$  for ID #9.

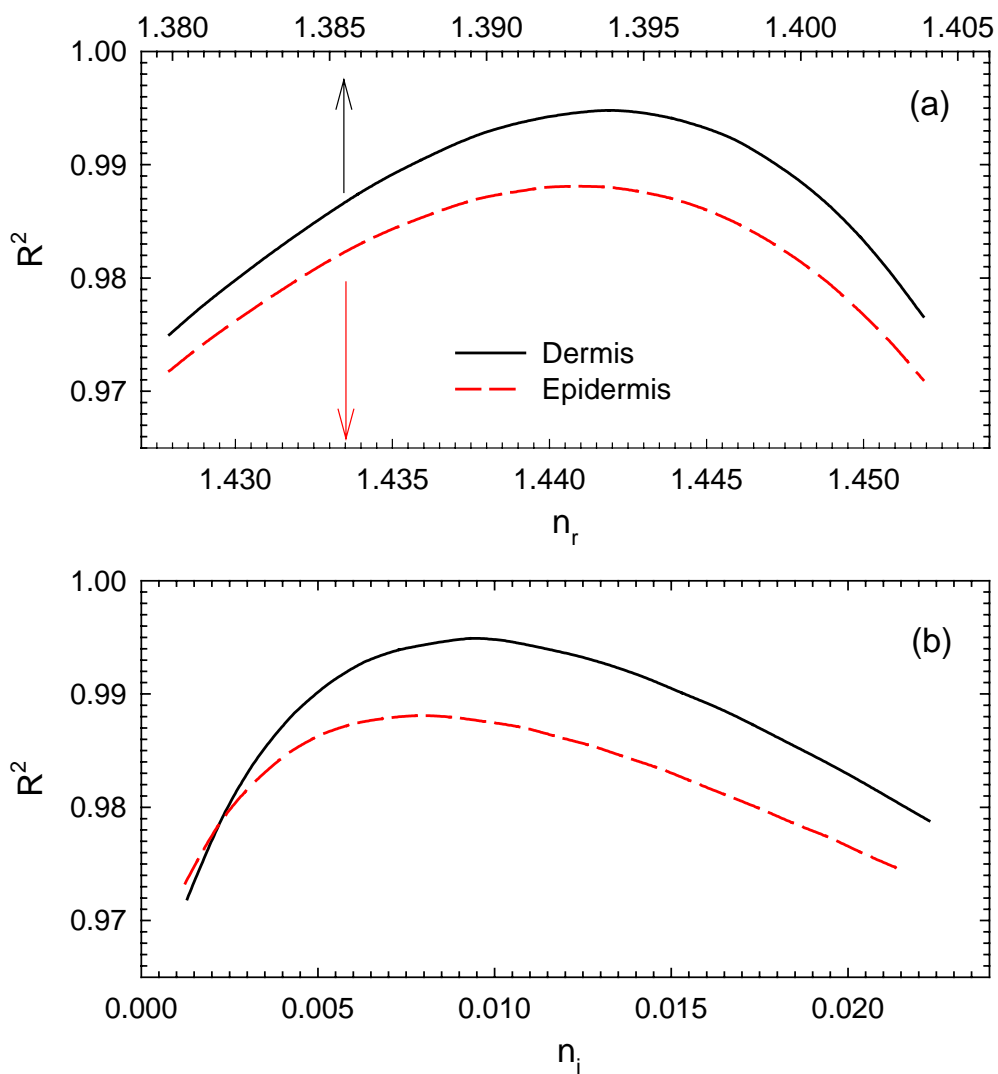


Figure 5-16 The dependence of the coefficient of determination  $R^2$  on different choices of  $n_r$  or  $n_i$  for a coherent reflectance curve measured from the epidermis or dermis side of a skin sample at  $\lambda=442\text{nm}$ .

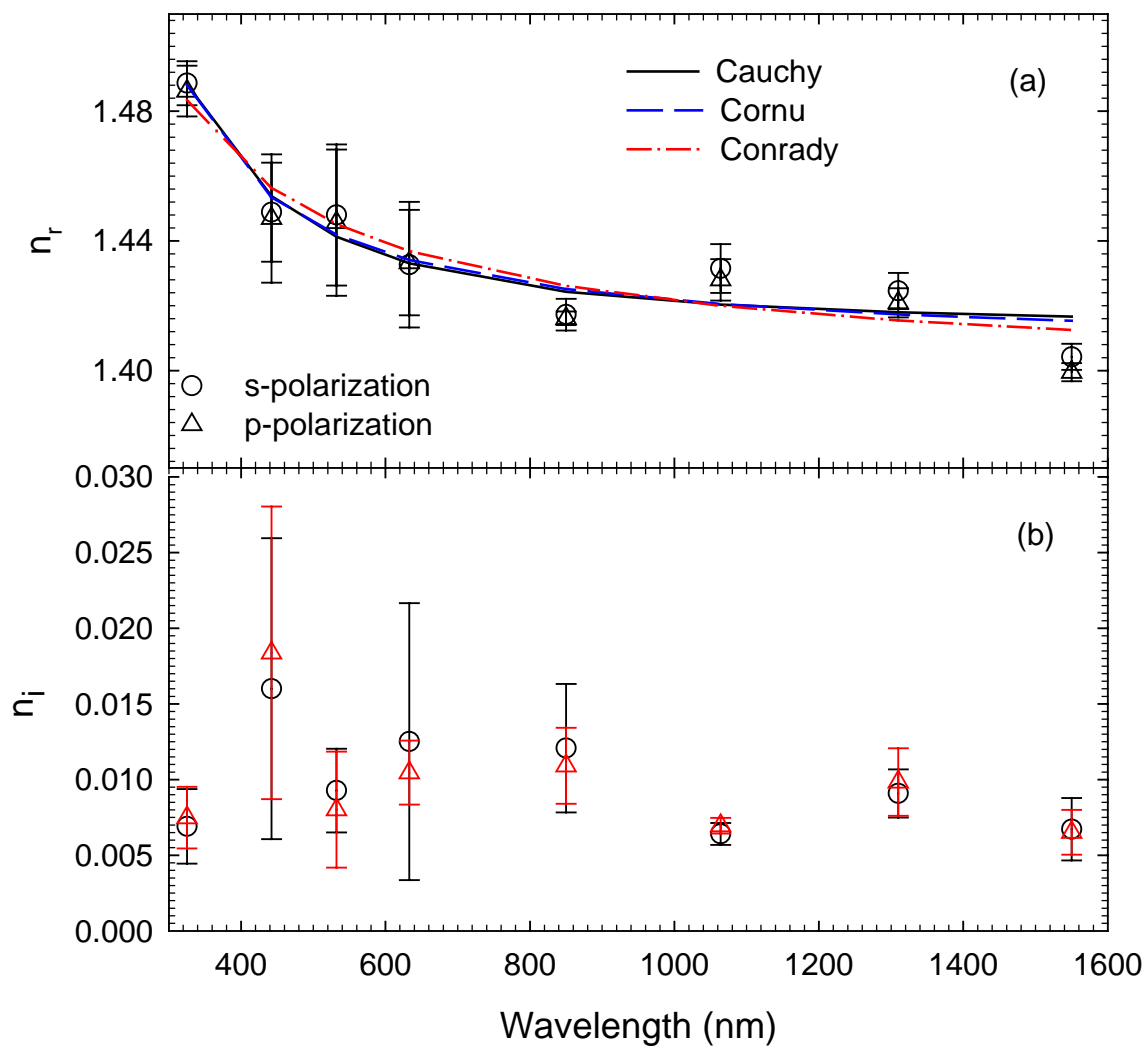


Figure 5-17 The (a) real and (b) imaginary refractive indices of human skin epidermis versus wavelength. Each data point and associated error bar are the mean and standard deviation obtained from 6 or 9 measurements of 2 or 3 skin samples. The lines in (a) are based on the dispersion equations.

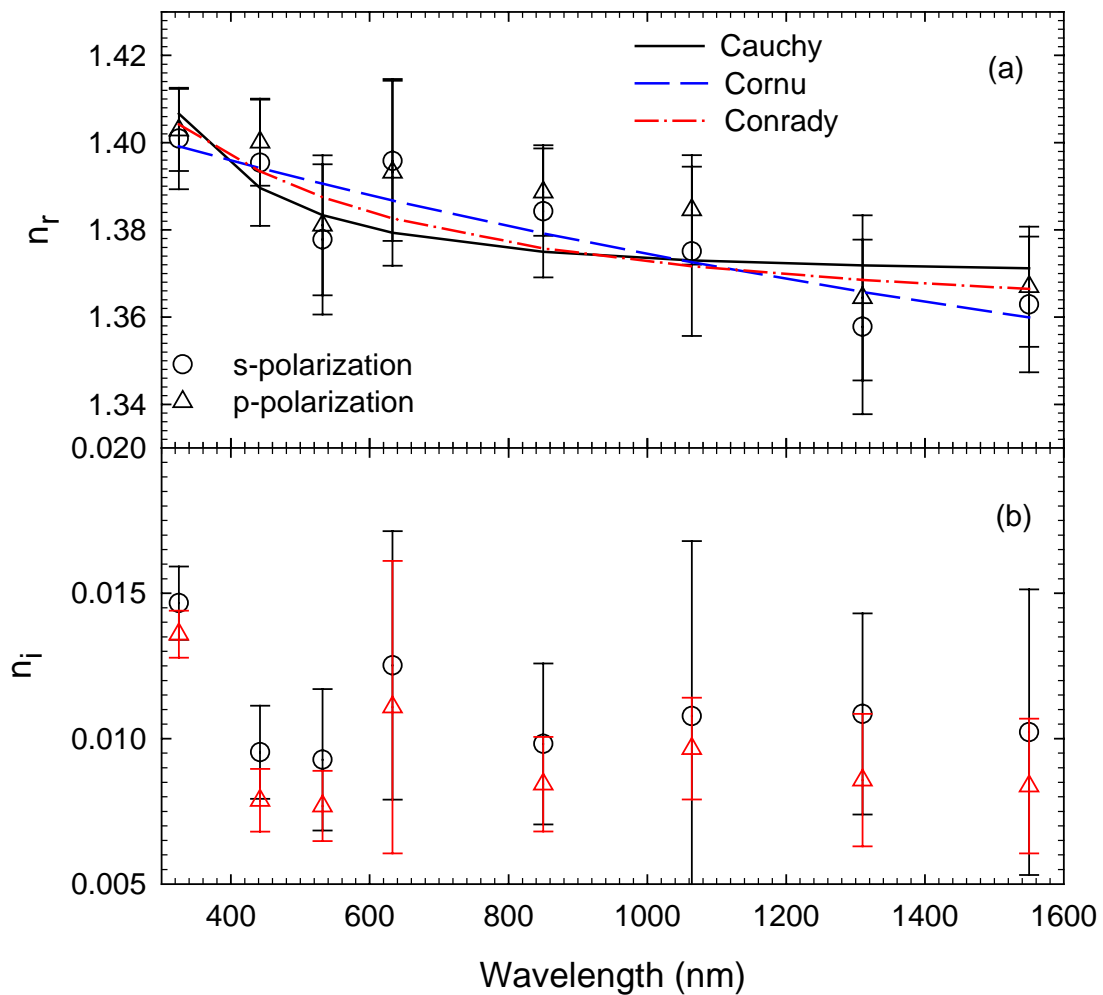


Figure 5-18 The (a) real and (b) imaginary refractive indices of human skin dermis versus wavelength. Each data point and associated error bar are the mean and standard deviation obtained from 6 or 9 measurements of 2 or 3 skin samples. The lines in (a) are based on the dispersion equations.

## Chapter 6 Discussions and Summary

The experimental results presented in Chapter 4 and 5 demonstrate that the fundamental cause of light scattering by biological cells and in tissues is due to the optical heterogeneity that can be expressed in terms of refractive index. To accomplish the specific aims stated at the beginning of this dissertation, a PEM based goniometer system has been successfully constructed, calibrated and applied to experimentally determine the sixteen Mueller matrix elements for two different types of cell suspensions. We have also built a prism-based reflectance system to measure the angular dependence of the coherent reflectance of turbid samples and skin tissues *in vitro* to determine their refractive index between 325 and 1550nm in wavelength. We discuss the implication of these results and provide a summary in this chapter.

### 6.1 Light Scattering by Cells

We determined the Mueller matrix elements of B-cells and HL-60 cells in suspension with a goniometer system. Previous research results have indicated that among the 16 elements, the elements of  $S_{12}$  and  $S_{34}$  are quantities correlating sensitively with the morphology of the probed cells (Bickel, Davidson et al. 1976; Perry 1978; Bickel and Stafford 1981; Menguc and Manickavasagam 1998; Volten, de Haan et al. 1998). We therefore focus our attention here on these two elements. Based on the definition of the Stokes parameters and Mueller matrix (see section 2.2), it is easy to show that the normalized element  $s_{12}$  represents the ability of a sample to scatter incident

light polarized parallel to the scattering (or horizontal) plane relative to the perpendicularly polarized. Specifically, one can write

$$s_{12}(\theta_s) = \frac{I_{//}(\theta_s) - I_{\perp}(\theta_s)}{I_{//}(\theta_s) + I_{\perp}(\theta_s)} \quad (6.1)$$

where  $I_{//}(\theta_s)$  is the scattered irradiance at  $\theta_s$  with horizontally polarized incident light and  $I_{\perp}(\theta_s)$  is the counterpart for the vertically polarized incident light. Based on the above relation, the measured data, shown as  $-s_{12}(\theta_s)$  in Fig. 4-6 and 4-14, can be interpreted that cells have stronger ability to scatter vertically polarized incident light than the horizontally polarized, which reaches a maximum as the scattering angle  $\theta_s$  approaches to about  $80^\circ$ . Moreover, a careful examination of the data in Fig. 4-6 indicates that the angle of maximum  $-s_{12}$ ,  $\theta_{sm}$ , shifts toward larger values as  $\lambda$  decreases. Even though the  $\theta_{sm}$  shift is relatively small, it is large enough to exhibit a strong correlation with wavelength. In addition, we find that the peak value of the element  $-s_{12}$  decreases with increasing wavelength for both cell suspensions.

To investigate the wavelength dependence of the peak value and  $\theta_{sm}$  in  $-s_{12}(\theta_s)$ , we employed two different modeling techniques. The accurate method of FDTD provides a characteristic Gaussian shaped pattern in  $-s_{12}(\theta_s)$  by modeling just a single B-cell as the scatterer (Fig. 6-1). By contrast, the coated sphere model, even using the same set of the mean values of refractive indices and radii and averaged over a fairly large ranges of radii, still deviate significantly from the measured shapes of  $-s_{12}(\theta_s)$  and  $-s_{34}(\theta_s)$  (Fig. 6-2). This fact suggests strongly that the nonspherical features of the biological cells (even in

the case of B-cells) play a vital role in determining the angular distribution of the Mueller matrix elements (Brock, Hu et al. 2006). We also observe that both the FDTD and coated sphere models correctly predict a decreasing  $\theta_{sm}$  with increasing  $\lambda$  as demonstrated by the experimental data although at angles different from the measured values. Combined together, these results yield a conclusion that accurate modeling with realistic cell morphology has the capacity to extract the intracellular distribution of refractive index from the experimental data of angle-resolved Mueller matrix elements. Currently, the computing complexity of the FDTD method is the major roadblock to our efforts to study the index distributions in cells and their dispersion relations. Research is underway to adapt efficient modeling methods to model the light scattering by cells. Also, the signal intensity for HL-60 cells at 850nm is unusually small compared to those at the other two wavelengths which need be investigated in our future research.

The matrix element  $S_{34}$  has been suspected to contain rich information about the size (Perry 1978; Bickel and Stafford 1981; Bohren and Huffman 1983; Menguc and Manickavasagam 1998) and internal structure of the scatterers (Bickel and Stafford 1981; Witkowski, Krol et al. 1998). The element  $S_{34}$  relates  $45^\circ$  linear polarization ( $U_t$ ) of the scattered field to circular polarization ( $V_i$ ) of incident field with matrix multiplication (see Eq. 2.8). The  $S_{34}$  signal is close to zero for scatterers with small size parameters and becomes nonzero and oscillates with  $\theta_s$  as the scatterers increase in size (Bickel and Stafford 1981; Menguc and Manickavasagam 1998). Its sensitivity to the subtle change in the biological samples such as live cells makes it more useful and volatile and it may be the best matrix element for sizing scatterers (Perry 1978). Also, the element  $S_{34}$  can be

applied to investigate the effect of the environment change on the biological cells (Bickel and Stafford 1981; Witkowski, Krol et al. 1998). However, with its wealth information, the accuracy of  $S_{34}$  investigation is affected by its relatively small signal magnitude compared to other elements (Bohren and Huffman 1983; Menguc and Manickavasagam 1998).

Our measured data for B-cells, shown as  $-s_{34}(\theta_s)$  in Fig. 4-11, demonstrates part of the characterizations as the discussion above. The signal magnitude of  $-s_{34}(\theta_s)$  is smaller compared with other elements. The drastic change of the measured shape at 862nm is due to the decreased level of scattered light at longer wavelength (or equivalently, smaller size parameter). We also attribute the small signals for HL-60 cells to their smaller size compared to that of B-cells. More attention in our future research need be brought to  $s_{34}$  because of its sensitivity to the difference on the cellular scale.

## **6.2 Light Scattering in Turbid and Skin Samples**

The measurement of coherent reflectance was validated by confirming the dominance of the coherent reflection over the diffused one at the specular reflection angle for both the epidermis and dermis sides of the skin samples, as shown in Fig. 5-2. Diffuse reflection occurs in a large angular range in comparison to the specular reflection angle defined by the aperture of the photodiode PD2 (see Fig. 3-10) and decreases towards the baseline data of water as the incident angle  $\theta$  approaches to  $80^\circ$ . The diffusely reflected light originates from two sources: the rough tissue surface mismatched optically with the prism glass and the light scattering in the tissue bulk. Combining the fact that the index

mismatch between the tissue sample and the BK7 glass of the prism for the epidermis is smaller than that of the dermis with the knowledge of the skin epidermis having larger scattering coefficient than the dermis (van Gemert, Jacques et al. 1989), one can conclude that the diffuse reflection of the skin tissues should be dominated by the bulk scattering.

The skin tissue has a layered structure with two primary layers of epidermis and dermis, both are beneath the superficial layer of the epidermis or the stratum corneum (sc). We examined the human tissue structures by preparing histological slides of the skin tissue samples from 4 patients (with ID # from 8 to 11, see Table 5-1) with standard H&E staining. Two examples of skin slides were shown in Fig. 5-9 with one from a Caucasian and the other from an African American patient. It can be seen that the sc layer is less than  $10\mu\text{m}$  in thickness, as expected, with the thickness of epidermis ranging from about 30 to  $80\mu\text{m}$ . We further verified that the sc layer had no significant effect on the refractive index determination by comparing the index values from samples with and without the sc layer prepared from fresh porcine skin tissues. The real refractive index  $n_r$  of the epidermis at the wavelengths of 442nm and 1064nm was found to be the same within the experimental errors between the samples with and without the sc layer. These results demonstrated that the sc layer has no significant effect on the real refractive index of the skin epidermis because of its small thickness in comparison with the penetration depth (Everett, Yeagers et al. 1966; van Gemert, Jacques et al. 1989).

A general model of refractive index for a dense and turbid medium remains an open question. But according to the existing models of effective medium for absorbing or

dilute turbid media (Ballenegger and Weber 1999; Barrera and Garcia-Valenzuela 2003) the refractive index determined from a coherent reflectance curve should relate to at least the full penetration depth of the coherent component of the incident wave in the medium. The total attenuation coefficients, as the sum of the scattering and absorption coefficients, for both the skin epidermis and dermis are expected to be on the orders of 1 to 10 mm<sup>-1</sup> based on the published data (van Gemert, Jacques et al. 1989; Ma, Lu et al. 2005) in the spectral region from 300 to 1600nm. Consequently, the penetration depth for the coherent component should be about a few hundred micrometers or less. Therefore, one would expect the tissue response of the first 100µm layer to dominate the coherent reflectance and thus the value of the real refractive index. This conclusion is supported by the wavelength correlation of the real refractive index determined from the epidermis and dermis sides of the skin tissue samples. The correlation coefficient of wavelength dependence of the real refractive index was found to be  $r_{\text{corr}} = 0.99$  between the index determined with s- and p-polarized beam for the epidermis and  $r_{\text{corr}} = 0.95$  for the dermis. The values of  $r_{\text{corr}}$  decreased drastically to 0.057 and 0.065 between the index of epidermis and dermis measured with the s- and p-polarized beam, respectively.

To extend the use of our real refractive index data on the limited number of wavelengths, we have tested different dispersion schemes based on the equations by Cauchy, Cornu and Conrady. From Figs. 5-17 and 5-18, it is clear that these relations are close to each other and all fit to data fairly well for the dermis and very well for the epidermis. Therefore, these equations may be used to estimate the values of the real refractive indices of human skin tissues with the coefficients given in Table 5-2 between

300 to 1600nm. These estimations should be further improved as the refractive index becomes available at an increased number of wavelengths.

### **6.3 Summary**

In this dissertation, the refractive indices have been studied on the cellular and tissue levels. The sixteen Mueller matrix elements were fully determined for human B-cell and HL-60 cell suspensions at 442, 633 and 850nm (or 862nm) with our PEM based goniometer system. The correlation between the Mueller matrix elements and intracellular distribution of refractive index was discussed using different models of light scattering by cells. In addition, the refractive indices for turbid samples and skin tissues were obtained as a function of wavelength from 325 nm to 1550nm. Different dispersion schemes were tested and provided an estimate on the values of the real refractive indices of human skin tissues at this spectral region. In the future research, the goniometer system can be further improved to reduce stepping error and increase scanning speed. More attention need be paid to the identification and study of Mueller matrix elements that have rich information about the scatterers. Fast and efficient modeling method is desirable to further improve comparison with experimental data on different cells and at short wavelengths in the near future. Even though these studies were limited currently by the simulation speed of the FDTD method in modeling, we accomplished the goal by demonstrating the close correlation between cell morphology and light scattering signals.

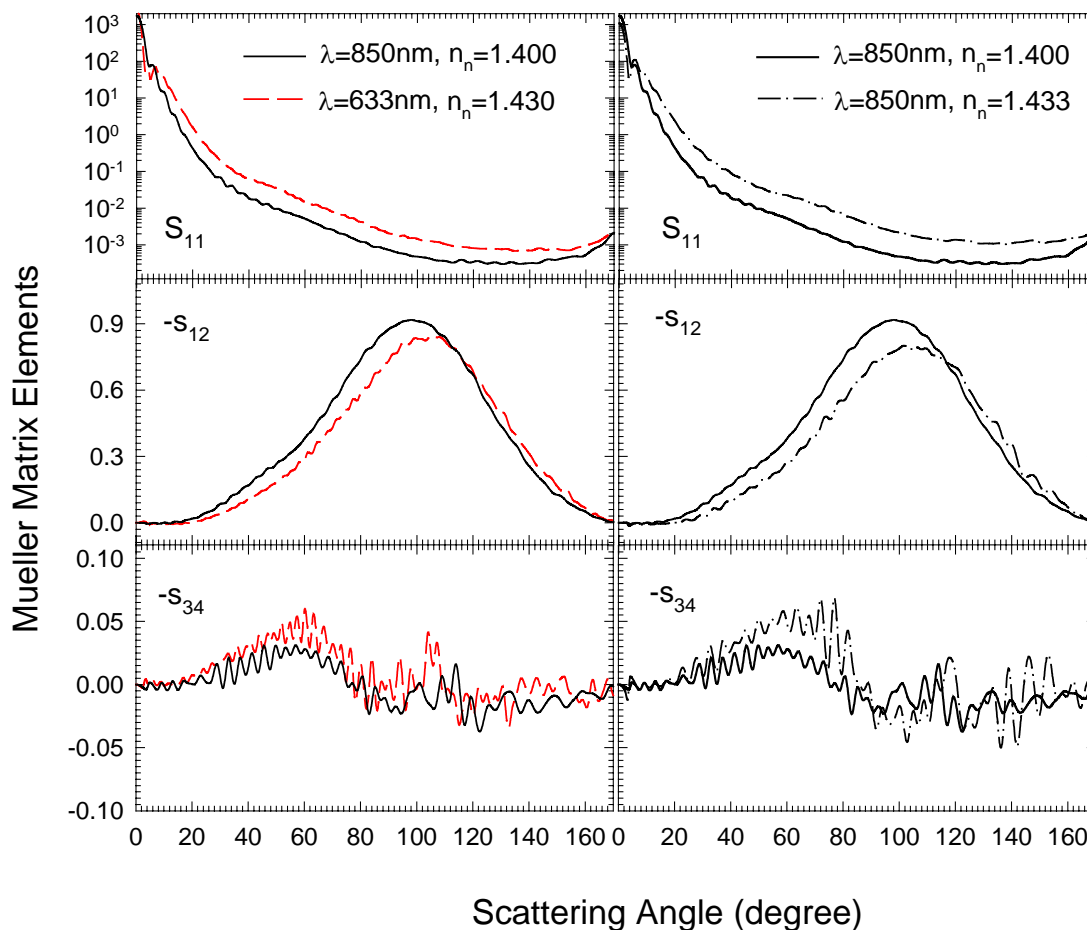


Figure 6-1 The angle-resolved Mueller matrix elements of  $S_{11}$ ,  $-S_{12}$  and  $-S_{34}$  calculated by the FDTD method for B-cell of 3D structures reconstructed from its confocal images with refractive indices set at  $n_h=1.336$  for the host medium,  $n_c=1.380$  for the cytoplasm and  $n_n=1.430$  for the nucleus at  $\lambda=633\text{nm}$  and  $n_h=1.330$ ,  $n_c=1.368$  and  $n_n=1.400$  or  $1.433$  at  $\lambda=850\text{nm}$ . The calculated elements are the averaged values over 12 orientations.

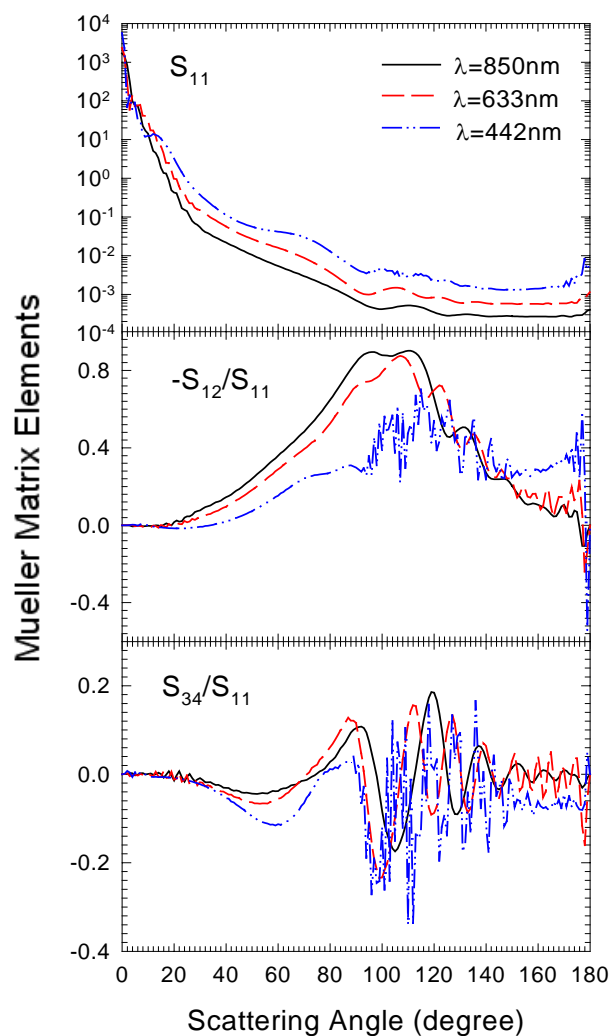


Figure 6-2 The angle-resolved Mueller matrix elements of  $S_{11}$ ,  $-S_{12}$  and  $-S_{34}$  calculated by a coated sphere model with the mean inner radius  $r_n=4.143\mu\text{m}$  and outer radius  $r_c=5.133\mu\text{m}$ . The mean values of the refractive indices were assigned as:  $n_h=1.342$ ,  $n_c=1.400$  and  $n_n=1.460$  at  $\lambda=442\text{nm}$ ;  $n_h=1.336$ ,  $n_c=1.380$  and  $n_n=1.430$  at  $\lambda=633\text{nm}$ ;  $n_h=1.330$ ,  $n_c=1.368$  and  $n_n=1.400$  at  $\lambda=850\text{nm}$ . The elements are the values averaged over the coated spheres of Gaussian distributions with  $\pm 20\%$  on  $r_n$  and  $r_c$  and  $\pm 3.6\%$  on  $n_h$  and  $\pm 0.8\%$  on  $n_c$ .

## Bibliography

Abhyanka.Kd and A. L. Fymat (1969). "Relations between Elements of Phase Matrix for Scattering." Journal of Mathematical Physics **10**(10): 1935-&.

Anderson, R. R. and J. A. Parrish (1981). "The optics of human skin." J Invest Dermatol **77**(1): 13-9.

Antosiewicz, H. A. (1964). "Bessel functions of fractional order." Handbook of Mathematical Functions: 435-478.

Atchison, D. A. and G. Smith (2005). "Chromatic dispersions of the ocular media of human eyes." J Opt Soc Am A Opt Image Sci Vis **22**(1): 29-37.

Ballenegger, V. C. and T. A. Weber (1999). "The Ewald-Oseen extinction theorem and extinction lengths." Am J Phys **67**(7): 599-605.

Barrera, R. G. and A. Garcia-Valenzuela (2003). "Coherent reflectance in a system of random Mie scatterers and its relation to the effective-medium approach." J Opt Soc Am A Opt Image Sci Vis **20**(2): 296-311.

Bickel, W. S., J. F. Davidson, et al. (1976). "Application of polarization effects in light scattering: A new biophysical tool." Proc. Nat. Acad. Sci. USA **73**: 486-490.

Bickel, W. S. and M. E. Stafford (1981). "Polarized light scattering from biological systems: a technique for cell differentiation." J. Biol. Phys. **9**: 53-66.

Birnie, G. D. (1988). "The HI60 Cell-Line - a Model System for Studying Human Myeloid Cell-Differentiation." British Journal of Cancer **58**: 41-45.

Bohren, C. F. and D. P. Gilra (1979). "Extinction by a Spherical-Particle in an Absorbing Medium." Journal of Colloid and Interface Science **72**(2): 215-221.

Bohren, C. F. and D. R. Huffman (1983). Absorption and scattering of light by small particles. New York, Wiley.

Brock, R. S., X. H. Hu, et al. (2006). "Effect of Detailed Cell Structure on Light Scattering Distribution: FDTD study of a B-cell with 3D Structure Constructed from Confocal Images." J. Quant. Spectrosc. Radiat. Transfer **102**: 25-36.

- Brock, R. S., X. H. Hu, et al. (2005). "Evaluation of a parallel FDTD code and application to modeling of light scattering by deformed red blood cells." Opt. Express **13**(14): 5279-5292.
- Brock, R. S., X. H. Hu, et al. (2005). "Simulation of light scattering by a pressure deformed red blood cell with a parallel FDTD method." SPIE Proceedings **5702**: 69-75.
- Bruggeman, D (1935). Ann. Phys Leipzig **24**: 636.
- Brunsting, A. and P. Mullaney (1974). "Differential light scattering from spherical mammalian cells." Biophys J **14**: 439-453.
- Chandrasekhar, S. (1960). Radiative Transfer. New York, Dover Publications.
- Dalton, W. T., M. J. Ahearn, et al. (1988). "HI-60 Cell-Line Was Derived from a Patient with Fab-M2 and Not Fab-M3." Blood **71**(1): 242-247.
- Dunn, A. and R. Richard-Kortum (1996). "Three-dimensional computation of light scattering from cells." IEEE J. Selected Topics Quantum. Electron. **2**: 898-890.
- Dunn, A., C. Smithpeter, et al. (1997). "Finite-Difference Time-Domain Simulation of Light Scattering from Single Cells." J. Biomed. Opt. **2**(3): 262-266.
- Eisenber.H (1965). "Equation for Refractive Index of Water." Journal of Chemical Physics **43**(11): 3887-&.
- Everett, M. A., E. Yeagers, et al. (1966). "Penetration of epidermis by ultraviolet rays." Photochem Photobiol **5**(7): 533-42.
- Flock, S. T., S. L. Jacques, et al. (1992). "Optical properties of Intralipid: a phantom medium for light propagation studies." Lasers Surg. Med. **12**(5): 510-9.
- Hale, G. and M. Querry (1973). "Optical constants of water in the 200nm to 200 micrometer wavelength region." Appl. Opt. **12**: 555-563.
- Hunt, A. J. and D. R. Huffman (1973). "A new polarization-modulated light scattering instrument." Rev. Sci. Instrum. **44**(12): 1753-1762.
- Hurwitz, H. R., J. Hozier, et al. (1979). "Characterization of a leukemic cell line of the pre-B phenotype." Int. J. Cancer **23**: 174-180.
- Jackson, J. D. (1975). Classical electrodynamics. New York, Wiley.
- Jackson, J. D. (1999). Classical electrodynamics. New York, Wiley: Ch. 10.

- J.W. Hovenier (1994). "Structure of a general pure Mueller matrix". *Applied Optics* **33**(36): 8318-8324.
- Kang, S. N., M. H. Lee, et al. (2001). "Induction of human promyelocytic leukemia HL-60 cell differentiation into monocytes by silibinin: involvement of protein kinase C." *Biochemical Pharmacology* **61**(12): 1487-1495.
- Knuttel, A. and M. Boehlau-Godau (2000). "Spatially confined and temporally resolved refractive index and scattering evaluation in human skin performed with optical coherence tomography." *J Biomed Opt* **5**(1): 83-92.
- Kroger, R. H. H. (1992). "Methods to estimate dispersion in vertebrate ocular media." *J Opt Soc Am A Opt Image Sci Vis* **9**(9): 1486-1490.
- Kuik, F., P. Stammes, et al. (1991). "Experimental determination of scattering matrices of water droplets and quartz particles." *Appl. Opt.* **30**(33): 4872-4881.
- Kurtz, S. S., Wikings.Ae, et al. (1965). "Refractive Index and Density of Acetone-Water Solutions." *Journal of Chemical and Engineering Data* **10**(4): 330-&.
- Lavker, R. M., G. Dong, et al. (1991). "Hairless micropig skin. A novel model for studies of cutaneous biology." *Am J Pathol* **138**(3): 687-97.
- Lu, J. Q., P. Yang, et al. (2005). "Simulations of Light Scattering from a Biconcave Red Blood Cell Using the FDTD method." *J. Biomed. Opt.* **10**(2): 024022.
- Ma, X., J. Q. Lu, et al. (2003). "Determination of Complex Refractive Index of Polystyrene Microspheres from 370 to 1610nm." *Phys. Med. Biol.* **48**: 4165-4172.
- Ma, X., J. Q. Lu, et al. (2005). "Bulk optical parameters of porcine skin dermis tissues at eight wavelengths from 325 to 1557nm." *Opt. Lett.* **30**: 412-414.
- Marquardt, D. W. (1963). "An Algorithm for Least Squares Estimation of Parameters." *Journal of the Society of Industrial and Applied Mathematics* **11**(2): 431-441.
- Meeten, G. H. and A. N. North (1995). "Refractive index measurement of absorbing and turbid fluids by reflection near the critical angle." *Meas. Sci. Technol.* **6**: 214-221.
- Menguc, M. P. and S. Manickavasagam (1998). "Characterization of size and structure of agglomerates and inhomogeneous particles via polarized light." *International Journal of Engineering Science* **36**(12-14): 1569-1593.
- Michael I. Mishchenko, J. W. H., Larry D. Travis (2000). "Light Scattering by Nonspherical Particles."

- Mie, G. (1908). "Beitrage zur Optik truber Medien, speziell kolloidaler Metallosungen." Annalen der Physik **25**(3): 377-445.
- Mourant, J. R., M. Canpolat, et al. (2000). "Light scattering from cells: the contribution of the nucleus and the effects of proliferative status." J Biomed Opt **5**(2): 131-7.
- Mourant, J. R., J. P. Freyer, et al. (1998). "Mechanisms of light scattering from biological cells relevant to noninvasive optical-tissue diagnostics." Appl Opt **37**(16): 3586-3593.
- Niklasson, G. A., C. G. Granqvist, et al. (1981). "Effective Medium Models for the Optical-Properties of Inhomogeneous Materials." Applied Optics **20**(1): 26-30.
- Ossenkopf, V. (1991). "Effective-Medium Theories for Cosmic Dust Grains." Astronomy and Astrophysics **251**(1): 210-219.
- Parker, D. C. (1993). "T cell-dependent B cell activation." Annu Rev Immunol **11**: 331-60.
- Perrin, J. M. and P. L. Lamy (1990). "On the Validity of Effective-Medium Theories in the Case of Light Extinction by Inhomogeneous Dust Particles." Astrophysical Journal **364**(1): 146-151.
- Perry, A. J. H., and Donald R. Huffman (1978). "Experimental determinations of Mueller scattering matrices for nonspherical particles." Applied Optics **17**(17): 2700-2710.
- Pettit, G. H. and M. N. Ediger (1996). "Corneal-tissue absorption coefficients for 193- and 213-nm ultraviolet radiation." Appl Opt **35**(19): 3386-3391.
- Salzman, G. C., J. M. Crowell, et al. (1975). "Cell classification by laser light scattering: identification and separation of unstained leukocytes." Acta Cytol **19**(4): 374-7.
- Stroud E., F. P. P. (1978). "Self-consistent approach to electromagnetic wave propagation in composite media: Application to model granular metals." Phys. Rev.B **17**: 1602-1610.
- Taflove, A. and S. C. Hagness (2000). Computational Electrodynamics: The Finite-Difference Time-Domain Method. Boston, Mass., Artech House.
- Tearney, G. J., M. E. Brezinski, et al. (1995). "Determination of the refractive index of highly scattering human tissue by optical coherence tomography." Opt Lett **20**(21): 2258-2260.
- Turner, L. (1973). "Rayleigh-Gans-Born Light Scattering by Ensembles of Randomly Oriented Anisotropic Particles." Appl. Opt. **12**(5): 1085-1090.

van Gemert, M. J., S. L. Jacques, et al. (1989). "Skin optics." IEEE Trans. Biomed. Eng. **36**(12): 1146-54.

Volten, H., J. F. de Haan, et al. (1998). "Laboratory Measurements of Angular Distributions of Light Scattered by Phytoplankton and Silt." Lum. Oceanogr. **43**(6): 1180-1197.

Wang, A. M., A. A. Creasey, et al. (1985). "Molecular-Cloning of the Complementary-DNA for Human-Tumor Necrosis Factor." Science **228**(4696): 149-154.

Wang, X., C. Zhang, et al. (2002). "Simultaneous refractive index and thickness measurements of bio tissue by optical coherence tomography." J Biomed Opt **7**(4): 628-32.

Witkowski, K., T. Krol, et al. (1998). "A light-scattering matrix for unicellular marine phytoplankton." Limnology and Oceanography **43**(5): 859-869.

Wyatt, P. J. and D. T. Phillips (1972). "Structure of single bacteria from light scattering." J. Theor. Biol. **37**(3): 493-501.

Yang, P. and K. N. Liou (1996). "Finite-difference time domain method for light scattering by small ice crystals in three-dimensional space." J. Opt. Soc. Amer., A **13**: 2072-2085.

Yee, S. K. (1966). "Numerical solutions of initial boundary problems involving Maxwell's equations in isotropic materials." IEEE Trans. Antennas. Propg. **14**: 302-307.

Zharinov, A., P. Tarasov, et al. (2006). "A study of light scattering of mononuclear blood cells with scanning flow cytometry." JQSRT **102**(1): 121-128.

Zuev, V. E. and V. K. Sonchik (1969). "Experimental Determination of Components of Water Complex Refractive Index for Visual and Infrared." Izvestiya Akademii Nauk Sssr Fizika Atmosfery I Okeana **5**(7): 745-&.

## Appendix

### A. Derivations of the Mueller Matrix for Different Optical Devices

#### 1) The Mueller Matrix for a Polarizer $P(\gamma)$ :

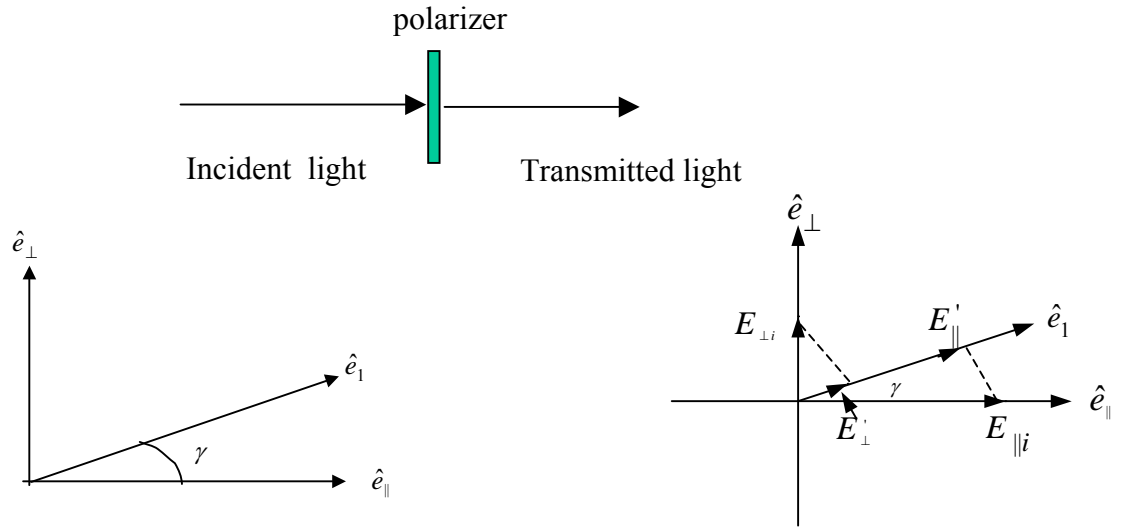


Figure A-1 Specification of the field components(  $\hat{e}_1$  specifies the axes of the modulator)

Assume  $\gamma$  is the angle between the unit vector ( $\hat{e}_1$ ) and the axis of the polarizer

$\hat{e}_1$ , as shown above, the total transmitted field along  $\hat{e}_1$  is given by:

$$E' = E'_{\parallel} + E'_{\perp} = E_{\parallel i} \cos \gamma + E_{\perp i} \sin \gamma . \quad (\text{A.1})$$

So the relations between the incident field components ( $E_{\parallel i}, E_{\perp i}$ ) and transmitted field

components ( $E_{\parallel t}, E_{\perp t}$ ) are

$$\begin{aligned} E_{\parallel t} &= E' \cos \gamma = E_{\parallel i} \cos^2 \gamma + E_{\perp i} \sin \gamma \cos \gamma ; \\ E_{\perp t} &= E' \sin \gamma = E_{\parallel i} \cos \gamma \sin \gamma + E_{\perp i} \sin^2 \gamma ; \end{aligned} \quad (\text{A.2})$$

Or

$$\begin{pmatrix} E_{\parallel t} \\ E_{\perp t} \end{pmatrix} = \begin{pmatrix} \cos^2 \gamma & \sin \gamma \cos \gamma \\ \sin \gamma \cos \gamma & \sin^2 \gamma \end{pmatrix} \begin{pmatrix} E_{\parallel i} \\ E_{\perp i} \end{pmatrix}. \quad (\text{A.3})$$

In the equation above, the 2x2 matrix is the J-matrix previously discussed:

$$\begin{pmatrix} J_1 & J_4 \\ J_3 & J_2 \end{pmatrix} = \begin{pmatrix} \cos^2 \gamma & \sin \gamma \cos \gamma \\ \sin \gamma \cos \gamma & \sin^2 \gamma \end{pmatrix}. \quad (\text{A.4})$$

The Mueller matrix for a nonabsorbing linear polarizer is obtained by plugging Eq. (A.4) into Eq. (2.19):

$$P(\gamma) = \frac{1}{2} \begin{pmatrix} 1 & \cos 2\gamma & \sin 2\gamma & 0 \\ \cos 2\gamma & \cos^2 2\gamma & \cos 2\gamma \sin 2\gamma & 0 \\ \sin 2\gamma & \sin 2\gamma \cos 2\gamma & \sin^2 2\gamma & 0 \\ 0 & 0 & 0 & 0 \end{pmatrix}. \quad (\text{A.5})$$

## 2). The Mueller Matrix for the Photoelastic Modulator $M(\gamma)$

The photo elastic modulator (PEM) is a variable wave-plate in which the phase difference between the two components of transmitted light, parallel and perpendicular to the optical axis of the PEM, can be made to vary as a sine function of time at a constant frequency. The relation between the incident electric field ( $E_i$ ) and the transmitted electric field ( $E_t$ ) can be found from the following derivation.

Again, we start our discussion from the electric fields incident on and transmitting through the modulator. As an ideal retarder, it also introduces a phase difference  $\phi_1 - \phi_2$ .

Transmitted components along  $\hat{e}_1$  are:

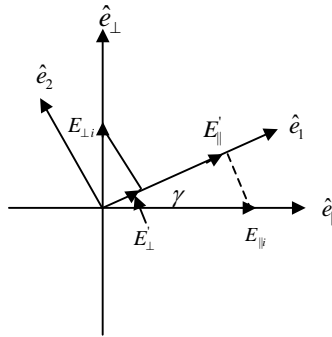


Figure A-2 Light through a modulator

$$\begin{aligned} E'_{\parallel} &= E_{\parallel i} \cos \gamma e^{i\phi} \\ E'_{\perp} &= E_{\perp i} \sin \gamma e^{i\phi} \end{aligned} \quad (\text{A.6})$$

Transmitted components along  $\hat{e}_2$  are:

$$\begin{aligned} E'_{2\parallel} &= -E_{\parallel i} \sin \gamma e^{i\phi_2} \\ E'_{2\perp} &= E_{\perp i} \cos \gamma e^{i\phi_2} \end{aligned} \quad (\text{A.7})$$

where  $\phi_1$  and  $\phi_2$  are related to the different light speed for  $\hat{e}_1$ ,  $\hat{e}_2$ , respectively. Therefore, we obtain the total field of the transmitted light on the  $\hat{e}_1$  axis of modulator as:

$$E'_1 = E'_{\parallel} + E'_{1\perp} = E_{\parallel i} \cos \gamma e^{i\phi} + E_{\perp i} \sin \gamma e^{i\phi}; \quad (\text{A.8})$$

and on the  $\hat{e}_2$  axis:

$$E'_2 = E'_{2\parallel} + E'_{2\perp} = -E_{\parallel i} \sin \gamma e^{i\phi_2} + E_{\perp i} \cos \gamma e^{i\phi_2}. \quad (\text{A.9})$$

Project back to the original axes of  $\hat{e}_{\parallel}$  and  $\hat{e}_{\perp}$ :

$$\begin{aligned} E_{\parallel t} &= (e^{i\phi} \cos^2 \gamma + e^{i\phi_2} \sin^2 \gamma) E_{\parallel i} + (e^{i\phi} \cos \gamma \sin \gamma - e^{i\phi_2} \cos \gamma \sin \gamma) E_{\perp i} \\ E_{\perp t} &= (e^{i\phi} \cos \gamma \sin \gamma - e^{i\phi_2} \cos \gamma \sin \gamma) E_{\parallel i} + (e^{i\phi_2} \cos^2 \gamma + e^{i\phi} \sin^2 \gamma) E_{\perp i} \end{aligned} \quad (\text{A.10})$$

The above equations can be written in the matrix form as:

$$\begin{pmatrix} E_{\parallel r} \\ E_{\perp r} \end{pmatrix} = \begin{pmatrix} e^{i\phi_1} \cos^2 \gamma + e^{i\phi_2} \sin^2 \gamma & e^{i\phi_1} \cos \gamma \sin \gamma - e^{i\phi_2} \cos \gamma \sin \gamma \\ e^{i\phi_1} \cos \gamma \sin \gamma - e^{i\phi_2} \cos \gamma \sin \gamma & e^{i\phi_2} \cos^2 \gamma + e^{i\phi_1} \sin^2 \gamma \end{pmatrix} \begin{pmatrix} E_{\parallel i} \\ E_{\perp i} \end{pmatrix}. \quad (\text{A.11})$$

this yields:

$$\begin{aligned} J_1 &= e^{i\phi_1} \cos^2 \gamma + e^{i\phi_2} \sin^2 \gamma \\ J_2 &= e^{i\phi_2} \cos^2 \gamma + e^{i\phi_1} \sin^2 \gamma \\ J_3 &= e^{i\phi_1} \cos \gamma \sin \gamma - e^{i\phi_2} \cos \gamma \sin \gamma \\ J_4 &= e^{i\phi_1} \cos \gamma \sin \gamma - e^{i\phi_2} \cos \gamma \sin \gamma \end{aligned} \quad (\text{A.12})$$

Substituting Eq. (A.12) into Eq. (2.19) gives the Mueller matrix for the modulator as:

$$M(\gamma) = \begin{pmatrix} 1 & 0 & 0 & 0 \\ 0 & \cos^2 2\gamma + \sin^2 2\gamma \cos \phi & \sin 2\gamma \cos 2\gamma (1 - \cos \phi) & -\sin 2\gamma \sin \phi \\ 0 & \sin 2\gamma \cos 2\gamma (1 - \cos \phi) & \sin^2 2\gamma + \cos^2 2\gamma \cos \phi & \cos 2\gamma \sin \phi \\ 0 & \sin 2\gamma \sin \phi & -\cos 2\gamma \sin \phi & \cos \phi \end{pmatrix}. \quad (\text{A.13})$$

where  $\phi = \phi_1 - \phi_2$  is related to the birefringence of the PEM.

If one introduces a sinusoidal modulation in the phase difference, then:

$$\phi = \phi_0 \sin \omega t \quad (\text{A.14})$$

where  $\omega$  is the frequency of the modulator vibration.

### 3). The Mueller Matrix for a Quarter-wave Plate

The phase difference  $\phi$  is a constant and equal to  $90^\circ$  for a quarter wave plate, and it is straightforward to obtain the Mueller matrix by substituting  $\phi=90^\circ$  into Eq. (A.14):

$$Q(\gamma) = \begin{pmatrix} 1 & 0 & 0 & 0 \\ 0 & \cos^2 2\gamma & \sin 2\gamma \cos 2\gamma & -\sin 2\gamma \\ 0 & \sin 2\gamma \cos 2\gamma & \sin^2 2\gamma & \cos 2\gamma \\ 0 & \sin 2\gamma & -\cos 2\gamma & 0 \end{pmatrix}. \quad (\text{A.15})$$

## B. Mie Theory For Nonabsorptive Host Medium

In this section we briefly review the Mie theory for the purpose to derive the Mueller matrix elements for simple sphere and the detailed procedures can be found in (Bohren and Huffman 1983; Ma 2004). The Mie theory provides one of the analytical solutions of the light scattering problems for a spherical particle embedded in a host medium. An accurate model of light distribution in microsphere suspensions can be established which are often used as tissue phantoms for calibrating optical instruments and investigating cell and tissue optics by combining Mie theory and the Monte Carlo simulations (Ma, Lu et al. 2005).

An electromagnetic wave  $(\vec{E}, \vec{H})$  propagating in a homogeneous medium must satisfy the following two wave equations:

$$\begin{aligned}\nabla^2 \vec{E} + k^2 \vec{E} &= 0 \\ \nabla^2 \vec{H} + k^2 \vec{H} &= 0\end{aligned}\tag{B.1}$$

where  $k^2 = \omega^2 \epsilon \mu$  is the wave number,  $\omega$  is the angular frequency of the wave,  $\epsilon$  is the permittivity of the medium, and  $\mu$  is the permeability of the medium. And they are derived from the Maxwell's equations below for a monochromatic wave

$$\begin{aligned}\nabla \cdot \mathbf{D} &= 0 \\ \nabla \cdot \mathbf{B} &= 0 \\ \nabla \times \mathbf{E} &= -\frac{\partial \mathbf{B}}{\partial t} \\ \nabla \times \mathbf{B} &= \mu \epsilon \frac{\partial \mathbf{E}}{\partial t}\end{aligned}\tag{B.2}$$

where  $\mathbf{D}=\epsilon\mathbf{E}$ .

A scalar function  $\psi$  in a spherical polar coordinates  $(r,\theta,\phi)$  (Fig. B-1) is introduced to construct two vector functions by Mie (1908), and this method avoid the lengthy procedures to solve Eq. (B.1) directly,

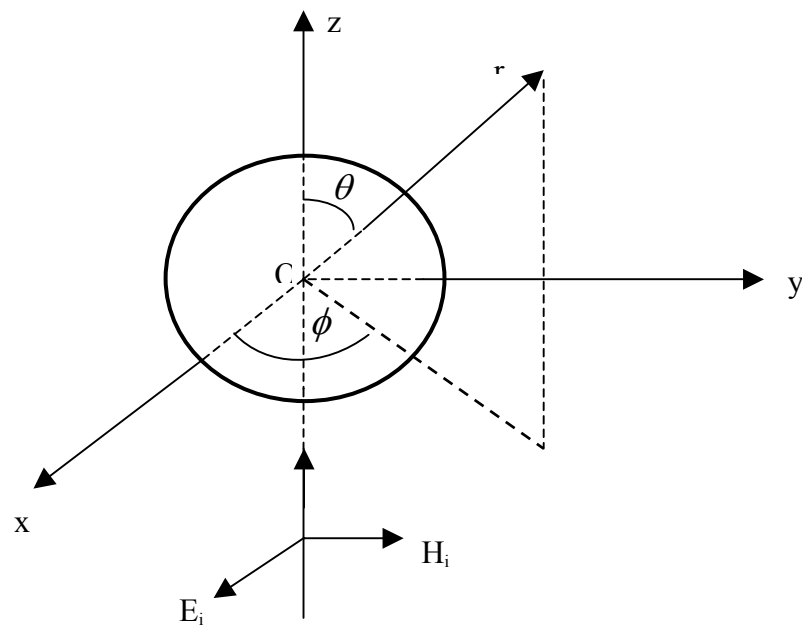


Figure B-1 Spherical polar coordinate system

$$\begin{aligned}\vec{\mathbf{M}} &= \nabla \times (\vec{\mathbf{r}}\psi) \\ \vec{\mathbf{N}} &= \frac{\nabla \times \vec{\mathbf{M}}}{k}\end{aligned}\tag{B.3}$$

where  $\vec{\mathbf{M}}$  and  $\vec{\mathbf{N}}$  have the properties:

$$\begin{aligned}
\nabla \cdot \vec{M} &= 0 \\
\nabla \cdot \vec{N} &= 0 \\
\nabla \times \vec{N} &= k\vec{M} \\
\nabla \times \vec{M} &= k\vec{N}
\end{aligned}
\tag{B.4}$$

The importance of this method is increased if  $\psi$  is a solution of a scalar wave equation in the spherical polar coordinates such as

$$\frac{1}{r} \frac{\partial}{\partial r} \left( r^2 \frac{\partial \psi}{\partial r} \right) + \frac{1}{r^2 \sin \theta} \frac{\partial}{\partial r} \left( \sin \theta \frac{\partial \psi}{\partial \theta} \right) + \frac{1}{r^2 \sin \theta} \frac{\partial^2 \psi}{\partial \phi^2} + k^2 \psi = 0
\tag{B.5}$$

then  $\vec{M}$  and  $\vec{N}$  will satisfy the vector wave equation:

$$\begin{aligned}
\nabla^2 \vec{M} + k^2 \vec{M} &= 0 \\
\nabla^2 \vec{N} + k^2 \vec{N} &= 0
\end{aligned}
\tag{B.6}$$

Obviously,  $\vec{M}$  and  $\vec{N}$  have all the required properties of an electromagnetic field. And it will be identical to find solutions for vector wave equations (B.1) and to find scalar solutions to the wave equation (B.5), but the mathematical complexity of the problem is drastically decreased.

Eq. (B.5) has the linearly independent solutions as (Bohren and Huffman 1983):

$$\Psi_{emn} = \cos(m\phi) P_n^m(\cos\theta) z_n(\rho);
\tag{B.7}$$

and

$$\Psi_{omn} = \sin(m\phi) P_n^m(\cos\theta) z_n(\rho)
\tag{B.8}$$

where  $\rho = kr$ , the subscripts e and o denote even and odd,  $P_n^m(\cos\theta)$  is the first kind associated Legendre function and  $z_n$  is any of the following four spherical Bessel functions  $j_n, y_n, h_n^{(1)}$  or  $h_n^{(2)}$ . Therefore, the vector spherical harmonics generated by  $\psi_{emn}$  and  $\psi_{omn}$  are

$$\begin{aligned}\vec{M}_{emn} &= \nabla \times (\vec{r}\psi_{emn}) \\ \vec{M}_{omn} &= \nabla \times (\vec{r}\psi_{omn}) \\ \vec{N}_{emn} &= \frac{\nabla \times \vec{M}_{emn}}{k} \\ \vec{N}_{omn} &= \frac{\nabla \times \vec{M}_{omn}}{k}\end{aligned}\quad (B.9)$$

which can be written in component form as:

$$\vec{M}_{emn} = \frac{-m}{\sin\theta} \sin(m\phi) P_n^m(\cos\theta) z_n(\rho) \hat{e}_\theta - \cos(m\phi) \frac{dP_n^m(\cos\theta)}{d\theta} z_n(\rho) \hat{e}_\phi, \quad (B.10)$$

$$\vec{M}_{omn} = \frac{m}{\sin\theta} \cos(m\phi) P_n^m(\cos\theta) z_n(\rho) \hat{e}_\theta - \sin(m\phi) \frac{dP_n^m(\cos\theta)}{d\theta} z_n(\rho) \hat{e}_\phi \quad (B.11)$$

$$\begin{aligned}\vec{N}_{emn} &= \frac{z_n(\rho)}{\rho} \cos(m\phi) n(n+1) P_n^m(\cos\theta) \hat{e}_r \\ &+ \cos(m\phi) \frac{dP_n^m(\cos\theta)}{d\theta} \frac{1}{\rho} \frac{d}{d\rho} [\rho z_n(\rho)] \hat{e}_\theta \\ &- m \sin(m\phi) \frac{P_n^m(\cos\theta)}{\sin\theta} \frac{1}{\rho} \frac{d}{d\rho} [\rho z_n(\rho)] \hat{e}_\phi\end{aligned}\quad (B.12)$$

$$\begin{aligned}
\vec{N}_{\text{omn}} = & \frac{z_n(\rho)}{\rho} \sin(m\phi) n(n+1) P_n^m(\cos\theta) \hat{e}_r \\
& + \sin(m\phi) \frac{dP_n^m(\cos\theta)}{d\theta} \frac{1}{\rho} \frac{d}{d\rho} [\rho z_n(\rho)] \hat{e}_\theta \\
& + m \cos m\phi \frac{P_n^m(\cos\theta)}{\sin\theta} \frac{1}{\rho} \frac{d}{d\rho} [\rho z_n(\rho)] \hat{e}_\phi
\end{aligned} \tag{B.13}$$

As mentioned at the start of this section, the functions  $\vec{M}_{\text{emn}}$ ,  $\vec{M}_{\text{omn}}$ ,  $\vec{N}_{\text{emn}}$ ,  $\vec{N}_{\text{omn}}$ , have all the required properties of an electromagnetic field, therefore, can be applied to express any electromagnetic fields in an expansion of an infinite series.

Consider that a plane wave with x-polarization propagating along z incident on a medium in which a homogeneous spherical particle with radius of  $R_a$  is embedded (Fig. B-1):

$$\vec{E}_i = E_0 e^{ikr \cos\theta} \hat{e}_x \tag{B.14}$$

where

$$\vec{e}_x = \sin\theta \cos\phi \hat{e}_r + \cos\theta \cos\phi \hat{e}_\theta - \sin\phi \hat{e}_\phi \tag{B.15}$$

The field for the incident wave can be expanded as

$$\vec{E}_i = E_0 \sum_{n=1}^{\infty} i^n \frac{2n+1}{n(n+1)} \left( \vec{M}_{\text{oln}}^{(1)} - i \vec{N}_{\text{eln}}^{(1)} \right) \tag{B.16}$$

$$\vec{H}_i = \frac{-k}{\omega\mu} E_0 \sum_{n=1}^{\infty} i^n \frac{2n+1}{n(n+1)} \left( \vec{M}_{\text{eln}}^{(1)} + i \vec{N}_{\text{oln}}^{(1)} \right) \tag{B.17}$$

where  $\mu$  is the permeability of the medium, the superscript (1) is appended to the vector spherical harmonics and is used to specify the radial dependence of the generating function by  $j_n$ .

Thus, the expansion of field inside the spherical particle  $(\vec{E}_1, \vec{H}_1)$  is

$$\vec{E}_1 = \sum_{n=1}^{\infty} E_n \left( c_n \vec{M}_{o1n}^{(1)} - i d_n \vec{N}_{e1n}^{(1)} \right) \quad (\text{B.18})$$

$$\vec{H}_1 = \frac{-k}{\omega \mu_1} \sum_{n=1}^{\infty} E_n \left( d_n \vec{M}_{e1n}^{(1)} + i c_n \vec{N}_{o1n}^{(1)} \right) \quad (\text{B.19})$$

where  $\mu_1$  is the permeability of the sphere. And the scattered field  $(\vec{E}_s, \vec{H}_s)$  can be expanded as (Bohren and Gilra 1979)

$$\vec{E}_s = \sum_{n=1}^{\infty} E_n \left( i a_n \vec{N}_{e1n}^{(3)} - b_n \vec{M}_{o1n}^{(3)} \right) \quad (\text{B.20})$$

$$\vec{H}_s = \frac{k}{\omega \mu} \sum_{n=1}^{\infty} E_n \left( i b_n \vec{N}_{o1n}^{(3)} + a_n \vec{M}_{e1n}^{(3)} \right) \quad (\text{B.21})$$

where the superscript (3) appended to vector spherical harmonics indicates that the radial dependence of the generating function is specified by  $h_n^{(1)}$ .

With the boundary conditions in component form (between the sphere and the surrounding medium  $r = R_a$ ):

$$\begin{aligned}
E_{i0} + E_{s0} &= E_{10} \\
E_{i\phi} + E_{s\phi} &= E_{1\phi} \\
H_{i0} + H_{s0} &= H_{10} \\
H_{i\phi} + H_{s\phi} &= H_{1\phi}
\end{aligned} \tag{B.22}$$

The scattering coefficients can be obtained from Eqs. (B.16-21) as:

$$a_n = \frac{\mu m^2 j_n(mx) [x j_n(x)]' - \mu_1 j_n(x) [mx j_n(mx)]'}{\mu m^2 j_n(mx) [x h_n^{(1)}(x)]' - \mu_1 h_n^{(1)}(x) [mx j_n(mx)]'} \tag{B.23}$$

$$b_n = \frac{\mu_1 j_n(mx) [x j_n(x)]' - \mu j_n(x) [mx j_n(mx)]'}{\mu_1 j_n(mx) [x h_n^{(1)}(x)]' - \mu h_n^{(1)}(x) [mx j_n(mx)]'} \tag{B.24}$$

and the coefficients of the field inside the particle:

$$c_n = \frac{\mu_1 j_n(mx) [x h_n^{(1)}(x)]' - \mu_1 h_n^{(1)}(x) [x j_n(x)]'}{\mu_1 j_n(mx) [x h_n^{(1)}(x)]' - \mu h_n^{(1)}(x) [mx j_n(mx)]'} \tag{B.25}$$

$$d_n = \frac{\mu_1 m j_n(x) [x h_n^{(1)}(x)]' - \mu_1 m h_n^{(1)}(x) [x j_n(x)]'}{\mu m^2 j_n(mx) [x h_n^{(1)}(x)]' - \mu_1 h_n^{(1)}(x) [mx j_n(mx)]'} \tag{B.26}$$

where the prime indicates differentiation with respect to the argument in the parentheses, the size parameter and the relative refractive index are

$$x = kR_a = \frac{2\pi n R_a}{\lambda}, \quad m = \frac{k_1}{k} = \frac{n_1}{n} \tag{B.27}$$

where  $n_1$  and  $n$  are the refractive indices of particle and medium, respectively.

The scattering coefficient can be simplified by introducing the Riccati-Bessel functions:

$$\begin{aligned}\psi_n(\rho) &= \rho j_n(\rho) \\ \xi_n(\rho) &= \rho h_n^{(1)}(\rho)\end{aligned}\tag{B.28}$$

therefore, if we define the permeability of the particle  $\mu_1$  and the surrounding medium  $\mu$  are same, the scattering coefficients (B.23) and (B.24) will have the forms

$$a_n = \frac{m\psi_n(mx)\psi_n'(x) - \psi_n(x)\psi_n'(mx)}{m\psi_n(mx)\xi_n'(x) - \xi_n(x)\psi_n'(mx)}\tag{B.29}$$

$$b_n = \frac{\psi_n(mx)\psi_n'(x) - m\psi_n(x)\psi_n'(mx)}{\psi_n(mx)\xi_n'(x) - m\xi_n(x)\psi_n'(mx)}\tag{B.30}$$

For the case that the incident light is x-polarized. From Eq. (B.20) to (B.26), the incident field can be written in the component form as

$$E_{i0} = \frac{\cos\phi}{\rho} \sum_{n=1}^{\infty} E_n (\psi_n \pi_n - i\psi_n' \tau_n)\tag{B.31}$$

$$E_{i\phi} = \frac{\sin\phi}{\rho} \sum_{n=1}^{\infty} E_n (\psi_n' \pi_n - \psi_n \tau_n)\tag{B.32}$$

$$H_{i0} = \frac{k}{\omega\mu} \tan\phi E_{i0}\tag{B.33}$$

$$H_{i\phi} = \frac{-k}{\omega\mu} \cotan\phi E_{i\phi}\tag{B.34}$$

where functions  $\pi_n$  and  $\tau_n$  are angle-dependent functions and defined as (Bohren and Gilra 1979)

$$\pi_n = \frac{P_n^1(\cos\theta)}{\sin\theta}\tag{B.35}$$

$$\tau_n = \frac{dP_n^1(\cos\theta)}{d\theta} \quad (\text{B.36})$$

The corresponding scattered field has the following form

$$E_{s\theta} = \frac{\cos\phi}{\rho} \sum_{n=1}^{\infty} E_n (ia_n \xi'_n \tau_n - b_n \xi_n \pi_n) \quad (\text{B.37})$$

$$E_{s\theta} = \frac{\sin\phi}{\rho} \sum_{n=1}^{\infty} E_n (b_n \xi_n \tau_n - ia_n \xi'_n \pi_n) \quad (\text{B.38})$$

$$H_{s\theta} = \frac{k}{\omega\mu} \frac{\sin\phi}{\rho} \sum_{n=1}^{\infty} E_n (ib_n \xi'_n \tau_n - a_n \xi_n \pi_n) \quad (\text{B.39})$$

$$H_{s\theta} = \frac{k}{\omega\mu} \frac{\cos\phi}{\rho} \sum_{n=1}^{\infty} E_n (ib_n \xi'_n \pi_n - a_n \xi_n \tau_n) \quad (\text{B.40})$$

### C. Data Acquisition and Programs

- 1). Goniometer system control and data collection (see Appendix D)

Program Names: 040913\_goniometer\_2lock\_in.vbp

030802\_goniometer\_pg.frm

Description: The goniometer system was controlled with this VB code. Digital pulses were generated and used to drive the PMT, and the scattered light was collected at different angles with the multiple channels of the AD board.

- 2). Reflectometry system control and data collection

Program Names: 030411\_reference\_add.vbp

030215\_show.frm

Description: To obtain the reflectance curve, the reflectometry system was placed on a four-axis rotation and translation stage. Four stepping motors were controlled with this VB code, and meanwhile, the data was collected and the live plot of reflectance as a function of incident angle was depicted on the computer screen.

- 3). Manual control of the stepping motors of the reflectometry system

Program Names: 010328Manual.vbp

New1115a.frm

Description: This code was developed for calibration and signal monitoring purpose and was applied to manually control the four stepping motors' movement during the calibration and watch the DC signal at any time.

#### 4). Diffusion check

Program Names: 030411\_reference\_add\_samll.vbp

030215\_show\_samll.frm

Description: This VB code was employed to check the diffusion for the reflectance measurement. At a fixed incident angle, the PD2 (see Fig. 3-10) moved on both sides with a small angular range to detect the diffuse light.

AD board built-in Modules used: DriverLINXGUIInterface (DLVBGui.bas)  
DriverLINXLibrary (DLVBLib.bas)  
DriverLNXVB(DRVLNXVB.bas)  
IEEEVB.bas  
DLCODES.bas

### D. VB Program for Goniometer System Control and Data Collection

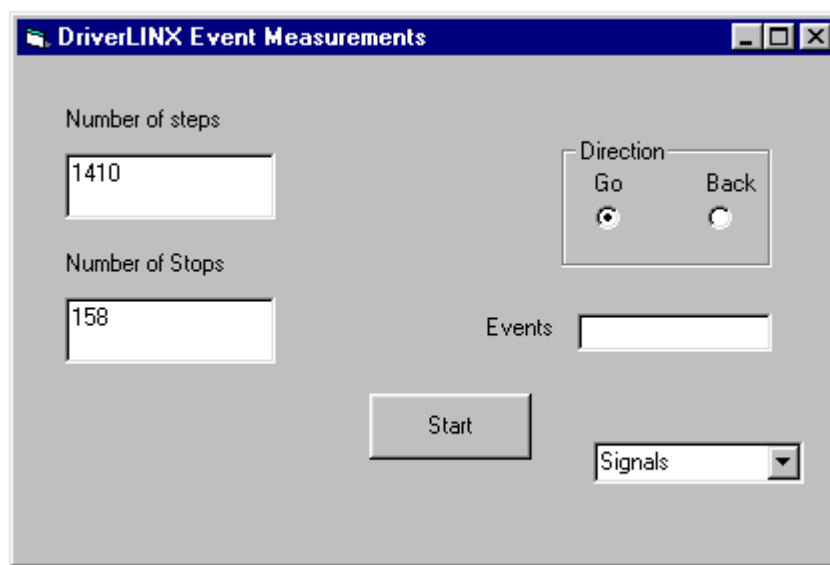


Figure D-1 Goniometer system control

```

*****
`Goniometer system control and data collection
*****

Option Explicit
` DriverLINX CTM Event Measurement Example
`public parameters
Const LogicalDevice = 0      ' Assume Device 0
Private LogicalChannel As Integer  ' Use CTM Chn 1 for measurements
Const Source = DL_SOURCE1      ' Use CTM ACLKIN1 for event input
Const ChannelGain As Single = -1#  'Gain setting for Logical Channel
Const NumberOfSamples As Integer = 500
Dim dataArray(0 To 0, 0 To NumberOfSamples - 1) As Single
Const msgRunning As String = "Running"
Const msgStopped As String = "Stopped"
Private strStatus As String
Const SamplingFrequency As Single = 1000#
Const SamplingPeriod As Single = 1 / SamplingFrequency
Const BackgroundForeground As Integer = 1
Const FullSweep As Single = NumberOfSamples * SamplingPeriod
' Number of buffers
Const NumberOfBuffers As Integer = 1

Private tics As Long
Private k444 As Long
Private FileName As String
Private outangle As Double
Private vol As Single
Private stepsequence As Integer
Private phase As Single
Private Delaytime As Single
Private fullvol As Single
Private sen As Integer
Private status As Integer
Private AD() As Single
Private AD1() As Single
Private AD_1f() As Single
Private AD1_1f() As Single
Private key_4 As Integer
Private reference() As Single

Private Sub cmdStartStop_Click()

    Dim continuous As Boolean

    ' Read and calculate parameters from user interface
    continuous = 1

    Call StartEventCount(DriverLINXSR2, LogicalDevice,
        LogicalChannel, DL_EXTERNAL, DL_DISABLED, CT_Output_Default,
        continuous)

```

```

' Setup a polling timer to periodically check for next valid
measure

' If result = DL_NoErr Then

txtResults = "measuring..."
TimerPolling.Interval = 1

End Sub

'*****
' Use this procedure for event counting
'*****

Private Sub StartEventCount(DriverLINXSR2 As DriverLINXSR, ByVal
LogicalDevice As Integer, ByVal LogicalChannel As Integer, ByVal Source
As Integer, ByVal gate As Integer, ByVal clkOut As Integer, ByVal
continuous As Boolean)

    Dim dir_val As Integer

    With DriverLINXSR3
        .Req_device = 0
        .Req_op = DL_START
        .Req_mode = DL_POLLED
        .Req_subsystem = DL_CT
        .Evt_Str_type = DL_COMMAND
        .Evt_Tim_type = DL_RATEEVENT
        .Evt_Stp_type = DL_COMMAND
        .Evt_Tim_rateClock = DL_INTERNAL1
        .Evt_Tim_rateChannel = 1
        .Evt_Tim_rateGate = DL_NOCONNECT
        .Evt_Tim_rateMode = DL_SQWAVE
        .Evt_Tim_rateOnCount = 0
        .Evt_Tim_ratePeriod = .DLSecs2Tics(DL_INTERNAL1, 1 / 1000)
        .Evt_Tim_ratePulses = 0
        .Evt_Tim_rateOutput = 0
        'tics = .Res_Tim_count
        .Refresh
    End With

    If Option1.Value Then
        dir_val = 64
    Else
        dir_val = 0
    End If

    Call subwritevalue(dir_val)

    ' Setup Service Request to perform task
    With DriverLINXSR2
        .Req_device = LogicalDevice
        .Req_subsystem = DL_CT

```

```

        .Req_mode = DL_POLLED
        .Req_op = DL_START
        .Evt_Tim_type = DL_RATEEVENT
        .Evt_Tim_rateChannel = LogicalChannel
        .Evt_Tim_rateMode = DL_COUNT
        .Evt_Tim_rateClock = Source
        .Evt_Tim_rateGate = gate
        .Evt_Tim_ratePeriod = 0
        .Evt_Tim_rateOnCount = 0

    If continuous Then
        .Evt_Tim_ratePulses = 0
    Else
        .Evt_Tim_ratePulses = 1
    End If

        .Evt_Tim_rateOutput = clkOut
        ' Other events, buffers, channels unneeded
        .Evt_Str_type = DL_NULLEVENT
        .Evt_Stp_type = DL_NULLEVENT
        .Sel_buf_N = 0
        .Sel_chan_N = 0
        .Refresh
        'StartEventCount = .Res_result
    End With

End Sub

Private Sub Command1_Click()

    Dim starttime As String
    Dim endtime As String
    Dim k5 As Long
    Dim numofstops As Integer
    k444 = 0
    k5 = CLng(Text2.Text)
    ReDim AD(k5 + 1) As Single
    ReDim AD1(k5 + 1) As Single
    ReDim AD_1f(k5 + 1) As Single
    ReDim AD1_1f(k5 + 1) As Single
    ReDim reference(k5 + 1) As Single

    MsgBox "Please give the file name to save", vbOKCancel,
        "Attention message box"
    CommonDialog1.ShowSave
    FileName = CommonDialog1.FileName
    starttime = Format(Now, "hh:mm:ss")
    key_4 = 0

    Open FileName For Output As #1
    Print #1, "Date(Mon-Day-Year)          :", Format(Now, "MM-dd-yyyy")
    Print #1, "Starttime-Endtime(H:Min:Sec):", starttime, "-",
    endtime

```

```

Print #1, " "
Print #1, "phase_2f", "Signal_1f  ", "phase_1f ", "Signal_1f ",
"Signal_DC"

Print #1, " "

`open a file for 2f signal

Open FileName For Output As #2
Print #2, "Date(Mon-Day-Year)          :", Format(Now, "MM-dd-yyyy")
Print #2, "Starttime-Endtime(H:Min:Sec):", starttime, "-",
endtime

Print #2, "phase_1f          ", "AC_2f  Signal", "DC"
Call cmdStartStop_Click

End Sub

Private Sub Form_Load()

    Dim DLDriverName As String
    Dim DLResultCode As Integer
    Dim DLDriverName1 As String
    Dim DLResultCode1 As Integer
    Dim DLMessage As String
    Dim channelNumber As Integer
    Dim Model As String
    Dim Msg As String
    ` Center form
    Me.Move (Screen.Width - Me.Width) / 2, (Screen.Height - Me.Height)
    / 2

    ` Open DriverLINX CTM driver
    DriverLINXSR2.Req_DLL_name = "kpci3100"

    ` Initialize CTM device
    DriverLINXSR2.Req_device = 0
    DriverLINXSR2.Req_mode = DL_OTHER
    DriverLINXSR2.Req_op = DL_INITIALIZE
    DriverLINXSR2.Refresh

    If DriverLINXSR2.Res_result <> DL_NoErr Then
        MsgBox ("Unable to initialize CT. Quitting.")
        End
    End If

    `StartMeasurement

    With DriverLINXSR3
        .Req_DLL_name = "kpci3100"
        .Req_device = 0
        .Req_op = DL_INITIALIZE
        .Req_mode = DL_OTHER
    End With

```

```

        .Refresh
    End With

    With DriverLINXSR4
        .Req_DLL_name = "kpci3100"
        .Req_device = 0
        .Req_op = DL_INITIALIZE
        .Req_mode = DL_OTHER
        .Refresh
    End With

    'test the board to set connection instruction
    DriverLINXSR1.Refresh
    DLDriverName = OpenDriverLINXDriver(DriverLINXSR1, "", True)

    If DLDriverName = "" Then
        ' If no driver opened, report this in a message box.
        MsgBox "DriverLINX driver not opened.", vbOKOnly, Me.Name
        ' Then close the application
        End
    End If

    DLResultCode = InitializeDriverLINXDevice(DriverLINXSR1,
        LogicalDevice)

    If DLResultCode <> DL_NoErr Then
        ' If initialization fails, report the error in a message box
        ShowDriverLINXStatus DriverLINXSR1

        ' Then close the application
        End
    End If

    'Get Model name may be needed for messages
    Model = GetModelName(DriverLINXSR1, DriverLINXLDD1)

    ' 3. See if the Logical Device supports an analog-input subsystem

    If Not HasDriverLINXSubsystem(DriverLINXSR1, DriverLINXLDD1,
        DL_AI) Then
        ' If it does not, report this in a message box.
        Msg = "This " & Model & " does not support analog input"
        MsgBox Msg, vbOKOnly, Me.Name
        ' Then close the application
        End
    End If

    SetupDriverLINXBufferedIO DriverLINXSR1, DriverLINXLDD1,
    LogicalDevice, DL_AI, LogicalChannel, ChannelGain,
    SamplingFrequency, NumberOfSamples, NumberOfBuffers,
    BackgroundForeground

    Call Initialize(21, 0)
    Call send(8, "OUTX 1", status%)

```

```

Call send(8, "OFLT 8", status%)
Call send(8, "OFSL 3", status%)
Call send(8, "SENS 26", status%)

```

```
'Add a lock-in #2
```

```

Call send(12, "OUTX 1", status%)
Call send(12, "OFLT 8", status%)
Call send(12, "OFSL 3", status%)
Call send(12, "SENS 26", status%)

```

```
End Sub
```

```
Private Sub Form_Unload(Cancel As Integer)
```

```

` Close DriverLINX driver
DriverLINXSR2.Req_DLL_name = ""

```

```
End Sub
```

```
Private Sub CalculateResults()
```

```

Dim steps As Long
Dim tics As Long
Dim r As String
Dim m As String
Dim m1, m2, m3 As String
Dim ac As Integer
Dim k As Integer
Dim t1, t2 As String
Dim newitem As String
Dim k5 As Long
Dim k6 As Long

```

```

` Read current count
DriverLINXSR2.Req_op = DL_STATUS
DriverLINXSR2.Refresh
steps = CLng(Text1.Text)
` If DriverLINXSR2.Res_Sta_typeStatus = DL_TIMERSTATUS Then
tics = DriverLINXSR2.Res_Tim_count

```

```
txtResults = Str(tics + 60) + " counts"
```

```
If tics >= steps Then
```

```

Call stop111
Call stop222

```

```

Dim k3 As Long
Dim numofstops As Long

```

```

Call DC_acquire

Call checksensitivity(vol!, phase!, fullvol!, sen%, s
tatus%, 8)
Call send(8, "SNAP?3,4", status%)
Call enter(r$, 30, ac, 8, status%)

m = Mid(r$, 10, 1)
m1 = Mid(r$, 11, 1)
m2 = Mid(r$, 12, 1)
m3 = Mid(r$, 13, 1)

If m = "," Then
    k = 9
ElseIf m1 = "," Then
    k = 10
ElseIf m2 = "," Then
    k = 11
ElseIf m3 = "," Then
    k = 12
End If

t1 = Left$(r, k)
t2 = Mid(r, k + 2, 12)

AD(k444) = Val(t2)
AD1(k444) = Val(t1)

`2nd lock-in

Call checksensitivity(vol!, phase!, fullvol!, sen%, status%,
12)
Call send(12, "SNAP?3,4", status%)
Call enter(r$, 30, ac, 12, status%)

m = Mid(r$, 10, 1)
m1 = Mid(r$, 11, 1)
m2 = Mid(r$, 12, 1)
m3 = Mid(r$, 13, 1)

If m = "," Then
    k = 9
ElseIf m1 = "," Then
    k = 10
ElseIf m2 = "," Then
    k = 11
ElseIf m3 = "," Then
    k = 12
End If

t1 = Left$(r, k)
t2 = Mid(r, k + 2, 12)

AD_1f(k444) = Val(t2)

```

```

AD1_lf(k444) = Val(t1)

newitem = Chr(32) & k444 + 1 & Chr(32) & "<----->" &
AD1(k444)
coboxresult.Text = newitem
coboxresult.AddItem newitem
numofstops = CLng(Text2.Text)

If k444 < numofstops - 1 Then
    k444 = k444 + 1
    DriverLINXSR2.Refresh
    Call cmdStartStop_Click
    tics = 0
Else
    Dim inte As Long
    For inte = 0 To numofstops - 1
        Print #1, AD(inte), AD1(inte), AD_lf(inte),
        AD1_lf(inte), reference(inte)
        ' Print #2, AD_if(inte), AD1_lf(inte),
        reference(inte)
    Next inte
    Close #1
    Close #2
    MsgBox "The process has been finished", vbOKCancel,
    "OK message box"

End If

End If

End Sub

Private Sub TimerPolling_Timer()

    CalculateResults

End Sub

Private Sub Delay()

    Dim t As Single
    Dim i As Long

    For i = 1 To 2000
        t = Sqr(2)
    Next I

End Sub

Private Sub stop111()

    With DriverLINXSR3
        .Req_op = DL_STOP
        .Refresh
    End With

```

```

        End With

End Sub

Private Sub stop222()

    With DriverLINXSR2
        .Req_op = DL_STOP
        .Refresh
    End With

End Sub

Private Sub subwritevalue(t As Integer)

    Dim writevalue As String
    Dim BackgroundForeground As Integer

    BackgroundForeground = 0
    SetupDriverLINXSingleValueIO DriverLINXSR4, DriverLINXLDD4,
    LogicalDevice, DL_DO, LogicalChannel, ChannelGain,
    BackgroundForeground
    DriverLINXSR4.Refresh
    'writevalue$ = InputBox("inpput D/O write value")
    DriverLINXSR4.Res_Sta_ioValue = t
    ' Initiate Service Request
    DriverLINXSR4.Refresh

End Sub

Sub checksensitivity(vol!, phase!, fullvol!, sen%, sta%, adress As
Integer)

    Dim s As String
    Dim length As Integer
    Dim sen1 As String
    Dim ex As Integer
    Dim sn As String
    Dim fa As Double
    Dim a As String
    Dim r As String
    Dim fa2, fa3, fa4 As Integer
    Dim fal As Double

    '-- query the sensitivity setting and calculate full scale
voltage
    6000 Call send(adress, "SNAP?3,4", status%)
    Call enter(sen1$, 30, length%, adress, status%)

    Call send(adress, "SENS?", status%)           '8=lock-in addr

```

```

s$ = Space$(10)
Call enter(s$, 30, length%, adress, status%)

ex = Val(s)
fa = Val(sen1)

If fa = 0 Then
    ex = ex - 1
    a = "SENS" + Str(ex)
    Call send(adress, a$, status%)
    DoEvents
    GoTo 6000
End If

fa2 = 0

Do
    fa1 = fa * (10 ^ fa2)
    fa2 = fa2 + 1
Loop Until fa1 >= 1

If fa2 > 0 Then
    fa2 = fa2 - 1
End If

fa3 = fa2 \ 3
fa4 = fa2 Mod 3

If fa3 < 1 Then
    If fa1 > 5 Then
        If fa4 = 0 Then
            ex = 26
        ElseIf fa4 = 1 Then
            ex = 26
        ElseIf fa4 = 2 Then
            ex = 23
        End If
    Else
        If fa4 = 0 Then
            ex = 26
        ElseIf fa4 = 1 Then
            ex = 25
        ElseIf fa4 = 2 Then
            ex = 22
        End If
    End If
ElseIf fa3 < 2 Then
    If fa1 > 5 Then
        If fa4 = 0 Then
            ex = 20
        ElseIf fa4 = 1 Then
            ex = 17
        ElseIf fa4 = 2 Then

```

```

        ex = 14
    End If
Else
    If fa4 = 0 Then
        ex = 19
    ElseIf fa4 = 1 Then
        ex = 16
    ElseIf fa4 = 2 Then
        ex = 13
    End If
End If
ElseIf fa3 < 3 Then
    If fa1 > 5 Then
        If fa4 = 0 Then
            ex = 11
        ElseIf fa4 = 1 Then
            ex = 10
        ElseIf fa4 = 2 Then
            ex = 5
        End If
    Else
        If fa4 = 0 Then
            ex = 10
        ElseIf fa4 = 1 Then
            ex = 7
        ElseIf fa4 = 2 Then
            ex = 4
        End If
    End If
ElseIf fa4 = 3 Then
    ex = 3
End If

a = "SENS" + Str(ex)
Call send(adress, a$, status%)

6300    End Sub

Private Sub menusave_Click()

    CommonDialog1.ShowSave
    FileName = CommonDialog1.FileName

End Sub

Private Sub DC_acquire()

    Dim DLMessage As String
    Dim DLResultCode As Integer
    Dim amount As Single, i As Integer

    DLResultCode = GetDriverLINXStatus(DriverLINXSR1, DLMessage)

```

```

        If DLResultCode <> DL_NoErr Then
            strStatus = DLMessage
        End If

End Sub

Private Sub DriverLINXSRL_ServiceStart(task As Integer, device As
Integer, subsystem As Integer, mode As Integer)

    ' The DriverLINXSR calls this subroutine when a task starts. This
    ' application uses this ServiceStart event to update the form,
    ' indicating that a task is currently running.
    strStatus = msgRunning

End Sub

Private Sub DriverLINXSRL_BufferFilled(task As Integer, device As
Integer, subsystem As Integer, mode As Integer, bufIndex As Integer)

    Dim samples As Long
    Dim amount As Single, i As Integer

    samples = GetDriverLINXAIBuffer(DriverLINXSRL, bufIndex,
    dataArray())

    ' Display the new data
    'ShowAnalogResults pictureCRT, NumberOfChannels, NumberOfSamples,
    _SamplingFrequency, dataArray()
    amount = 0

    For i = 0 To NumberOfSamples - 1
        amount = amount + dataArray(0, i)
    Next i

    amount = amount / NumberOfSamples
    reference(key_4) = amount
    key_4 = key_4 + 1

End Sub

Private Sub DriverLINXSRL_ServiceDone(task As Integer, device As
Integer, subsystem As Integer, mode As Integer)

    ' The DriverLINXSR calls this subroutine when a task ends. This
    ' application uses this ServiceDone event to update the form,
    ' indicating that no task is running.
    strStatus = msgStopped

End Sub

```

